UNSTEADY AERODYNAMIC CHARACTERISTICS OF SYMMETRIC AIRFOIL AT LOW REYNOLDS NUMBERS

A THESIS SUBMITTED TO
THE GRADUATE SCHOOL OF NATURAL AND APPLIED SCIENCES
OF
MIDDLE EAST TECHNICAL UNIVERSITY

BY

MERTCAN GÜNEY

IN PARTIAL FULFILLMENT OF THE REQUIREMENTS
FOR
THE DEGREE OF MASTER OF SCIENCE
IN
AEROSPACE ENGINEERING

JULY 2023

Approval of the thesis:

UNSTEADY AERODYNAMIC CHARACTERISTICS OF SYMMETRIC AIRFOIL AT LOW REYNOLDS NUMBERS

submitted by **MERTCAN GÜNEY** in partial fulfillment of the requirements for the degree of **Master of Science** i**n Aerospace Engineering, Middle East Technical University** by,

Prof. Dr. Halil Kalıpçılar
Dean, Graduate School of **Natural and Applied Sciences** _____

Prof. Dr. Serkan Özgen
Head of the Department, **Aerospace Engineering, METU** _____

Prof. Dr. Dilek Funda Kurtuluş
Supervisor, **Aerospace Engineering, METU** _____

Examining Committee Members:

Prof. Dr. Ozan Tekinalp
Aerospace Engineering, METU _____

Prof. Dr. Dilek Funda Kurtuluş
Aerospace Engineering, METU _____

Assoc. Prof. Dr. Nilay Sezer Uzol
Aerospace Engineering, METU _____

Asst. Prof. Dr. Özge Başkan Perçin
Aerospace Engineering, METU _____

Asst. Prof. Dr. Emre Kara
Aerospace Engineering, GAUN _____

Date: 18.07.2023

I hereby declare that all information in this document has been obtained and presented in accordance with academic rules and ethical conduct. I also declare that, as required by these rules and conduct, I have fully cited and referenced all material and results that are not original to this work.

Name, Last name : Mertcan Güney

Signature :

ABSTRACT

UNSTEADY AERODYNAMIC CHARACTERISTICS OF SYMMETRIC AIRFOIL AT LOW REYNOLDS NUMBERS

Güney, Mertcan
Master of Science, Aerospace Engineering
Supervisor : Prof. Dr. Dilek Funda Kurtulus

July 2023, 132 pages

Reynolds number (Re) has a dominant effect on the aerodynamic characteristics of airfoils specifically at low Reynolds number flows. In particular, low Reynolds number flows (Re<100,000) where viscous forces are dominant compared to the inertial forces, resulting in a laminar boundary layer that is more prone to separation and transition to turbulence. To understand the boundary layer physics of the low Re flows, the two-dimensional (2D) unsteady numerical simulations were conducted on a NACA 0012 airfoil with changing Reynolds numbers from 40,000 to 100,000. Moreover, the numerical simulations also involved varying angles of attack from 0° to 20° with 1° increments by using different turbulence models. The results showed that the flow separation occurred earlier at higher angles of attack and lower Reynolds numbers. The location of the separation point also affected the aerodynamic characteristics of the airfoil, with earlier separation resulting in a decrease in lift coefficient and an increase in drag coefficient.

Keywords: NACA 0012, Symmetric Airfoil, Unsteady Aerodynamics, Low Reynolds Number, Computational Fluid Dynamics

ÖZ

DÜŞÜK REYNOLDS SAYILARINDA SİMETRİK KANAT KESİTİNİN ZAMANA BAĞLI AERODİNAMİK ÖZELLİKLERİ

Güney, Mertcan
Yüksek Lisans, Havacılık ve Uzay Mühendisliği
Tez Yöneticisi: Prof. Dr. Dilek Funda Kurtuluş

Temmuz 2023, 132 sayfa

Reynolds sayısı (Re), özellikle düşük Reynolds sayılarında, kanat kesitlerinin aerodinamik özellikleri üzerinde baskın bir etkiye sahiptir. Özellikle, atalet kuvvetlerine kıyasla viskoz kuvvetlerin baskın olduğu düşük Reynolds sayılı akışlar (Re<100.000), ayrılmaya ve türbülansa geçişe daha yatkın laminer bir sınır tabakası ile sonuçlanırlar. Düşük Re sayısındaki akışlarda sınır tabakası fiziğini anlamak için, Reynolds sayısı 40.000'den 100.000'e değişen NACA 0012 kanat kesiti üzerinde iki boyutlu (2B) zamana bağlı sayısal analizler gerçekleştirilmiştir. Buna ek olarak gerçekleştirilen sayısal analizler, 1°'lik artışlarla 0°'den 20°'ye kadar değişen hücum açıları için farklı türbülans modellerini de içermektedir. Sonuçlar akış ayrımının daha düşük Reynolds sayılarında ve daha yüksek hücum açılarında daha erken gerçekleştiğini göstermektedir. Ayrılma noktasının konumu, kanat kesitinin aerodinamik özelliklerini etkilemekle birlikte kanat kesiti üzerinde görünen daha erken ayrılma durumu, kaldırma kuvveti katsayısında bir azalmaya ve sürükleme kuvveti katsayısında bir artışa neden olmaktadır.

Anahtar Kelimeler: NACA 0012, Simetrik Kanat Kesiti, Zamana Bağlı Aerodinamik, Düşük Reynolds Sayısı, Hesaplamalı Akışkanlar Dinamiği

To my family whose support always encouraged me,

To Bersu who was always there for me.

ACKNOWLEDGMENTS

I want to thank my thesis advisor, Prof. Dr. Dilek Funda Kurtulus, for guiding me in my academic career. I wouldn't be the person I am now without her direction and extensive knowledge.

Additionally, I wish to thank my family and Bersu for their unwavering support. Without their patience, it would have been impossible to do this task.

My friends Veysel and Berkan, who volunteered their skills to assist me, also deserve my gratitude and respect.

As one last word, I would like to thank UHEM (National Center for High Performance Computing) to let me use their High Performance Computing (HPC) facility and TA (Turkish Aerospace) for encouraging me to do academic research.

Computing resources used in this work were provided by the National Center for High Performance Computing of Turkey (UHEM) under grant number 4013032022.

TABLE OF CONTENTS

LIST OF TABLES

TABLES

LIST OF FIGURES

FIGURES

LIST OF SYMBOLS

SYMBOLS

c	:	Chord Length
C_d	:	Instantaneous Drag Coefficient in 2D
$\bar{C}_d$	:	Mean Drag Coefficient in 2D
C_f	:	Skin Friction Coefficient
C_l	:	Instantaneous Lift Coefficient in 2D
$\bar{C}_l$	:	Mean Lift Coefficient in 2D
C_p	:	Pressure Coefficient
D'	:	Drag Force Per Unit Span
L'	:	Lift Force Per Unit Span
k	:	Turbulence Kinetic Energy
P_∞	:	Static Pressure of the Freestream
Re	:	Reynolds Number
Re_θ	:	Critical Reynolds Number
$\widetilde{\mathrm{Re}}_{\theta t}$	:	Transition onset momentum thickness Reynolds number
t^*	:	Non–dimensional Time
T_u	:	Turbulence Intensity
U_∞	:	Freestream Velocity
u_i	:	Total Velocity

$\bar{u}_i$	:	Mean Velocity
u'_{i}	:	Fluctuating Velocity
u'	:	Fluctuating Velocity in x direction
u_t	:	Eddy Viscosity
v'	:	Fluctuating Velocity in y direction
y^+	:	Non–dimensional Distance Perpendicular to Airfoil Surface
δ_{ij}	:	Kronecker Delta
μ	:	Molecular Viscosity
μ_∞	:	Dynamic Viscosity of Air
ρ_∞	:	Freestream Density
$-\rho\overline{u'_{\mathrm{i}}u'_{\mathrm{j}}}$	:	Reynolds Stress
τ_w	:	Wall Shear Stress

CHAPTER 1

INTRODUCTION

Animals' capacity to fly has always captivated humans, and the natural world served as an inspiration for the development of aerodynamics. The study of the air and how objects move through it has been a continuous pursuit for centuries and has led to the development of a vast array of technologies, from hot air balloons to supersonic jets. Leonardo da Vinci's written rough drafts and sketches of conceptual designs and engineering approaches have had a lasting impact on the aerospace industry. His notes and drawings on flying machines, such as his famous design for a flying machine with wings made of feathers, have been an inspiration to generations of engineers and scientists.

Leonardo da Vinci was a master of visualization and understood the importance of sketches and drawings in understanding complex systems, such as fluid flows. He came to see that a skillfully drawn flow field, emphasizing the streamlines, might offer helpful insights into the flow's physical characteristics and assist draw attention to significant elements that could otherwise be missed (Bakker, 1991). Leonardo's insights into the visualization of fluid flows have indeed inspired countless questions and paved the way for further scientific inquiry. Some examples of that questions developing scientific inquiry are, whether the bounded streamline that traps fluid is a definite region of flow or not, what is the contraption of the separation on any solid body, or what happens generally to a given flow pattern as one alters a certain flow parameter (Ananda & Selig, 2018).

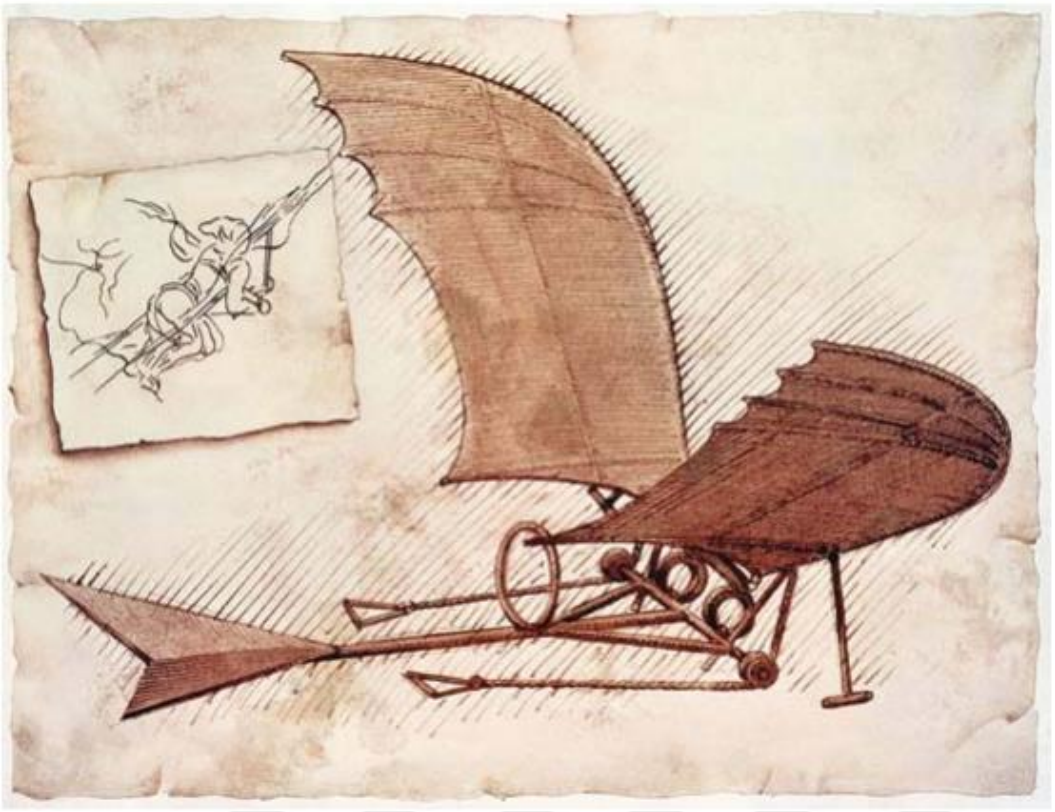

Figure 1.1. Human–powered ornithopter design of Leonardo da Vinci (Harmon & Hubbard, 2015)

After humans became fascinated with the ability of birds to fly, early aircraft designs were heavily influenced by the anatomy and flight mechanics of birds. This led to the development of aircraft with thin airfoils that mimicked the shapes of bird wings, as well as the use of wing warping as a means of control (Lilienthal, 2000). However, as knowledge of the physics of flight and aerodynamics increased, the aerospace industry gradually moved away from the early era of mimicking avian flight and began to develop more sophisticated aircraft designs based on advanced theoretical models and experimental data. With the expansion of payload and speed requirements, aircraft design and manufacturing became more complex, and new technologies and materials were developed to meet these challenges. This led to a shift away from the simple, organic shapes of early aircraft, towards more complex and aerodynamically optimized designs that were better suited to the demands of high–speed and heavy–load flight.

On the other hand, the development of electronics and avionics on a small scale has indeed made it possible to create bio–inspired flight vehicles in recent years (Raney & Waszak, 2003). So, the necessity of bringing together the two ends of flight spectrum (i.e. biological and technological) close together has arisen (McMasters, 2004). One of the main ways this has been accomplished is through the enhancement of tiny unmanned aerial vehicles (UAVs), micro air vehicles (MAVs), and flapping-wing MAVs (FWMAVs).

By definition, the most common definition of MAVs is flying machines that are not larger than 15 cm. However, advances in technology and miniaturization have made it possible to develop even smaller MAVs that can mimic the flight of common insects (Platzer et al., 2006). Still, the growth of MAVs is indeed a challenging task due to the constraints imposed by their tiny and light weight. The miniaturization of MAVs requires the integration of various components like power sources, actuators, and sensors, into a compact and lightweight design, which can be a significant engineering challenge. Moreover, controlling small–scale MAVs in flight is also challenging due to the limited control authority and their aerodynamic properties' remarkable susceptibility to minor disturbances. The small size of MAVs also implies that they are more vulnerable to disturbances from the environment, like wind gusts and turbulence, which can affect their stability and performance. So, a solid understanding of flapping-wing flight's basic aerodynamic properties at low Reynolds numbers is necessary (Bohorquez et al., 2010).

The categorization technique helps researchers to understand any physical phenomena, events, or objects for all scientific researchers. Similarly, emphasizing MAVs' and FWMAVs' areas of usage, pros/cons, and the differences between commercial air vehicles is a prior condition to understand the aerodynamics of MAVs and FWMAVs.

MAVs fall under the category of Small Unmanned Aerial Vehicles (SUAVs) and have both hovering and gliding capabilities, just like hummingbirds and other rotary–wing and fixed–wing air vehicles (Thomas & Boyer, 2011). Their agility and high maneuverability allow them to navigate through complex environments and access hard–to–reach areas. In addition to that, the optical characteristics of FWMAVs, such as their small size and the capacity to imitate the movements of insects and birds, provide them with a high degree of contextual camouflage (Alterbuchner & Hubbard, 2018). The integrated performance characteristics of FWMAVs are shown in Figure 1.2: (1) possess the best performance, (2) high maneuverability and agility, and (3) compact mission flexibility. Consequently, one can say that FWMAVs are the correct answer for design gaps in SUAVs (Grauer & Hubbard, 2011).

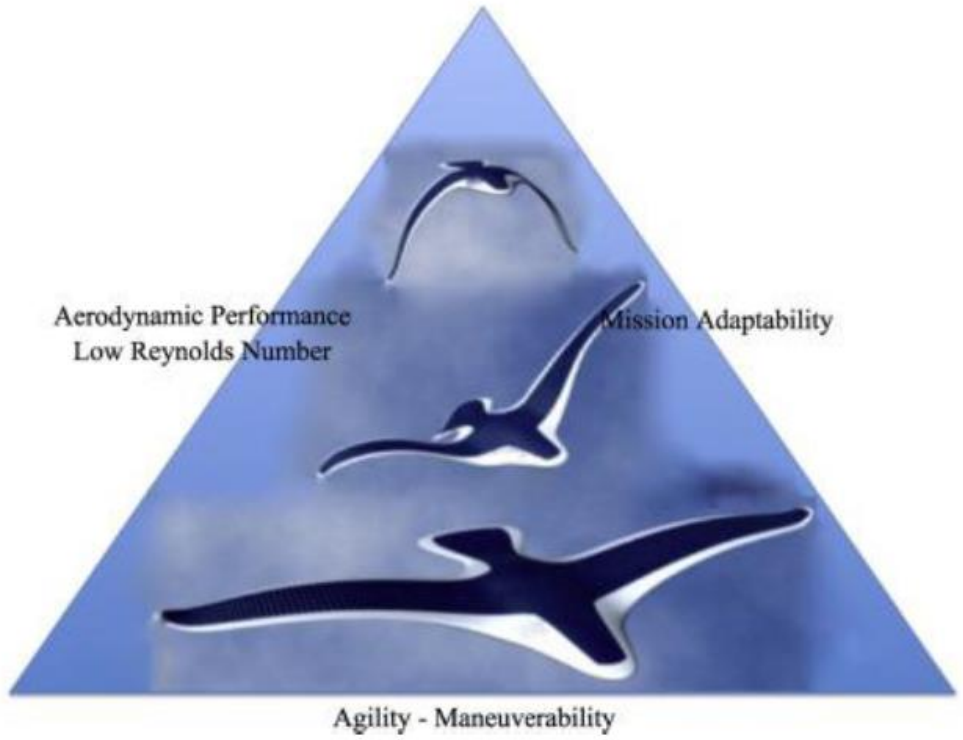

Figure 1.2. Flapping wing vehicle capabilities (NASA Langley, 2014)

UAVs, in particular, have seen widespread use in military surveillance and operations, as well as in a growing range of civilian applications such as mapping, cargo delivery, and land surveying. Moreover, FWMAVs have been developed as a safer and more agile alternative to traditional UAVs for surveillance and reconnaissance missions, especially in hazardous environments (Hu & Yang, 2008; Yang & Esakki, 2021). Due in part to their potential for military and civil applications, the development of UAVs and FWMAVs has been supported by strong financial investment in recent years.

The capability of FWMAVs to function in low Reynolds number (Re) flows like birds and insects has already been noted as one of their major characteristics. This new and important area of research allows for the development of more biologically–inspired flight technologies that can be applied to advanced Search and Rescue (SAR) missions, first–aid crews, and other applications that require highly maneuverable and efficient flight vehicles (Altenbuchner & Hubbard, 2018). That's why, the investigation of low Reynolds number flapping wings has gained significant attention among aerodynamicists as well as has been supported by strong financial investment. For example, researchers are exploring various flapping and body kinematics strategies to enhance the lift, thrust, and stability performance of flapping–wing flight (McMasters & Henderson, 1980). These studies' findings may have an impact on the development of flapping-wing aerial robots, which may find use in military reconnaissance, search-and-rescue operations, and environmental monitoring.

In addition to that, the low gravity and thin atmosphere on Mars provide unique challenges and opportunities for the design and operation of FWMAVs, making them attractive candidates for aerial exploration and survey missions. The combination of their small size, agility, and ability to hover makes FWMAVs a valuable tool for exploring difficult–to–reach areas on the Martian surface. By further advancing the capabilities of FWMAVs and incorporating new technologies, it is possible that they could play an important role in future Mars missions (Kang et al., 2018; Shrestha et al., 2016).

To overcome the challenges facing FWMAV missions on Mars, researchers must consider aerodynamics and flight mechanics that function in the low Reynolds number domain. Moreover, make sure that real products like the Marsbee (Figure 1.3) have high lift coefficients and maneuverability because they are critical parameters for successful operation in the challenging environment of Mars. To achieve this, the design should consider the flapping wing kinematics, airfoil geometry, and flow control strategies (Shyy et al., 2013). For example, for selecting optimized airfoil/wing profiles, using conventional airfoils (which are designed to best perform at $Re>10^6$) can not be proper for this kind of mission.

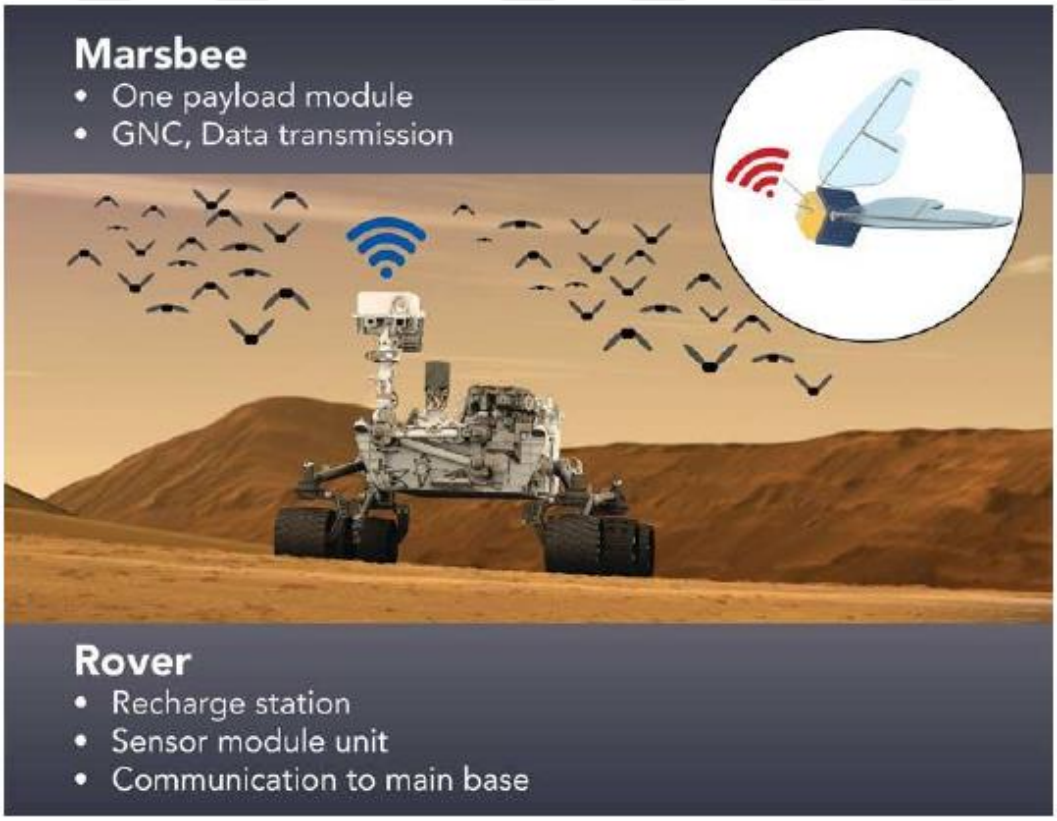

Figure 1.3. Marsbee on Mars (Shyy et al., 2013)

For flapping–wing vehicles, another example can be the Dove (Figure 1.4) (Yang et al., 2018). Wing design is a crucial part of its design, because not only lift but also the thrust is generated by pure wing. This situation is dissimilar to conventional air vehicle designs (both fixed and rotary wing configurations). Moreover, in clap and throw (Weis–Fogh, 1973), the stall is delayed due to prolonged leading–edge vortices (LEVs) (Ellington et al., 1996) capturing the wake of a wing during the return stroke (Dickinson et al., 1999; Birch, 2003) and rotational forces results from plunging and pitching motion (Sane & Dickinson, 2002; Dickinson et al., 1999) construct new challenges and involve much critical information about the birds' and insects' natural behavior. Therefore, it is valid that new aerodynamic theories and numerical simulations be developed. So, the researchers use experiments, simulations, and scaling laws to derive new design principles and strategies for flapping–wing air vehicles (Kang & Shyy, 2013).

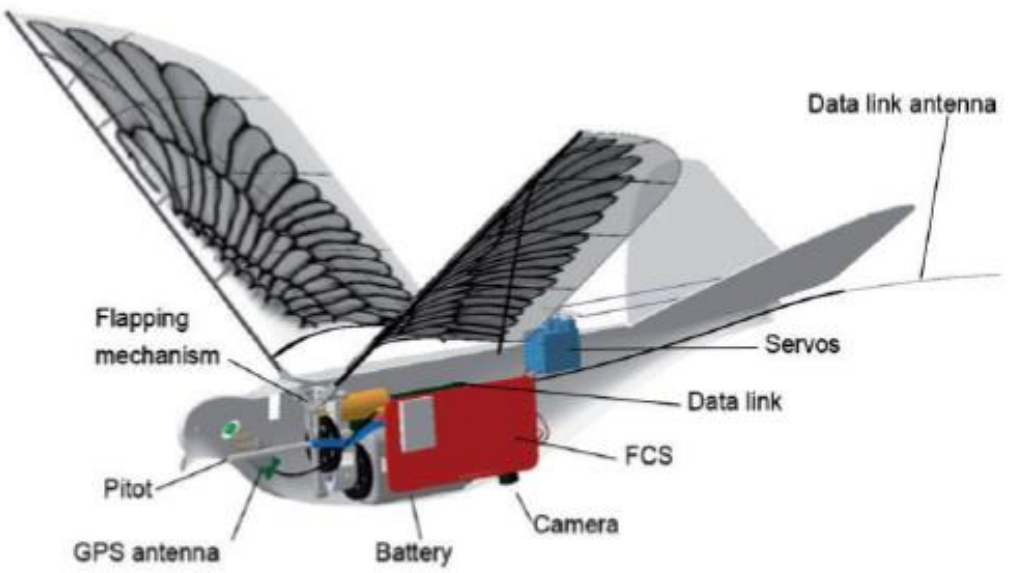

Figure 1.4. Configuration of the Dove (Yang et al., 2018)

Meanwhile, the design of FWMAVs has been enhancing every day, and their usage is also evolving. However, the creative idea of humankind about FWMAVs does not change. Nature still gives fascinating lessons to engineers to understand and develop new technologies. For example, small reference length scales of birds and insects with their low–speed result in flights at the order (O) of $Re=10^4–10^5$ and $10^3–10^4$, respectively (Shyy, 2008). Kang & Shyy (2013) stated that small insects (fruit flies, honeybees) cover the $Re=O(10^2–10^3)$, but birds like hummingbirds fly mostly at $Re=O(10^4)$. Most of them naturally fly with flapping motion, that's why, flapping–wing configurations must be designed with a more favorable wing design than fixed–wing MAVs in terms of mitigating the flights of birds and insects. Thus, engineers and scientists have been also investigating the low flight regime to understand the flight properties, however, this classification is not of one mind. Generally, below than $Re=O(10^5)$ is admitted for a low Reynolds number flow regime, but the birds and insects separate this relatively broad Re flow regime with their nature. In conclusion, $Re=O(10^4–10^5)$ flow regime also needs to be investigated wisely with both differences and the common features of $Re=O(10^3–10^4)$.

Figure 1.5. Flapping flight mode of Hummingbird (Unsplash, 2021)

By physical definition, low Reynolds number flows are nothing more than a fluid in which viscous forces predominate over inertial forces. So, boundary layer physics (e.g. flow separation phenomena, laminar/turbulent zones, reattachment points, etc.) of the solid body change compared to conventional flight regime (i.e. high Reynolds number flow regime). In detail, the flows which have low inertial forces are inclined to changing of the dynamics of the separation points, the transition to chaos, the sudden appearance of unsteadiness, and the form of stall unlike the case for high Reynolds number flow (Selig et al., 1996; Counsil & Boulama, 2013; McGranahan & Selig, 2012; Rossi et al., 2018; Yarusevych et al., 2009). So, extra alertness is necessary to understand aerodynamic characteristics and keep the benefits of FWMAVs while using them in previously mentioned missions within different low Reynolds numbers.

As an example, Figure 1.6 demonstrates the interaction between the maximum sectional lift-to-drag value and the Reynolds number change and explains the efficiency declaration. The efficiency of conventional airfoils in terms of aerodynamics quickly degrades when the Reynolds number lowers, and in that scenario, even a straightforward flat plate outperforms them. Thus, it is clear that decreasing an airfoil's Reynolds number results in a loss of efficiency with reference to the C_l/C_d value (McMasters & Henderson, 1980; Mueller, 1999).

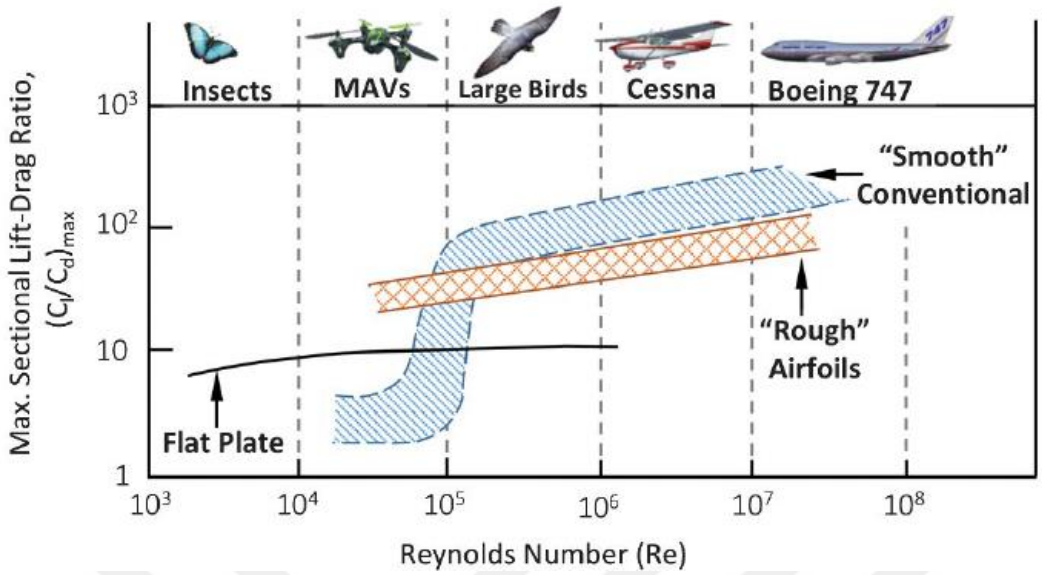

Figure 1.6. Airfoil's maximum sectional C_l/C_d vs. Re relation (McMasters & Henderson, 1980; Mueller, 1999)

Low Reynolds number flows can exhibit vortex shedding patterns and the erratic aerodynamic behavior of flapping wings under stable external conditions. Because of this, quasi-steady techniques are frequently utilized to examine the flight modes of flapping wings (Kurtulus, 2015; Kurtulus, 2016; Kurtulus, 2021; Kurtulus, 2022). The steady conditions for investigating the properties of the flapping wing contribute to not only physical interpretation but also understanding of the vortex formations and the unsteady aerodynamic behavior of the same wing (Jung & Park, 2005; Calis, 2021; Ansari et al., 2009; Jones et al., 1996; Kurtulus et al., 2004; Kurtulus et al., 2005; Lua et al., 2007; Kurtulus et al, 2006a; Kurtulus et al., 2006b; Ashrafi et al., 2012; Kurtulus et al., 2008; Lian et al., 2003). For instance, with steady external conditions, the C_l–α and $C_l - C_d$ relationships can be determined through wind tunnel experiments or computational simulations, and they offer useful details on the airfoil's non-dimensional aerodynamic coefficients. Using this knowledge, the airfoil design can be optimized for a particular application, such as a perching or flapping flight (Platzer et al., 2006).

One of the essential elements is, as was already mentioned, understanding the physics of flow separation for low Reynolds number flows. Some of the previous works resulted that, both numerically and experimentally, airfoil performance is closely associated with its boundary-layer properties. Schematic streamlines along the airfoil surface are represented in Figure 1.7. Although it is constructed for a moderate angle of attack, still gives important information about the Reynolds number effect. Laminar flow experiences a considerable negative pressure gradient towards the leading edge for Re=O(10^5-10^6) flow and a separation bubble is visible. But after the first out-of-touch receives enough momentum from the incoming external flow, it reattaches as a turbulent layer (Abbott & von Doenhoff, 1959). This layer tends to separate much less frequently and generally stays attached until the trailing edge since it has gotten its energy from the incoming flow. When an airfoil is subjected to a high incidence angle, beginning from the trailing edge, the turbulent boundary layer splits. Winslow et al. (2018) stated that it will result in decreasing lift and increasing drag (pressure drag). By migration of the separation point in the direction of the leading edge of the airfoil due to the higher incidence angles are introduced to system, the aerodynamic forces dramatically change (i.e. sharp increase for drag and abrupt reduction for lift). The term "stall" refers to this occurrence (i.e. trailing edge separation). It is generally seen in airfoils which are thick and have rounded leading edges.

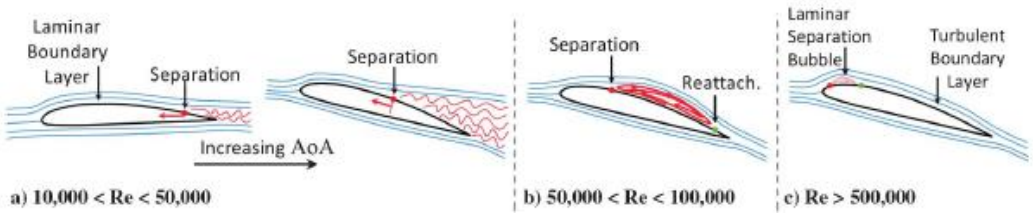

Figure 1.7. Illustration emphasizing the properties of conventional airfoils that separate at various Reynolds number regimes lower than 10^6 (Winslow et al., 2018)

For Re=O($5x10^4$–10^5) flows, the turbulent layer and separation bubble both increase in dimension. This naturally results from higher viscous forces and

contribution to parasitic drag. Still, the layer can attach the surface again, because gains enough momentum from the freestream. But, the reattachment location goes relatively backward compared to the high Reynolds number. When there is a greater incidence angle, reattachment takes place towards the trailing edge and produces relatively big separation bubbles (Mueller & DeLaurier, 2003). Near the stall, the flow starts to oscillate between complete separation and reattachment which results in large variations in pitch moment.

If $Re<5x10^4$, without subjecting the system to a high incidence angle, the separation point (laminar) extends to the trailing edge region. Since the flow has a larger resistance to flow transition, this should not be shocking (i.e. higher stability of the boundary layer) (Mueller & DeLaurier, 2003). And with the attack angle widened, the separation point goes to the leading edge of airfoil like stated in Figure 1.7, and develops a shear layer. Therefore, a smaller trailing edge separation is caused by a lower Reynolds number for the same incidence angle, which lowers the airfoil's aerodynamic efficiency (Tsuchiya et al., 2013). This is why understanding the relationship between Reynolds number and flow separation is so important in the design of aerodynamic devices.

1.1 Aim of the Research

Many publications exist in literature which explain symmetric and non–symmetric airfoils at $Re=O(10^3–10^4)$, but fewer exist on $Re=O(10^4–10^5)$ flow regimes. In addition to that, most of the ones who investigate $Re=O(10^4–10^5)$ flows to focus on the effect of a design parameter (e.g. airfoil profile, the shape of the trailing edge, roughness over airfoil surface, etc.) on airfoil performance for fixed Reynolds number instead of the effect of different Reynolds numbers. Moreover, the detailed turbulence model comparison studies exist even less while comparing the different low Reynolds number flows. So, the consistencies between not only numerical but also the literature's findings from experiments, may arise due to the lack of these

investigations. That’s why, understanding previous works and expending energy on new research can indeed be valuable.

As mentioned, there exist many experimental tests in the literature that examine the performance of airfoils under specific conditions, but these data points are often isolated and do not provide a thorough comprehension of the behavior of the airfoil concerning the Reynolds number effect. When it comes to fluid flow behavior and aerodynamic performance, the Reynolds number is a crucial factor and it is crucial to have a thorough understanding of how it affects airfoil performance. A single data point from an experimental test, even if it is well–controlled, may not accurately reflect the airfoil's behavior under a range of Reynolds numbers or other conditions. To gain a thorough comprehension of airfoil performance, it is important to consider a range of experimental data and numerical simulations that cover a large variety of Reynolds numbers and other relevant parameters. This will provide a more complete picture of the airfoil's behavior and its sensitivity to changes in Reynolds number and other conditions (Winslow et al., 2018).

Although it is possible today to carry out numerous experiments to know the aerodynamic properties of many lifting surfaces for different Reynolds number, the tests would be prohibitively take time and cost more. However, Computational Fluid Dynamics (CFD) simulations with recent technology enable the prediction of aerodynamic characteristics of the airfoils for academia and industry. It is crucial to note that, unless the most of literature works, the turbulence model selection is also another key factor in modeling features of flows at $Re \leq 10^5$. Otherwise, the experimental result differences which have been discussed previously, can not be well–defined as seen in the literature. Since the experimental findings from Ohtake et al. (2007) compared by Winslow et al. (2018), Krishnan and Ray (2022), Lan et al. (2020), Bodavula et al. (2020), Bull et al. (2021), and Zhang et al. (2022), for the validation of this work also mainly involves comparison with Ohtake et al. (2007)’s experimental results.

Finally, the major goal of this work is to provide a detailed CFD investigation of the NACA 0012 airfoil in a specific Reynolds number domain ($Re=4x10^4–10^5$), with an emphasis on how the choice of turbulence model affects the outcomes. Consequently, the results of this study will help us understand the NACA 0012 airfoil's aerodynamic behavior in great detail. So, it will be useful for the design and optimization of MAVs, and other similar small–scale aerial vehicles for the improvement of quasi–steady models used in flapping wings.

1.2 Outline

To understand the flow characteristics of the NACA 0012 airfoil in a systematic manner, this report is divided into five main chapters, including this introduction. Chapter 2 aims to offer a thorough insight to previous studies and their findings related to the topic under investigation. It involves detailed analysis and synthesis of existing literature, highlighting the key results, methodologies, and gaps in knowledge. This review serves as a foundation for the subsequent methodology chapter.

Chapter 3 outlines the numerical approach and techniques used in the study. This includes the numerical methodology employed to simulate the flow, the selection of turbulence models utilized for the investigation, and the grid refinement and time refinement studies conducted. Additionally, a thorough comparison will be made between the obtained results and the available literature data, focusing on turbulence intensity, turbulence models, and other relevant parameters.

The main focus of the Chapter 4 is to present and analyze the detailed findings of the study. This includes mean aerodynamic coefficients, pressure distributions, skin friction coefficients, streamlines, Strouhal numbers, and wake patterns. The results are reported for various Reynolds numbers between 40,000–100,000 and incidence angles between 0°–20° with a 1° increment. The aim is to understand the flow

characteristics within this range and identify any discrepancies compared to previous research.

Finally, the Chapter 5 summarizes the discussions and findings from the entire work. It provides insights into the observed discrepancies in previous results and their implications. In addition to current study's discussions and findings, possible future works are also indicated at this chapter.

CHAPTER 2

LITERATURE REVIEW

Due to their significance to a variety of applications in engineering, like airplanes and wind turbines, low Re flows have attracted growing attention from researchers in recent years. This particular work focuses on between Re=40,000-100,000, which is a relatively low range compared to high-speed flows commonly studied in the literature. Additionally, this work is distinctive in that it covers the post-stall features of the flow up to 20° incidence angle in addition to the lower incidence angle region. This is important because post-stall flows are often highly nonlinear and difficult to model accurately, making them a significant challenge for many engineering applications.

Ahuja and Rowley (2010) have shown the behavior of the flat plate between 0°–90° angles of attack at Re=100 without any turbulence models. Khalid et al. (2017) have discussed three airfoils which have 8%, 12%, and 16% thickness with symmetric NACA profile for Re=1,000. More detailed studies for numerous angles of attack at Re=1,000 are made by Kurtulus (2015, 2016) and the symmetric airfoils' wake structures have been split into various modes depending on the incidence angle of the airfoils. These works are crucial for comprehending the flow's unsteady features because wakes behind the airfoils and bluff bodies are unstable at greater incidence angles even under steady external conditions (Gopinath & Jameson, 2006).

The vortex evolution and shedding phenomena at the wake region of airfoils and bluff bodies are investigated mainly in terms of pitching and plunging airfoils because their applications are related to unsteady FWMAVs' aerodynamics (Shyy et al., 2013). Kurtulus et al. (2008) made numerical and experimental analyses like particle image velocimetry (PIV) and laser sheet visualizations for clearing the

topology of the unstable flapping motion's vortex at Re=1,000. Moreover, Kurtulus (2018, 2019) investigated computationally both the instantaneous aerodynamic forces and the vortex topologies of NACA 0012 symmetric airfoil at Re=1,000 with checking different pitching frequencies and mean angles of attack. Günaydınoğlu and Kurtulus also (2020) showed that a novel pressure reconstruction method for PIV (Particle Image Velocimetry) results around NACA 0012 flapping airfoil for the same Reynolds number. Some works of them also involve comparison between oscillatory and non–oscillatory motions.

Huang et al. (2001) also examined to an impulsively started NACA 0012 airfoil suction side in terms of vortex shedding by using PIV and particle tracking flow visualization (PTFV) methods. The work is concluded with complex multi–modes denoted as types from A to E: They are attached, trailing–edge vortex, separation vortex, leading–edge vortex, and bluff–body effect. After that, five alternative modes for a classification of the observed wake formations by using two different symmetric airfoils (NACA 0002 and NACA 0012) are offered (Kurtulus, 2016). The results of the airfoils obtained between 0°–180° incidence angles, and different modes are captured as related to the incidence angle. This classification is based on the amplitude lift coefficient spectrum, the longitudinal/lateral spacing of the vortices, and the vortex patterns. Thus, each mode has different aerodynamic characteristics.

Naeem et al. (2023) expressed the 2% thick NACA 0002 symmetric airfoil's wake characteristics between 100–3,000 Reynolds number and found two new modes, namely Mode 4i and Mode 4/3b. Mode 4i is the alternating single vortex with vortex pair shedding mode and compared its aerodynamic characteristics with Mode 4 and Mode 3. Mode 4/3b is another mode that shows the persistent time–based bifurcations phenomenon. This phenomenon involves changing the flow sporadically to Mode 3b from the dominant Mode 4.

For relatively higher Reynolds numbers, the studies by Ohmi et al. (1990, 1991) are conducted both numerically and experimentally to examine the vortex formation on NACA 0012 airfoil and an ellipse. He investigated between Re= 1,500-10,000. Similarly, the literature also presents additional vortex features and a comparison of aerodynamic performance at various Reynolds numbers. Here's one, Alam et al. (2010) studied the lift variation of the two-dimensional NACA 0012 profile between 0° and 90° incidence angles and Re=$5.3x10^3$–$5x10^4$, combined with Strouhal number and a thorough flow structure close to the wake zone. In the results, it revealed that the stall occurs in lower angle of attack for Re=$1.05x10^4$, that indicating a difference in aerodynamic characteristics of airfoils between the ultra–low and relatively higher Reynolds numbers. In addition to that, he linked the wake patterns with the lift variations which is also related to incidence angle.

Anyoji et al. (2014) performed that two-dimensional NACA 0012 and NACA 0002 profile comparison on Re=$23x10^3$. Counsil and Boulama (2013) also showed another performance comparison of airfoils from Re=$4.8x10^4$ to $2.5x10^5$ below than 8° angle of attack. Moreover, Selig et al. (1996) conducted experiments on 34 different airfoils within Re=60,000–300,000. However, all these works have not focused on the high angles of attack characteristics, and produced limited discussions.

For lower Reynolds number flows, there exist other old experiments on various airfoils (Selig et al., 1989; Mueller & Batill, 1982). Both experiments stated that $\overline{C}_{l_{max}}$ increases for relatively higher Reynolds number. Moreover, the $C_{d_{min}}$ importantly decreases when the flow experiences Re≥10^5. Selig et al. (1989) also demonstrated the polar drag of approximately 60 sailplane-type airfoils, then concluded that the results insensitive to change of Re when the flow is Re≥10^5. However, for Re≤10^5, the drag polar curve has nonlinear relation for different Reynolds numbers. Thus, both investigations demonstrated that the shape and range of Reynolds number had a significant impact on airfoil performance.

Moreover, Schmitz (1967) made other experiments on three geometries, which are a thin flat plate, a cambered plate, and an N60 airfoil (12.4% t/c, %4 camber) in between Re=$2x10^4$–$2x10^5$. He concluded that the flow is more likely to separate and that thin plates perform better below Re=10^5. After the 1980s, the works in literature that are mentioned until now, and many others, conducted numerous experiments and simulations. However, the data sets which are mostly below than Re=10^5 involve uncertainties and discrepancies (Winslow et al., 2018). For instance, E387 airfoil at Re=$6x10^4$ results vary by 28–68% between different experimental measurements (Lyon, 1997). However, at Re=$2x10^5$, the drag coefficient difference converges to a 13% error at the work of Lyon (1997), which is an acceptable margin (Winslow et al., 2018). This contradictoriness results from measurement methods such as load measurement or wake–momentum deficit (Selig et al., 1996) which have inadequate sensitivity (Laitone, 1997), and turbulence levels of the wind tunnel (McAurthur, 2008).

Although the experimental methodology and measurement tools have been developed last 20 years, the uncertainties for Re≤10^5 continue due to its natural physics which has been introduced previously. For instance, Zakaria et al. (2018) show that the experimental results have nearly 40% errors concerning C_l around 15° incidence angle around Re=80,000 concerning the outcomes of Ohtake (Ohtake et al., 2007). Also, Zhang et al. (2022) compared their experimental results with Tan et al. (2021), Bull et al. (2021), and Ohtake et al. (2007) at Re=100,000. The differences between the experiments are clearly illustrated in terms of $\bar{C}_l$. For instance, the stall angle is found as 12° by Tan et al. (2021) with $\overline{C}_{l_{max}}$ value is almost 0.9872. However, Bull et al. (2021) found a stall angle of around 10° and the $\bar{C}_l$ difference is diverging almost 35% as the angle of attack is above 13°. Moreover, the work of Zhang et al. (2022) has totally a lack of information about the $\overline{C}_d$.

CHAPTER 3

METHODOLOGY

The performance and design optimization of airplanes and spacecraft are heavily reliant on aerodynamics. The mathematical models used in aerodynamics are used to determine the behavior of air as it flows over the surface of an aircraft or spacecraft, taking into account various factors like pressure, velocity, turbulence, and temperature.

Both the boundary layer equations and the Navier-Stokes equations are two of the most often used mathematical models in aerodynamics. The motion of the fluid is explained by the Navier-Stokes equations by using the main physical parameters such as velocity, pressure, and temperature. Meanwhile, the thin layer of fluid extremely near an object's surface that is affected by the surface's presence is known as the boundary layer in physical terms, and its modeling properly is highly important to capture all flow properties.

3.1 Numerical Methodology

When combined with knowledge about the features of flow turbulence, the Reynolds-averaged Navier Stokes (RANS) equations are formulated for time-averaged fluid flow that may be used with approximate time-averaged Navier-Stokes equation solutions (Medina et al., 2014).

The equation below states that the mean velocity $\bar{u}_i$ and fluctuation velocity u'_i make up the total velocity u_i (Aftab et al., 2016).

$$u_i = \bar{u}_i + u'_i \tag{1}$$

The conservation of mass and momentum are represented by the equations below, respectively:

$$\frac{\partial \rho}{\partial t} + \frac{\partial}{\partial x_i}(\rho u_i) = 0 \tag{2}$$

$$\frac{\partial}{\partial t}(\rho u_i) + \frac{\partial}{\partial x_j}(\rho u_i u_j) = -\frac{\partial \rho}{\partial x_i} + \frac{\partial}{\partial x_j}\left[\mu\left(\frac{\partial u_i}{\partial x_j} + \frac{\partial u_j}{\partial x_i} - \frac{2}{3}\delta_{ij}\frac{\partial u_k}{\partial x_k}\right)\right] + \frac{\partial}{\partial x_j}(-\rho\overline{u'_i u'_j}) \tag{3}$$

These two equations are known as RANS equations (Batchelor, 2002; Saniei & Mani, 2014; Versteeg & Malalasekera, 2007) in Cartesian tensor form. Reynolds stress term is on the second equation's right side (R_{ij} or $-\rho\overline{u'_i u'_j}$) and needs to be modeled. The Reynolds stress and mean velocity are related according to the Boussinesq theory (Saniei, 2009; Schmitt, 2007) as follows:

$$R_{ij} = -\rho\overline{u'_i u'_j} = \mu_t\left(\frac{\partial u_i}{\partial x_j} + \frac{\partial u_j}{\partial x_i}\right) - \frac{2}{3}\left(\rho k + u_t\frac{\partial u_k}{\partial x_k}\right)\delta_{ij} \tag{4}$$

Where μ is the molecular viscosity, k represents the kinetic energy of the turbulence (the total of the diagonal Reynolds stress tensor components) and u_t indicates the eddy viscosity, and δ_{ij} is the Kronecker delta (Mousavi et al., 2017). There have been developed new and more reliable turbulence models throughout the history of the aerospace industry in an effort to more accurately depict the properties of fluids.

Each of these turbulence models has its own advantages and disadvantages to be used for the particular flow conditions and the desired level of accuracy. For example, the computationally efficient Spalart-Allmaras (SA) turbulence model models turbulence using just one equation and widely used for industrial applications. In contrast, the SST k–ω and k–kl–ω are two and three equations turbulence models that provide improved accuracy for flows with strong turbulence anisotropy. On the other hand, the Transition (γ–Re_Θ) SST turbulence model is a combined turbulence model that uses the advantages of not only RANS methodology but also the large–eddy simulation (LES) methods, and it is usually used to study complex flows with many different turbulence scales.

In conclusion, turbulence models are essential for forecasting the behavior of low Reynolds number flows. A particular condition determines the choosing of a turbulence model and the level of precision needed. For selecting the proper turbulence model: Spalart–Allmaras, SST k–ω, k–kl–ω and Transition (γ–Re_Θ) SST turbulence models are investigated in the chapters that follow.

3.1.1 Spalart–Allmaras turbulence model

Although the single equation that forms the basis of the Spalart-Allmaras (SA) turbulence model, it is reliable and useful in simulating the external flow over an airfoil with unfavorable boundary layer pressure gradients (Spalart & Allmaras, 1992; Versteeg & Malalasekera, 2007).

SA turbulence model can be effective for cases which have a low Reynolds number, but the grid resolution should be super fine with non–dimensional distance perpendicular to the airfoil surface, $y^+ \leq 1$ (Fluent, 2015; 2016).

3.1.2 SST k–ω turbulence model

SST *k–ω* turbulence model bases on a mixture of the Wilcox *k–ω* and the standard *k–ϵ* model (Menter, 1994). By inserting $\epsilon = k\omega$, the conventional *k–ϵ* becomes *k–ω* (Versteeg & Malalasekera, 2007). With the freestream independence of the *k–ϵ* model in the distant field, it offers robust solutions in the wall region (Ren & Ou, 2009). This two equations based turbulence model provides more accurate results compared to the regular *k–ω* model (Aftab et al., 2016).

3.1.3 K–kl–ω turbulence Model

A turbulence model called *k–kl–ω* is created for transitional flows (Walters & Cokljat, 2008). The prediction of the transition onset characteristics are advanced. This turbulence model is based on three equations for modelling turbulent viscosity.

3.1.4 Transition–SST turbulence model

Transition (γ–Re_Θ) SST turbulence model is also mainly designed for transitional flows. Basically, this model has an union of SST k–ω and intermittency γ (the time fraction at a specific location where the flow is turbulent (Fowler & Howell, 2003)), and transition onset Reynolds number equations. The onset of intermittency happens at the critical Reynolds number, i.e. Re_Θ, (Langtry & Menter, 2009).

So, this model involves four equations and two of them are analogous to SST k–ω. The last two equations are related to intermittency and transition onset momentum thickness Reynolds number, $\widetilde{Re}_{\theta t}$, (Menter et al., 2006).

For determining the transition behavior, the mesh shall be modeled as $y^+ \leq 1$ (Hau & von Reynouard, 2006; Mendez et al., 2017). Otherwise, the viscous sub–layer may not be modeled properly.

3.2 Simulation Setup and Grid Geometry

In this work, the simulations are carried out via a commercial CFD tool, ANSYS Fluent (v.18.1), which uses the finite-volume approach at the background. Also, the semi-implicit technique (SIMPLE) approach is used for pressure-linked equations where SIMPLE stands for Semi–Implicit Method for Pressure Linked Equations. This method is appropriate for unsteady aerodynamic analysis according to Fertizer et al. (2020). In essence, the SIMPLE approach resolves the momentum equation to obtain a steady-state solution for the velocity field. This algorithm basically updates the velocity field at each iteration, and it converges to a final solution up to the change in the velocity field between sequential solutions is small enough. To discover a time-dependent solution for the fluid flow, it is utilized to iteratively update not only the pressure fields but also the velocity fields at each time step.

Explicit methods are methods in which the solution is fed by known variables from the previous time step. The solution is advanced by using only the known variables and no unknown variables are kept in the calculation. Implicit methods, on the other hand, keep some variables unknown while the solution marches on. However, implicit methods are typically more computationally expensive than explicit methods. As befits the name, the depicted procedure in the above paragraph represents the semi–implicit methodology. While the velocity component is explicitly addressed, the momentum equation is implicitly solved as a pressure correction equation. This semi–implicit method provides a balance between computational efficiency and solution accuracy, and it is used frequently in computational fluid dynamics simulations. In addition to that, throughout the simulations, the spatial and time solutions are accurate as second order in terms of both space and time which means that the solution is accurate and well–resolved, even in complex fluid flow problems with adverse pressure gradients and boundary layer separation.

As a turbulence model Transition (γ–Re_{Θ}) SST is used (Aftab et al., 2016). The simulations are performed with this model and the results are compared from 0° to 20° angles of attack with 1° increment. For unsteady aerodynamic coefficients, the time–averaged values are kept between [8s 10s]. The inlet pressure is taken as sea level (101,325 Pa) and the temperature condition is taken as 288.15 K (15°C). Also, the convergence threshold is set at in order to ensure accuracy as $1x10^{-6}$ (Agrawal et al., 2020). Lastly, the characteristic length is taken as $0.07c$ (Versteeg & Malalasekera, 2007).

The unsteady aerodynamic analysis results do not depend on only the solution setup, but also the chosen grid topology and geometrical properties. So, the grid topology and geometrical properties must be optimized and assimilated. The airfoil is chosen as a symmetric NACA 4–digit, NACA 0012, airfoil for this particular work.

NACA–4 digit thickness distribution of airfoils can be found as follows (Abbott & von Doenhoff, 1959):

$$y_t = \pm \frac{t/c}{0.2}.(0.2969.\sqrt{x} - 0.1260.x - 0.3516.x^2 + 0.2843.x^3 - 0.1015.x^4) \quad (5)$$

where x ϵ [0 1]

For NACA–4 digit airfoils, the last two digits directly give this ratio. Specifically, NACA 0012 represents 12% maximum thickness relative to chord length. In addition to that, the first digit indicates the maximum camber as %chord and the second one indicates the chord's tenths of the greatest camber from the leading edge (Özdemir & Barlas, 2021).

Moreover, the airfoil grid topology for analysis is constructed in commercial software, Pointwise. The airfoil's chord length is 0.1m, and to minimize numerical inaccuracies, this size is multiplied by 100 in the Pointwise tool.

The formulization of non–dimensional aerodynamic coefficients and general information of the solution setup as follows:

$$Re = \frac{\rho_\infty U_\infty c}{\mu_\infty} \quad (6)$$

$$C_l = \frac{L'}{\frac{1}{2}\rho_\infty U_\infty^2 c} \quad (7)$$

$$C_d = \frac{D'}{\frac{1}{2}\rho_\infty U_\infty^2 c} \quad (8)$$

$$C_p = \frac{P - P_\infty}{\frac{1}{2}\rho_\infty U_\infty^2} \quad (9)$$

The numerical simulation's parameters are enumerated in Table 3.1. The airfoil analysis is conducted between Re=[40,000–100,000] with 10,000 increments. Moreover, the angle of attack value is changed between α=[0°–20°] with a 1° increment. The airfoil is rotated in a clockwise direction around a fixed point, 0.25*c*, to increase the angle of attack. For each configuration inner grid region is reconstituted so that the wake region keeps constant.

Table 3.1. Parameters of the Numerical Simulation

Turbulence model	Transition (γ–Re_Θ) SST
Reynolds number range	[40,000–100,000] with 10,000 increment
U_∞,Velocity range (m/s)	[5.86–14.65]
Angles of attack ($^\circ$)	[0°–20°] with 1 degree increment
Turbulence intensity	3%
Characteristic length	0.07c
Temperature (K)	288.15
Pressure (Pa)	101,325
Density (kg/m^3)	1.225
Dynamic viscosity (Pa.s)	1.789×10^{-5}

The geometrical representation that limits the numerical simulation is known as the computational domain (Narsipur et al., 2012). In this work, except for the structured boundary layer grid topology, the computational domain has two main sub–domains: inner and outer. The grid for the inner domain is made up of a 1.5c wide rectangular area at the downstream and a 3c diameter half-circle zone with its center at the c/4 position of the airfoil upstream.

By and large, grids can be classed as structured, unstructured, or hybrid depending on how the grids are connected (Lu et al., 2021), and the choice of the grid type has a considerable effect on simulation results (Liseikin, 2009). According to Aftosmis et al. (1995), unstructured topologies are 50 times more expensive than structured quadrilateral grids with nearly the same precision. On the other hand, unstructured grids have advantages over structured ones in terms of being more suitable for complex geometries and having less solution time.

That's why, hybrid grids have been seen as a compromise between structured and unstructured grids for taking advantage of the strengths of both types of grids. Meanwhile the unstructured portion of the domain allows for greater flexibility in

grid refinement and faster generation times, the boundary layer and wake regions are captured by structured grids that result in higher fidelity as the results of flow physics.

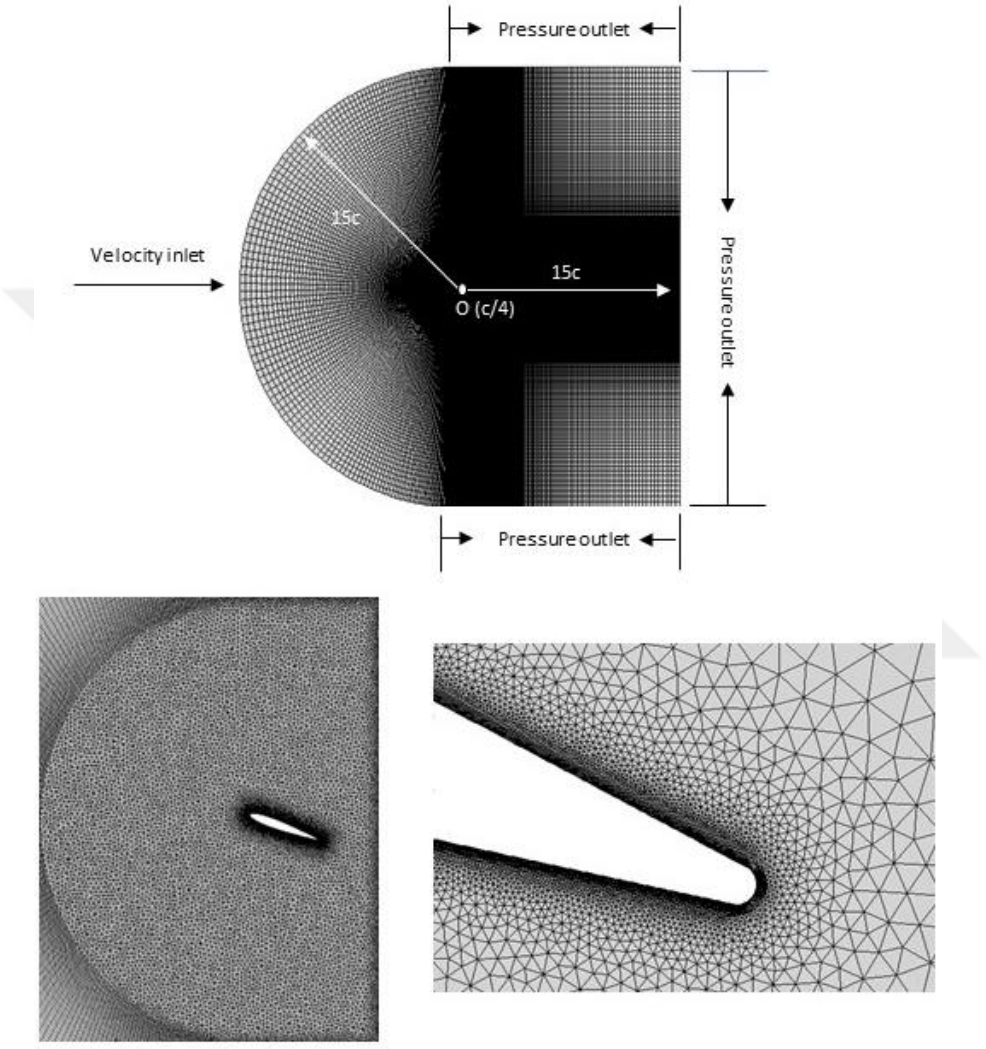

Figure 3.1. Grid topology

Moreover, the outer zone of this work is constructed as a rectangular section downstream of the airfoil with a length of 15*c* and a 15-*c*-diameter C-type structured grid.

As boundary conditions, the front semi–circle side of the outer domain held velocity inlet meanwhile the above, below and right sides of the outer domain held pressure outlet as indicated in Figure 3.1. Also, the airfoil profile must meet the no-slip criteria since it serves as a "wall" boundary condition. The no-slip criterion stipulates that the fluid velocity at all fluid-solid barriers must be the same as the solid boundary (Day, 1990). For viscous flows, it means that at a solid boundary (in this case, it is an airfoil surface), the fluid will have no velocity concerning the boundary. Since the solution is prescribed at a given particular location, this is an example of a Dirichlet boundary condition.

3.3 Grid and Time Refinement Studies

A numerical solution becomes more precise with grid refinement, so models the physical problem in an optimized way. Using the additional grids result in increase in computing time and memory (Khchine & Sriti, 2017). That's why, the trade–off work should be made about the grid structure and the aim should be getting sufficient fine results so that further refinement does not change the result excessively.

For this work, the grid and time refinement studies are conducted at 10° and 20° incidence angles at the greatest Reynolds number examined in this research (Re=100,000). The angles of attack are chosen to be 10° at the linear region's end of the C_l vs α curve and 20° at the maximum degree investigated by Winslow et al. (2018). Four different mesh domains are created in order to obtain accurate results with less computational time. They are called: Coarse, Medium 1, Medium 2, and Fine grids. When the node count is established, it is observed whether the results dramatically alter if the number of nodes changes (Eleni et al., 2012). Moreover, the grid refinement is conducted with a constant growth rate of 1.1 (Yousefi et al., 2014), and the number of boundary layer grides is varied by 20, 25, 25, and 30, respectively for each grid. Lastly, the aerodynamic coefficients are averaged between [8s 10s] which is equivalent to a non-dimensional time, $t^*=tU_\infty/c$=[1172 1465]. With the getting of aerodynamic results after t^*=1172, the initial impulsive start effects have not been taken into account and only steady/quasi–periodic solutions are concerned.

$$t^* = \frac{tU_\infty}{c} \tag{10}$$

The mean aerodynamic coefficients refer to the time–averaged type of coefficients and are denoted by a bar sign ($\bar{}$). For instance, the instantaneous lift coefficient is shown by C_l , but the time–averaged mean lift coefficient is shown by $\bar{C_l}$.

Another important parameter for grid structure is that y^+. The y^+ parameter describes how much of a cell's impacts are turbulent compared to laminar, which indicates a non-dimensional distance perpendicular to the airfoil surface (Salim & Cheah, 2009). Viscous damping effects lessen the tangential velocity oscillations if one tries to bring the solution extremely close to the wall. The significant disparities in mean velocity cause the turbulence to quickly intensify as it moves away from the near-wall and towards the outer domain. While for wall function problems y^+~30 is suitable, the most desirable value for near–wall modeling is y^+ ≤1 (Gerasimov, 2006).

This y^+ can be achieved by using the following formulations:

$$y^+ = \frac{u_\tau y_p \rho_\infty}{\mu_\infty} \tag{11}$$

$$u_\tau = \sqrt{\frac{\tau_w}{\rho_\infty}} \tag{12}$$

$$\tau_w = \frac{1}{2}\rho_\infty C_f U_\infty^2 \tag{13}$$

$$C_f = [2log(\mathrm{Re}) - 0.65]^{-2.3} \tag{14}$$

where friction veloicty is denoted by u_τ, and wall shear stress is denoted by τ_w. Although there exists a lot of formulations for the skin friction coefficient, C_f, the above one is used from Schlichting et al. (1979).

In conclusion, the NACA0012 airfoil analysis is conducted with 0.001%*c* first layer height (Winslow et al., 2018). In-depth discussion of the grid refinement study and associated aerodynamic findings will be provided in the following chapters.

3.3.1 Grid refinement results

Despite the fact that there are some articles on the NACA 0012 airfoil for different Reynolds numbers, this effort seeks to refine the initial grid and time on its own before comparing the outcomes to numerical and experimental values in the literature. For this purpose, the grid refinement is conducted at specific incidence angles, namely 10° and 20° for Re=100,000.

Table 3.2. Grid Configurations

	Coarse	***Medium1***	***Medium2***	***Fine grid***
Nodes around the airfoil	3,000	4,000	4,000	5,000
Total number of elements	206,012	301,102	302,114	401,053
First cell height above the airfoil	0.006%c	0.004%c	0.001%c	0.001%c
Number of layers inside the boundary layer	20	25	25	30
The growth rate	1.1	1.1	1.1	1.1

The grid refinement is conducted with a constant growth rate of 1.1 (Yousefi et al., 2014). With keeping the growth rate is same; different grid numbers/node numbers around the airfoil surface, first cell sizes, and boundary layer thickness are compared. Thus, the results of mean aerodynamic coefficients are compared as in the following tables.

Table 3.3. Grid Refinement Results at $\alpha=10^{\circ}$ for Re=100,000

	Angle of Attack (α) = 10°			**Error (%) of α = 10°**		
	$\overline{C}_l$	$\overline{C}_d$	$\overline{C}_l/\overline{C}_d$	$\overline{C}_l$	$\overline{C}_d$	$\overline{C}_l/\overline{C}_d$
Coarse	0.8381	0.041995	19.9571	1.0124	2.6947	3.8124
Medium 1	0.8364	0.042604	19.6324	0.8075	1.2836	2.1234
Medium 2	0.8300	0.043094	19.2611	0.0362	0.1483	0.1919
Fine	0.8297	0.043158	19.2242	–	–	–

The reference results are taken from the fine grid, then relatively percentage errors are calculated for other grides. URANS (Unsteady Reynolds–averaged Navier Stokes) solutions are tabulated by using time–step, Δt=0.003s. This time–step value results from another detailed time–step refinement study which will be discussed in the following chapter. In short, as shown in Table 3.3., the error numbers frequently decrease at 10° angle of attack for denser grid types. This outcome was predicted because with a smaller first layer thickness and a higher total number of elements, the boundary layer flow characteristic converges to a hypothetically real physical solution. Numerically, at 10° angle of attack, the Coarse grid has 2.6947% error in $\bar{C}_d$ and Medium 1 has 0.8075% and 1.2836% errors for $\bar{C}_l$ and $\bar{C}_d$ respectively. The error in $\bar{C}_d$ decreases higher than 50% which is important to capture flow fields properly. Moreover, the error values are also dramatically decreased to 0.0362% and 0.1483% by using Medium 2. That's why, it is proper to use Medium 2 instead of Medium 1, and it is easily shown that the Fine grid is unnecessary. Because similar results can be achieved with lower computational time cost with Medium 2.

Figure 3.2 illustrates how different grid topologies converge to aerodynamic coefficients as $\bar{C}_l$ and $\bar{C}_d$ at 10° incidence angle. The convergence is successfully achieved for each grid topology, and the differences between them are also revealed by looking first steps of solutions. Coarse and Medium 1 grides (blue and green lines) show a small bias according to Medium 2 and Fine grids. So, the mean aerodynamic coefficient errors and time history of each configuration are consistent. Thus, the selected grid topology is Medium 2 by looking at 10° incidence angle for Re=100,000.

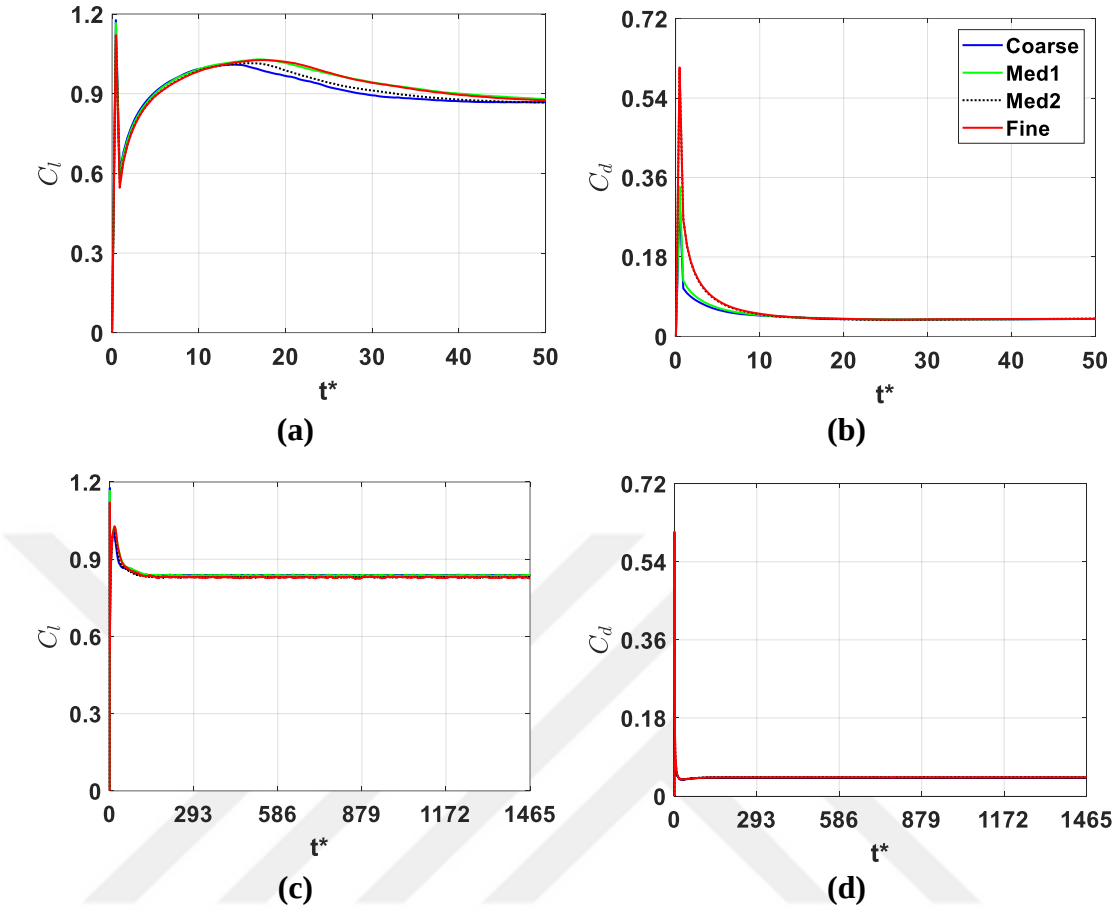

Figure 3.2. Instantaneous aerodynamic coefficients vs. t* (grid refinement study) at $\alpha=10^{\circ}$ for Re=100,000: a) lift coefficient in the time inverval of t^*=[0s 50s], b) drag coefficient in the time inverval of t^*=[0s 50s], c) lift coefficient in the time inverval of t^*=[0s 1465s], d) drag coefficient in the time inverval of t^*=[0s 1465s]

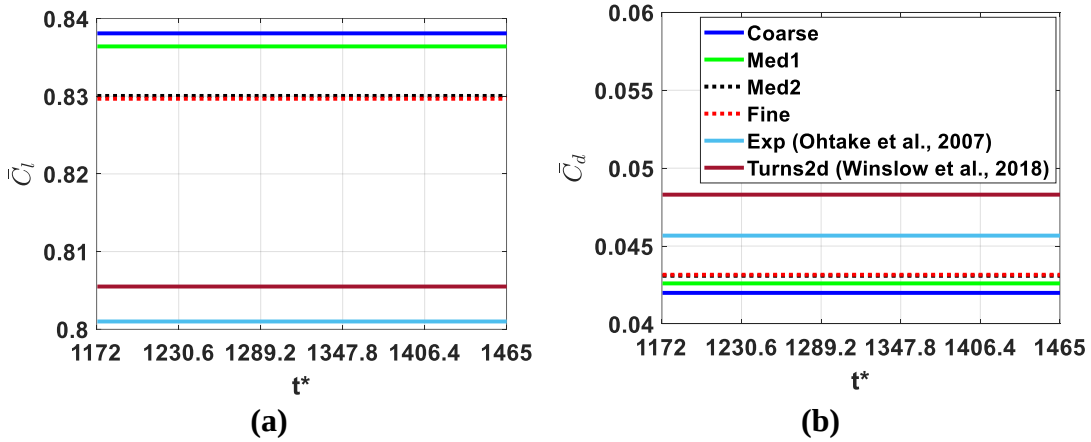

Figure 3.3. Mean aerodynamic coefficients vs. t* (grid refinement study) at α=10° for Re=100,000: a) lift coefficient, b) drag coefficient

Table 3.4. Grid Refinement Results at α=20° for Re=100,000

	Angle of Attack (α) = 20°			**Error (%) of α = 20°**		
	$\bar{C}_l$	$\bar{C}_d$	$\bar{C}_l/\bar{C}_d$	$\bar{C}_l$	$\bar{C}_d$	$\bar{C}_l/\bar{C}_d$
Coarse	0.7451	0.31580	2.3593	1.3328	1.5859	0.2477
Medium 1	0.7434	0.31591	2.3532	1.1016	1.6213	0.5099
Medium 2	0.7432	0.31375	2.3688	1.0744	0.9264	0.1522
Fine	0.7353	0.31087	2.3652	–	–	–

Similar trends with different magnitudes on mean aerodynamic coefficient errors are also valid for 20° angle of attack. The error magnitudes are closer when comparing incidence angles of 20° versus 10°, though. The inaccuracy of $\bar{C}_d$ for Medium 2 is still approximately half that of Medium 1, which is primarily due to the variation in first cell height. Although 0.004%*c* (Medium 1 first layer height) satisfies the $y^+ \leq 1$, the first layer value from Winslow et al. (2018) gives more accurate results.

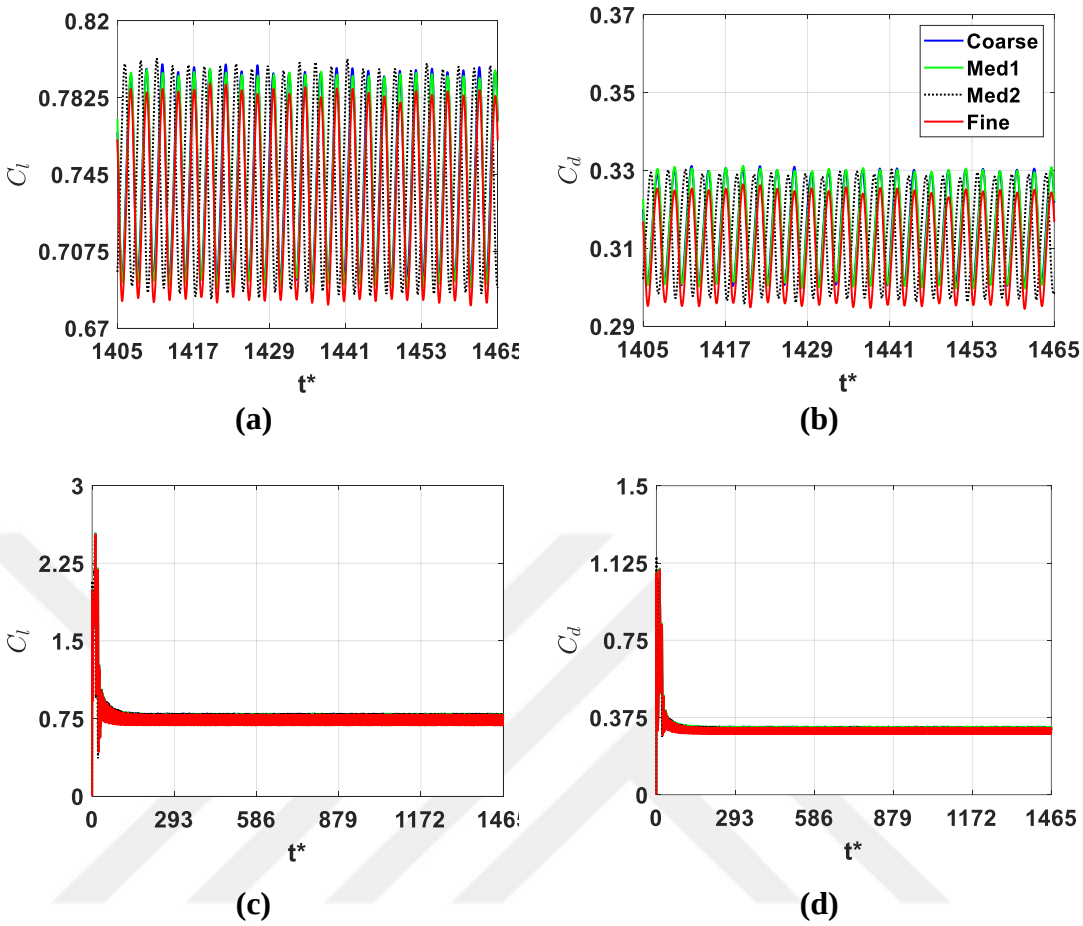

Figure 3.4. Instantaneous aerodynamic coefficients vs. t* (grid refinement study) at α=20° for Re=100,000: a) lift coefficient in the time inverval of t*=[1405s 1465s], b) drag coefficient in the time inverval of t*=[1405s 1465s], c) lift coefficient in the time inverval of t*=[0s 1465s], d) drag coefficient in the time inverval of t*=[0s 1465s]

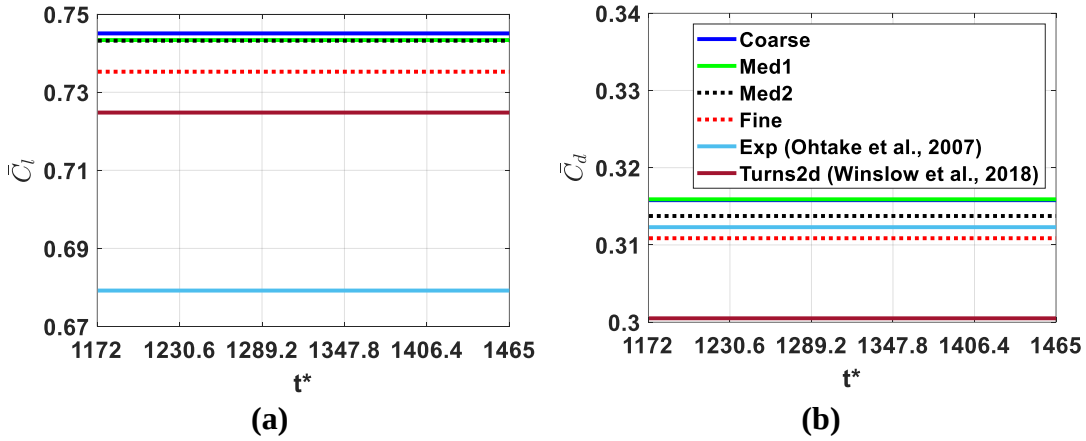

Figure 3.5. Mean aerodynamic coefficients vs. t* (grid refinement study) at α=20° for Re=100,000: a) lift coefficient, b) drag coefficient

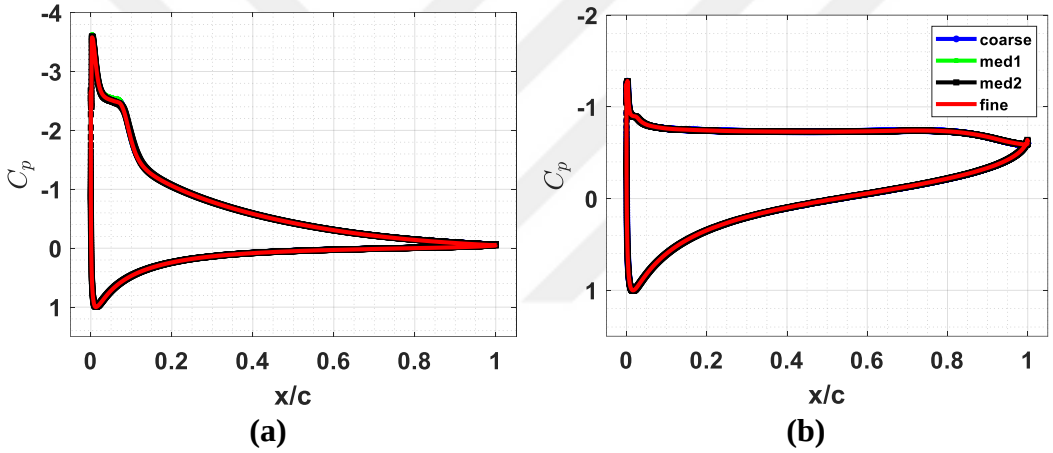

Figure 3.6. Mean pressure distributions around NACA 0012 with different grids for Re=100,000: a) α=10°, b) α=20°

The general differences between Medium 2 and Fine Grid are around 1%, so it is again proper to use Medium 2 instead of Fine grid by investigating 20° angle of attack in terms of computational time–saving. To sum up, Medium 1 and Medium 2 have almost the same grid numbers with different configurations. It means that computational time for both grid topologies will be similar, but the both errors of $\bar{C}_l$ and $\bar{C}_d$ for 10° and $\bar{C}_d$ value for 20° are dramatically decreased by using Medium 2 configuration.

Additionally, adding more elements (Fine grid) does not significantly alter the aerodynamic coefficients. That's why, Medium 2 is the most suitable one among the existing grid configurations.

3.3.2 Time refinement results

To determine the optimized time step, five different time steps are used with Medium 2 grid topology. In the first stage, although computational time is the highest the lowest time step (i.e. Δt=0.0025s) is assumed as the reference one.

Table 3.5. Time Refinement Results at α=10° for Re=100,000

	Angle of Attack (α) = 10°			**Error (%) of α = 10°**		
	$\overline{C}_l$	$\overline{C}_d$	$\overline{C}_l/\overline{C}_d$	$\overline{C}_l$	$\overline{C}_d$	$\overline{C}_l/\overline{C}_d$
Δt=0.02s	0.8396	0.043058	19.4993	1.1444	0.0905	1.2363
Δt=0.01s	0.8399	0.043114	19.4809	1.1805	0.0394	1.1406
Δt=0.005s	0.8349	0.043092	19.3765	0.5782	0.0116	0.5897
Δt=0.003s	0.8300	0.043094	19.2611	0.0120	0.0069	0.0005
Δt=0.0025s	0.8301	0.043097	19.2612	–	–	–

Figure 3.7 represents how the behavior of aerodynamic coefficients changes with time for different time steps. Although the all time steps are converging around t*=500, their initial response of them is also examined. As seen in Figure 3.7 Δt=0.02s (blue line) converges worst than the others in the first phase of simulation. Moreover, lowering time steps results in better convergence characteristics for all time steps, and the simulations converge faster to their unique steady values. It is an expected result, but computational time is also needed to be considered for optimization. That's why, the mean values are investigated for two angles of attack (10° and 20°) briefly.

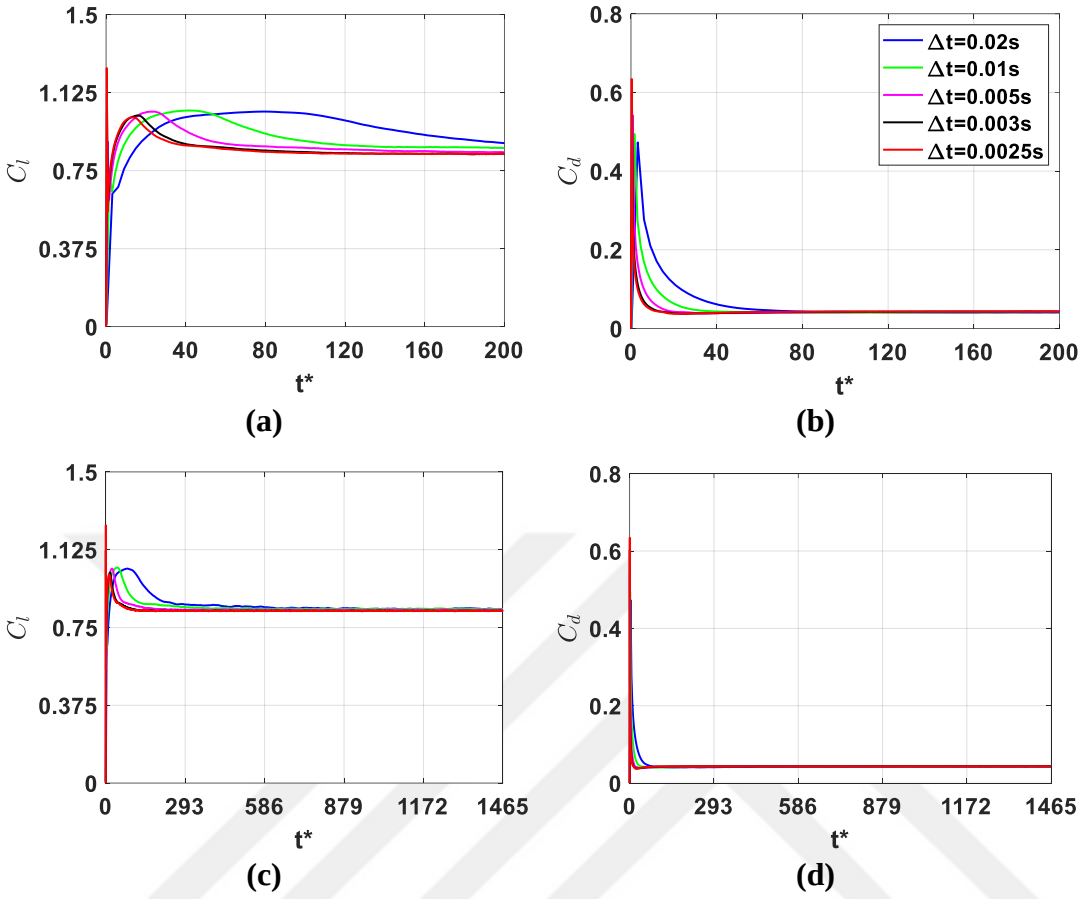

Figure 3.7. Instantaneous aerodynamic coefficients vs. t* (time refinement study) at α=10° for Re=100,000: a) lift coefficient in the time inverval of t*=[0s 200s], b) drag coefficient in the time inverval of t*=[0s 200s], c) lift coefficient in the time inverval of t*=[0s 1465s], d) drag coefficient in the time inverval of t*=[0s 1465s]

As seen in Table 3.5 in the first stage, because the unstable effects are not introduced at the relatively lower incidence angles, the mean drag coefficients do not change appreciably with different time steps at 10° angle of attack. And, there exists a non–linear trend between the aerodynamic coefficients. It means that one can not directly say that the lower time step converges to the reference value in "magnitude", but the error value shows converging characteristics with the lower time step as expected.

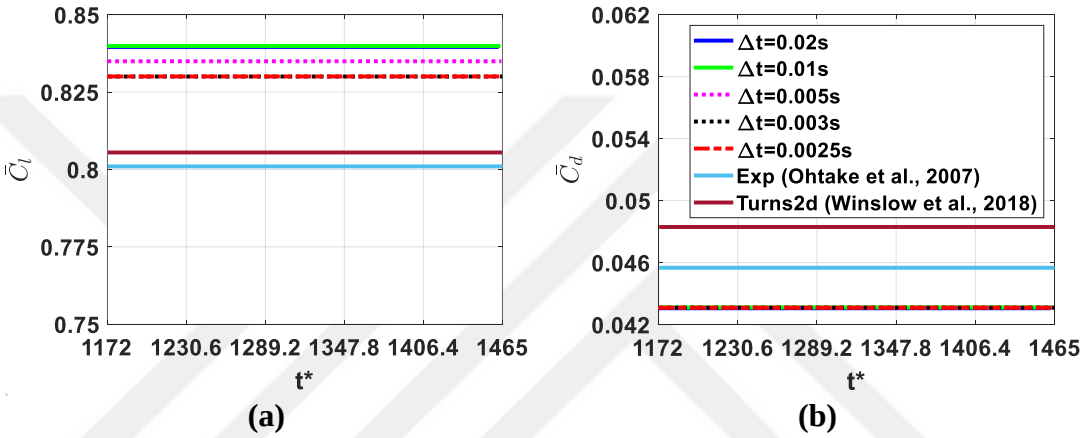

Figure 3.8. Mean aerodynamic coefficients vs. t* (time refinement study) at α=10° for Re=100,000: a) lift coefficient, b) drag coefficient

In addition, the $\bar{C}_d$ value has already converged under a 0.1% error with t=0.02s, and its absolute value is quite small numerically, thus the numerical errors listed in Table 3.5 are not confusing. At 20° angle of attack, the time–step has proportional relation for $\bar{C}_d$ both magnitude and error as shown in Table 3.6. However, $\bar{C}_l$ shows unexpected behaviour for 20° angle of attack. Decreasing the time step gives more error up to Δt=0.003s relatively Δt=0.0025s. In addition to that, the error magnitudes of mean aerodynamic coefficients are higher than 12% and 15% for $\bar{C}_l$ and $\bar{C}_d$ respectively. In order to clarify this situation, in this section a literature comparison (Table 3.7) which is referenced by experimental results is also added. Although the numerical solutions of Winslow et al. (2018) with TURNS2D (Transonic Unsteady Rotor Navier–Stokes 2D) converge better (6.7137% error) for

$\bar{C}_l$ than this work with Δt=0.003s (9.4243% error), there exists a huge difference in $\bar{C}_d$ between the results of Δt=0.003s and TURNS2D. This work with Δt=0.003s converges better than TURNS2D with almost 6 times lesser error.

Moreover, according to experimental data from Ohtake et al. (2007), which are displayed in Table 3.7, Δt=0.003s offers a smaller inaccuracy than Δt=0.005s. However, the Δt=0.0025s time–step clearly gives out–of–tolerance results for both $\bar{C}_l$ and $\bar{C}_d$. That's why, the Δt=0.003s time–step is preferred instead of Δt=0.005s and Δt=0.0025s.

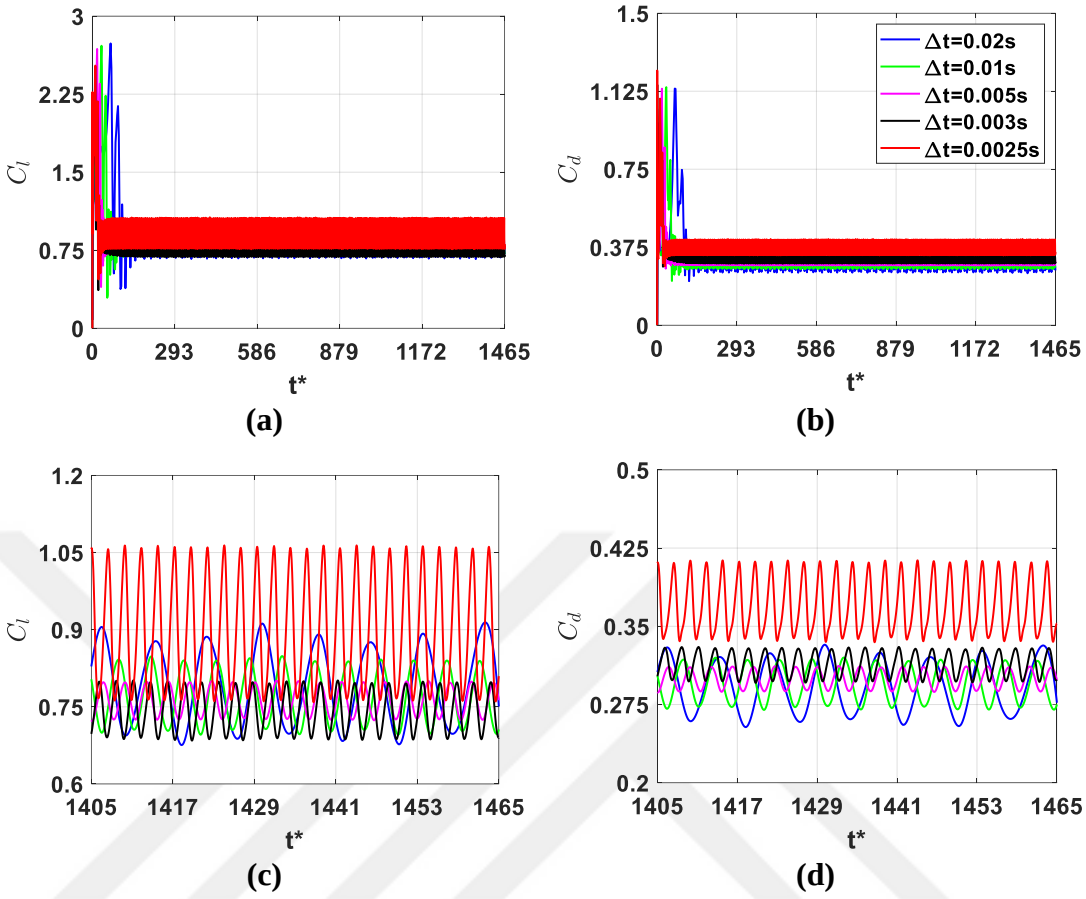

Figure 3.9. Instantaneous aerodynamic coefficients vs. t* (time refinement study) at α=20° for Re=100,000: a) lift coefficient in the time inverval of t^*=[0s 1465s], b) drag coefficient in the time inverval of t^*=[0s 1465s], c) lift coefficient in the time inverval of t^*=[1405s 1465s], d) drag coefficient in the time inverval of t^*=[1405s 1465s]

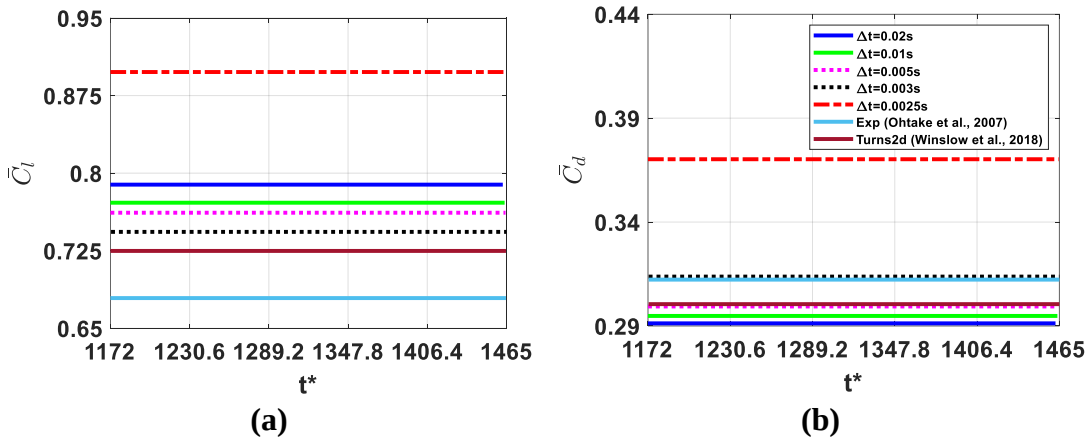

Figure 3.10. Mean aerodynamic coefficients vs. t* (time refinement study) at α=20° for Re=100,000: a) lift coefficient, b) drag coefficient

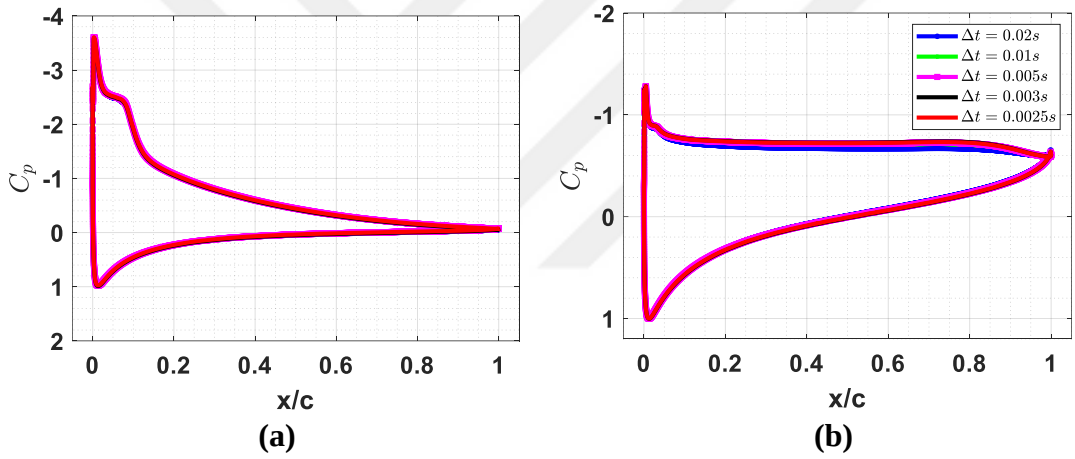

Figure 3.11. Mean pressure distributions around NACA 0012 with different time steps for Re=100,000: a) α=10°, b) α=20°

Table 3.6. Time Refinement Results at α=20° for Re=100,000

	Angle of Attack (α) = 20°			**Error (%) of α = 20°**		
	$\overline{C}_l$	$\overline{C}_d$	$\overline{C}_l/\overline{C}_d$	$\overline{C}_l$	$\overline{C}_d$	$\overline{C}_l/\overline{C}_d$
Δt=0.02s	0.7889	0.29126	2.7085	12.1296	21.3299	11.6948
Δt=0.01s	0.7714	0.29483	2.6165	14.0766	20.3657	7.8974
Δt=0.005s	0.7614	0.29939	2.5443	15.1548	19.1340	4.9207
Δt=0.003s	0.7432	0.31375	2.3688	17.2187	15.2554	2.3095
Δt=0.0025s	0.8978	0.37023	2.4248	–	–	–

Until now there exists necessary information for selecting Δt=0.003s time step. The Δt=0.0025s or lesser time steps are not considered in this situation. Because below than Δt=0.003s time step, the mean aerodynamic coefficients diverge from the experimental results. In other words, the time step and error of mean aerodynamic coefficients behave like parabolic characteristics and Δt=0.003s looks local maximum point.

Table 3.7. Time Step Comparison Results with Literature Data at α=20° for Re=100,000

	Angle of Attack (α) = 20°			**Error (%) of α = 20°**		
	$\overline{C}_l$	$\overline{C}_d$	$\overline{C}_l/\overline{C}_d$	$\overline{C}_l$	$\overline{C}_d$	$\overline{C}_l/\overline{C}_d$
Δt=0.005s	0.7614	0.29939	2.5443	12.1525	4.1338	16.9888
Δt=0.003s	0.7432	0.31375	2.3688	9.4228	0.4642	8.9186
Δt=0.0025s	0.8978	0.37023	2.4248	32.1849	18.5494	11.5019
TURNS2D (Winslow et al., 2018)	0.7248	0.3005	2.4119	6.7137	2.5392	7.5169
EXPERIMENTAL (Ohtake et al., 2007)	0.6792	0.3123	2.1748	–	–	–

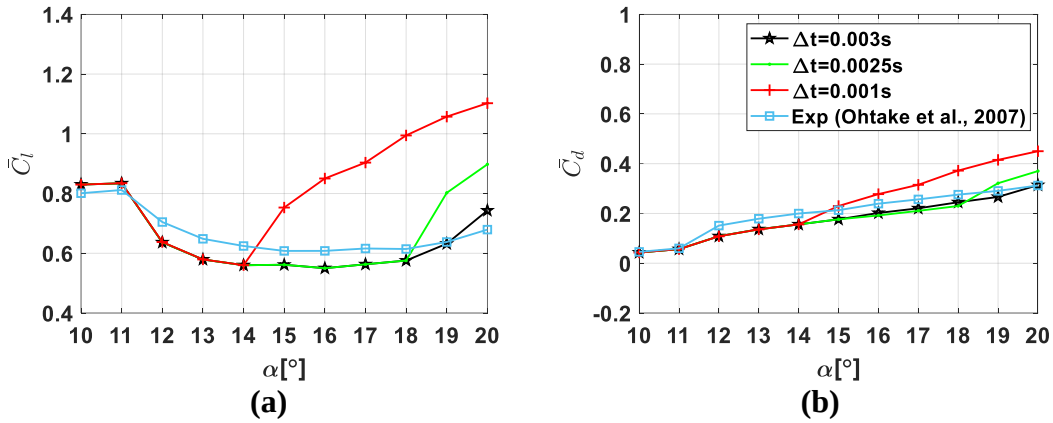

Figure 3.12. Mean aerodynamic coefficients vs. α for detailed time step comparison for Re=100,000: a) lift coefficient, b) drag coefficient

Still, the detail time-step and angle of attack sweep studies are conducted to ensure for selection the correct time step, because the correct time step is one of the major parameters to get better solutions for unsteady aerodynamic simulations.

Figure 3.12 shows how different time steps change the mean aerodynamic coefficients in the post–stall region as detailed version. With changing the time step, solutions are not almost changed up to 14° angle of attack. This shows that time step selection becomes more important for unsteady/unattached flows than relatively lower angles of attack. For Δt=0.001s, the slope of mean aerodynamic coefficients and angles of attack starts to increase just after 14°, and is clearly divergent with increasing angles of attack. For Δt=0.0025s, this pattern is similar, but the slope changes after an angle of attack of 18°.

3.4 Turbulence Intensity Selection

Another measure for aerodynamic study is turbulence intensity (*Tu*), which expresses the proportion of the intensity of velocity variations (root-mean-square) to mean freestream velocity. High-performance wind tunnels can achieve very low turbulence levels, usually under 1%; for general wind tunnels and low–speed flow typical values are between 2% and 7%; for high–speed flow inside of complex geometries such that exchangers and rotating types of machinery, typical values between 10% and 20%.

Moreover, since the flow is unstable for rotating types of machinery and external high incidence angles flow over an airfoil, the turbulence intensity changes continuously (Wang et al., 2011). Also, for airfoils at Re=10^4–10^5, increasing T_u may enhance their dynamic performance of them (Hoffman, 1991; Mish et al., 2001; Gilling et al., 2009; Mckeough et al., 1980). Moreoever, for very low Re flows stall and separation bubbles may disappear by increasing turbulence intensity (Huang & Lin, 1995), which are not the scope of this work. However, it is obvious that for predicting airfoil performance in detail, the turbulence intensity effect also needs to be well–defined. For the turbulence intensity calculation the following formula may be used. In this formula, U_∞ means the freestream velocity, the u' and v' stand in for the fluctuating velocities in x and y directions, respectively.

$$Tu = \frac{\sqrt{u'^2+v'^2}}{U_\infty} \tag{15}$$

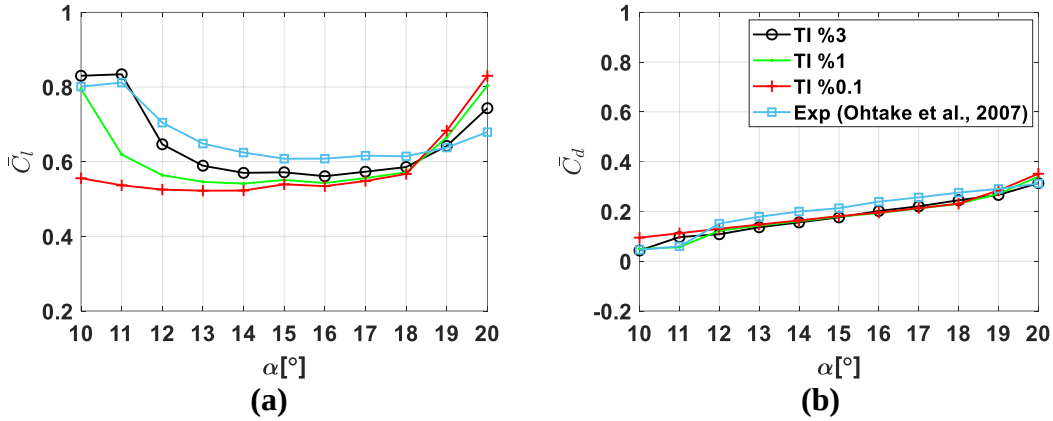

Figure 3.13. Turbulence intensity effect on mean aerodynamic coefficients vs. α for Re=100,000: a) lift coefficient, b) drag coefficient

Although the solutions of this effort converge to experimental findings of Ohtake et al. (2007) better than previous numerical study of Winslow et al. (2018) in terms of mean aerodynamic coefficients, it is important to understand how turbulence instensity changes the characteristics. Angle of attack sweep study is conducted for fixed Reynolds number (Re=100,000) between 10° and 20° angles of attack. There is no huge differences for $\bar{C}_d$ as presented in Figure 3.13(b), but turbulence intensity lower than 3% results show more divergence characteristics from Ohtake et al. (2007) in terms of $\bar{C}_l$.

3.5 Comparison of Turbulence Models

As explained previously, choosing the right turbulence model is another crucial step to effectively represent the flow. For the turbulence models, the accuracy-versus-computational-time trade-off is particularly important, because the different turbulence models which are described previously directly use different mathematical approaches to capture real flow physics. With the increase in equations of turbulence modeling, the solutions are converging to real values better. But, even at each iteration one needs to solve more equations/unknowns, so computational time becomes longer for each iteration. That's why, the most of literature work is also conducted with Spallart Allmaras or *k–ω* SST turbulence models rather than Transition–SST turbulence model.

For this work, the turbulence model selection is not just conducted at specific angles of attack as in grid and time refinement study, because it may mislead for stall and post–stall characteristics. That's why, unsteady simulations are conducted between [0° 20°] angles of attack with 1° increment at Re=$4x10^4$ and $1x10^5$. These Reynolds numbers are selected because this work covers Re=$4x10^4$–$1x10^5$.

Re=$4.8x10^4$–$2.5x10^5$ regimes for NACA 0012 and SD 7003 airfoils with *k–kl–ω*, *k-ω* SST, and Transition-SST turbulence models were covered by Counsil and Boulama (2012, 2013) and Genc et al. (2008). Moreover, Genc et al. (2008) used the *k–kl–ω* and Transition–SST turbulence models at Re=$2x10^5$ for NACA 2415 and investigated the leading edge slat mechanism effect, the solutions were compared with previous experimental results then it is validated that *k–kl–ω* model also can predict accurately lift slope and stall characteristics. On the other hand, the the lift slope prediction capability of the *k–ω* SST turbulence model is lacking. Although Counsil and Boulama (2012, 2013) showed the solutions until 8°, Genc et al. (2008) made his analyses until the 20° angle of attack.

On the other hand, Winslow et al. (2018) used Spallart–Allmaras turbulence model in his TURNS2D tool and compared the outcomes of Ohtake et al. (2007). The

solutions for different airfoils show sufficient similarity with experimental results between Re=10^4–10^5. Without a large-Edddy or a detached Eddy simulation, the results of Winslow et al. (2018) stayed limited for near stall conditions.

In short, there exist some publications about the validity of different turbulence models, their effects on airfoil/wing performance, or how they successfully capture the transition mechanism. Some of them are discussed in previous chapters of this work in detail, however, there is still a need of analysing different turbulence models for this particular work. Unsteady aerodynamics analysis results directly depend on input parameters, and non–existence work which has exactly the same simulation inputs as this work in literature, so it is better to investigate each turbulence model. According to the error in magnitude and trend of mean aerodynamic coefficients, the proper turbulence model is selected and detailed solutions will be discussed using it.

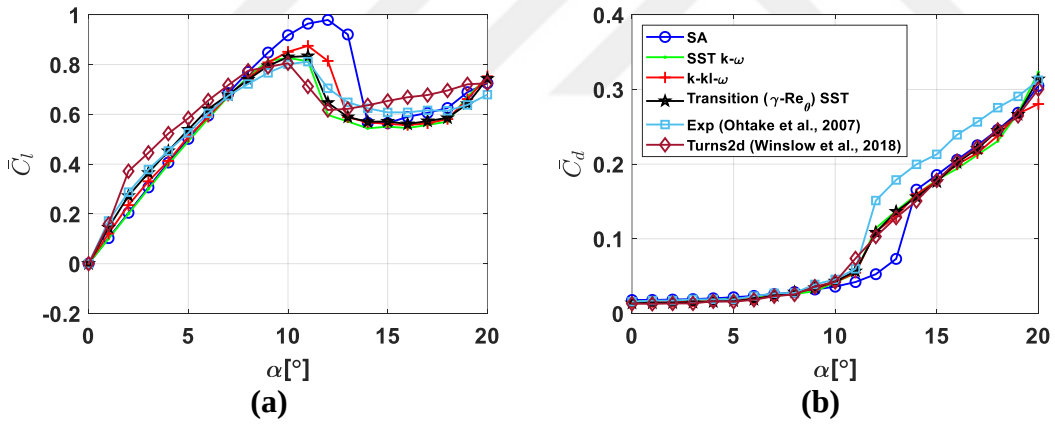

Figure 3.14. Mean aerodynamic coefficients vs. α for turbulence model comparison for Re=100,000: a) lift coefficient, b) drag coefficient

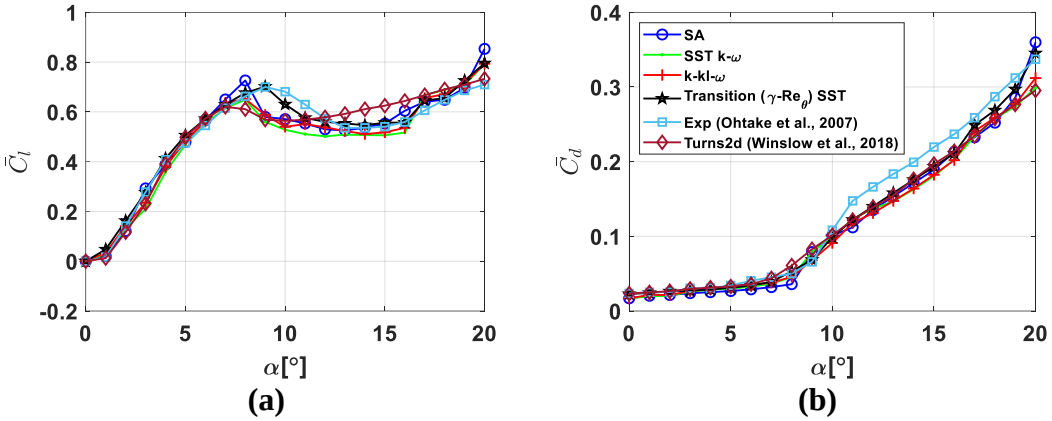

Figure 3.15. Mean aerodynamic coefficients vs. α for turbulence model comparison for Re=40,000: a) lift coefficient, b) drag coefficient

For both Reynolds numbers, the turbulence models showed mostly common features. Likewise, Carmichael (1981) and Choudhry et al. (2015) mentioned, lift and drag are well approximated by SA turbulence model, but flow physics are not. The Cp distributions also show differences between other turbulence models for not only leading–edge portion of airfoil surface but also clearly full suction part distribution. The discrepancies also grow as the incidence angle and Reynolds number are reduced. Additionally, in the quasi–linear $\bar{C}_l$ vs α region, although the SA turbulence model gives a better approximation than TURNS2D still underestimates lift to a 6° angle of attack. The term "quasi" is used because, in contrast to the high Reynolds numbers, the lower Reynolds numbers also entail the separation bubble on the airfoil's top surface at lower incidence angles (even below 8°). Therefore, the transition point on the airfoil surface is altered as a separation bubble goes up between the trailing edge and the leading edge, and this naturally affects the mean aerodynamic coefficient value.

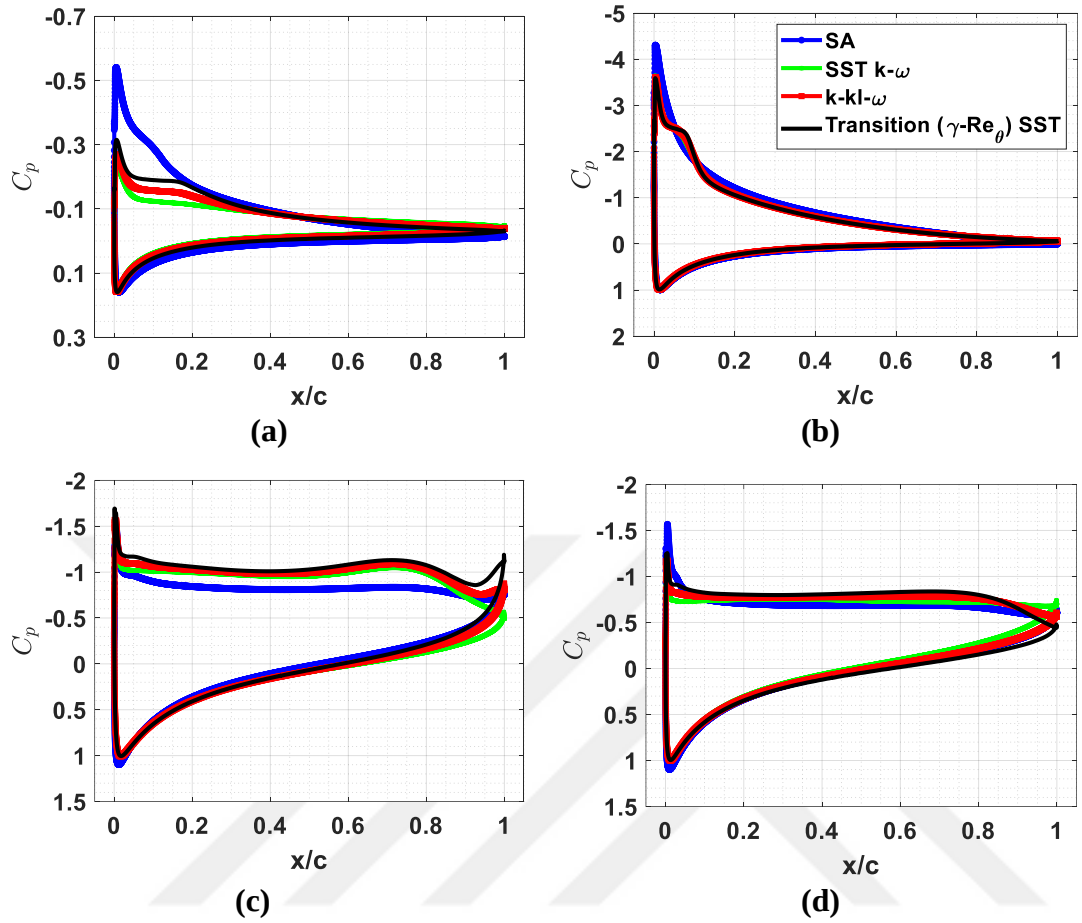

Figure 3.16. Mean pressure distributions around NACA 0012 with different turbulence models for Re=40,000 and Re=100,000: a) α=10° and Re=40,000, b) α=10° and Re=100,000, c) α=20° and Re=40,000, d) α=20° and Re=100,000

The SA turbulence model predicts better quasi–linear $\bar{C}_l$ vs α region for lower Re. The variation in $\bar{C}_l$ relative to the experimental result is almost dissipating for Re=40,000. However, this time $\bar{C}_d$ gives lower value than other turbulence model results, up to 8° angle of attack. Additionally, the SA model predicts a stall angle of 9° for Re=40,000, which is 1° lower than the findings of the experimental and Transition-SST model. This outcome has been similar to the *k–ω*–SST and the *k–kl–ω* turbulence models. In other words, they both estimate stall angle 1° lower than experimental and Transition–SST turbulence model results. Still, all of these turbulence models predict stall angle better than TURNS2D (7° stall angle prediction for Re=40,000 flow). In conclusion, although the results of this work

predict mean aerodynamic coefficients better than previous study up to stall region, one of the turbulence model, i.e. Transition–SST, gives more accurate results than other models as expected. So, for both $\bar{C}_l$ and $\bar{C}_d$, the experimental results may be validated with high fidelity by using the Transition–SST turbulence model.

For stall region, Winslow et al. (2018) finds the stall angle 1° and 2° before than experimental outcomes of Ohtake et al. (2007). The SA turbulence model overpredicts the eddy viscosity and it results in dissipation at high rates in the flow. If the solutions want to be improved by using SA turbulence model, detached Eddy simulation or large–eddy simulation should be introduced to the existence model (Winslow et al., 2018). Although *k–ω*-SST and *k–kl–ω* turbulence models exactly capture the stall angle, the SA turbulence model predicts stall angle 1° after experimental results for Re=100,000. Moreover, for the SA turbulence model, $\bar{C}_{l_{max}}$ diverges up to approximately 25% concerning experimental results which is dissatisfactory. In addition to that, except the Transition–SST turbulence model, all models fail to capture stall angle for Re=40,000, and up to now, there is no significant observation about the differences between *k–ω–*SST and *k–kl–ω* turbulence models. In conclusion, by putting together the experimental data of Ohtake et al. (2007), Transition-SST is a special turbulence model that can forecast the flow's stall characteristics.

For the post–stall region, the consistency between *k–ω–*SST and *k–kl–*omega turbulence models continues, also the general trend of mean aerodynamic coefficients concerning the incidence angle is similar to the Transition–SST turbulence model. But, the mean aerodynamic coefficient errors are less in magnitude for the Transition–SST turbulence model, and especially at high incidence angles, pressure distributions of Transition–SST turbulence model show different dispositions for both Reynolds numbers. Results are remarkably similar to earlier numerical studies for $\bar{C}_d$ values at high incidence angles, and the trend may also be maintained by utilizing discussed Transition-SST turbulence model. However, as mentioned before, there exists almost constant bias relative to

experimental study. This bias is acceptable by looking at other studies in the literature and will be thoroughly covered.

In conclusion, by investigating quasi–linear, stall, and post–stall regions, the most confidential turbulence model is observed as the Transition–SST turbulence model. This was an expected result because the mathematical equations which are running in the background of this model are more sophisticated than the other models. Traditional turbulence models based on one and two equations miss transition and produce inaccurate findings at low Reynolds numbers (Rumsey & Spalart, 2009 Wang et al., 2012). As opposed to that, four–equation–based Transition–SST turbulence model covers not only instantanenous and mean flow properties, but also the separation bubble position, transition mechanism, the wake features, and reattachment of the shear layer (Menter et al., 2006; Council & Boulama, 2012).

Lastly, the results of Transition–SST turbulence model show that not only reliable estimation of the mean aerodynamic coefficients for all angles of attack but involves some differences in terms of pressure distribution over airfoil surface for 10° and 20° incidence angles. The validation study for both non–dimensional forces and pressure distribution is necessary to complete the discussion, before making comments about the detailed results.

3.6 Validation Study

Since the NACA profiles are commercial, there exist numerous published numerical and experimental findings. That's why, the validation study is conducted both the computational study of Winslow et al. (2018) and the experimental study of Ohtake et al. (2007). As stated previously, these two works are well known in the literature and cited/validated by many types of research; so are selected for detailed comparison. However, the literature's more experiamental and numerical findings are also compared with this work in this part.

The numerical simulations are conducted via TURNS2D (Transonic Unsteady Rotor Navier–Stokes 2D) by Winslow et al. (2018). This internal-developed fluid dynamics solver (Srinivasan & Baeder, 1992) runs the Spalart-Allmaras (SA) turbulence model as laminar-turbulent transition model (Medida & Baeder, 2011). That's why, the numerical solutions are expected to have more accurate flow transition physics forecasting than FLUENT's SA model. Thus, the results are expected to be more reliable than a common commercial tool (i.e. FLUENT) within the same circumstances.

Firstly, results were compared at specific incidence angles (10° and 20°) for Re=100,000 as is explained in Time refinement result section. Then, the angle of attack sweep study was carried out for Re=100,000 to see whether detailed time step selection changes solutions or not. For the angle of attack sweep study, the angles were chosen between 10° and 20° are selected, because unsteady behavior and separation are dominant for incidence angles. In this part, the validation is taken a step further, and independent studies/tools are shown together with this work. But first, the chosen configuration comparison, in same angles of attack (10° and 20°) is tabulated as follows:

Table 3.8. Aerodynamic Coefficients Comparison with Literature Data at α=10° for Re=100,000

	Angle of Attack (α) = 10°			**Error (%) of α = 10°**		
	$\bar{C}_l$	$\bar{C}_d$	$\bar{C}_l/\bar{C}_d$	$\bar{C}_l$	$\bar{C}_d$	$\bar{C}_l/\bar{C}_d$
Medium 2	0.8300	0.043094	19.2611	3,6254	5,6404	9,8198
TURNS2D (Winslow et al., 2018)	0.8055	0.042300	19.0425	0,5618	7.3790	8.5734
Experimental (Ohtake et al., 2007)	0.8010	0.045670	17.5388	–	–	–

Both Table 3.8 and Table 3.9 show that TURNS2D gives relatively lower errors, for both angles of attack, in terms of $\bar{C}_l$ than this work. However, Figure 3.14 shows more realistic results for $\bar{C}_l$ to understand the big picture. The general $\bar{C}_l$ trend is dissimilar for TURNS2D by comparing the experimental findings of Ohtake et al. (2007). This is not valid for only above 10° angles of attack, but also the quasi–linear region of $\bar{C}_l$ vs α graph. However, this situation is not the case for the present work, so this work declares better numerical solutions than TURNS2D in terms of $\bar{C}_l$ vs α characteristics of NACA 0012 2D profile for Re=100,000.

Table 3.9. Aerodynamic Coefficients Comparison with Literature Data at α=20° for Re=100,000

	Angle of Attack (α) = 20°			**Error (%) of α = 20°**		
	$\bar{C}_l$	$\bar{C}_d$	$\bar{C}_l/\bar{C}_d$	$\bar{C}_l$	$\bar{C}_d$	$\bar{C}_l/\bar{C}_d$
Medium 2	0.7432	0.31375	2.3688	9.4243	0.4642	10.5672
TURNS2D (Winslow et al., 2018)	0.7248	0.3005	2.4119	6.7137	3.7784	10.904
Experimental (Ohtake et al., 2007)	0.6792	0.3123	2.1748	–	–	–

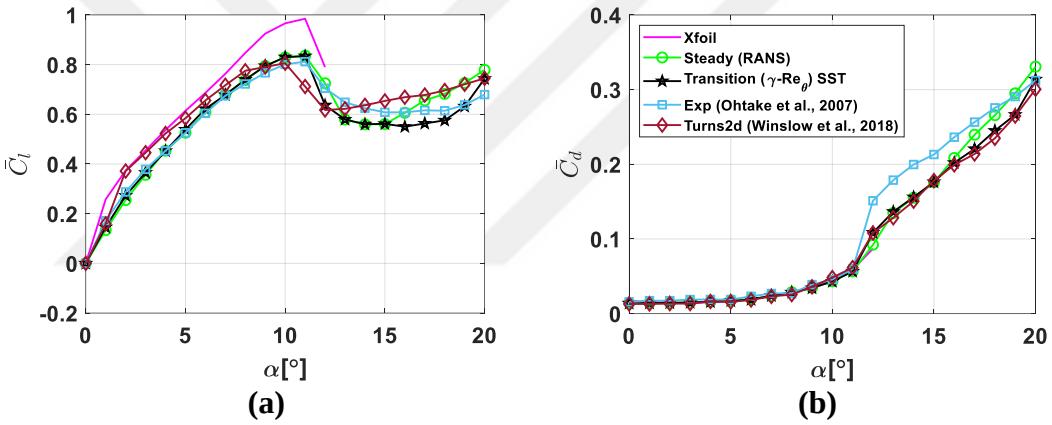

Figure 3.17. Mean aerodynamic coefficients vs. α comparison with different simulation methods for Re=100,000: a) lift coefficient, b) drag coefficient

The mean aerodynamic coefficients are compared in the results above concerning the angle of attack for both Xfoil, steady, and unsteady solutions (Figure 3.17). For validation study, unsteady outcomes are compared with TURNS2D and experimental findings. However, the Xfoil and steady solutions have also some characteristics which deserved to be emphasize.

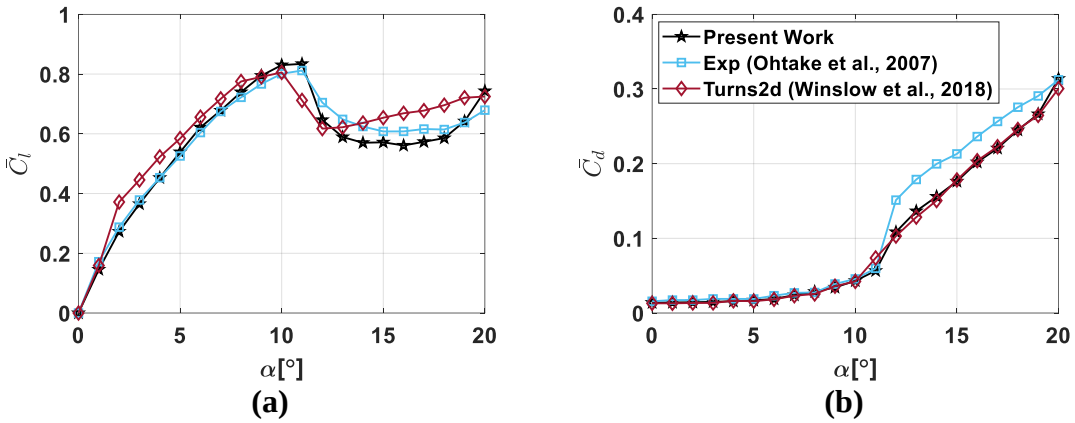

Figure 3.18. Mean aerodynamic coefficients vs. α comparison with literature for Re=100,000: a) lift coefficient, b) drag coefficient

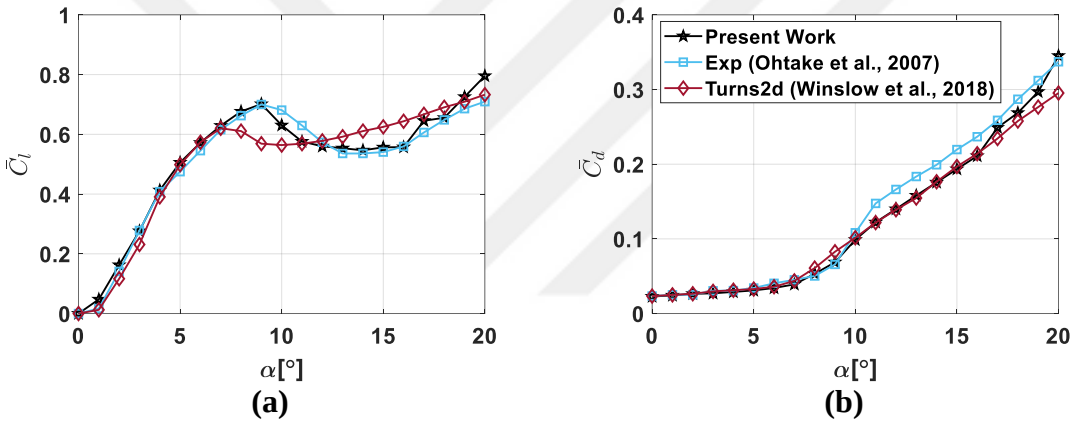

Figure 3.19. Mean aerodynamic coefficients vs. α comparison with literature for Re=40,000: a) lift coefficient, b) drag coefficient

As mentioned previously, the $\bar{C}_l$ vs α characteristics is not purely linear for solutions of TURNS2D, especially after 2° angle of attack there exists a breakdown that does not be observed as much as for the experimental study. Although the Xfoil shows a similar trend just after 1° angle of attack, unsteady results show a directly coherent results with the experiment. Moreover, the overestimation in $\bar{C}_l$ of TURNS2D shows more divergence characteristics for Xfoil solutions. This trend is similar to previous works which have compared Xfoil and experimental results (Yu et al., 2012; Aftab et al., 2016).

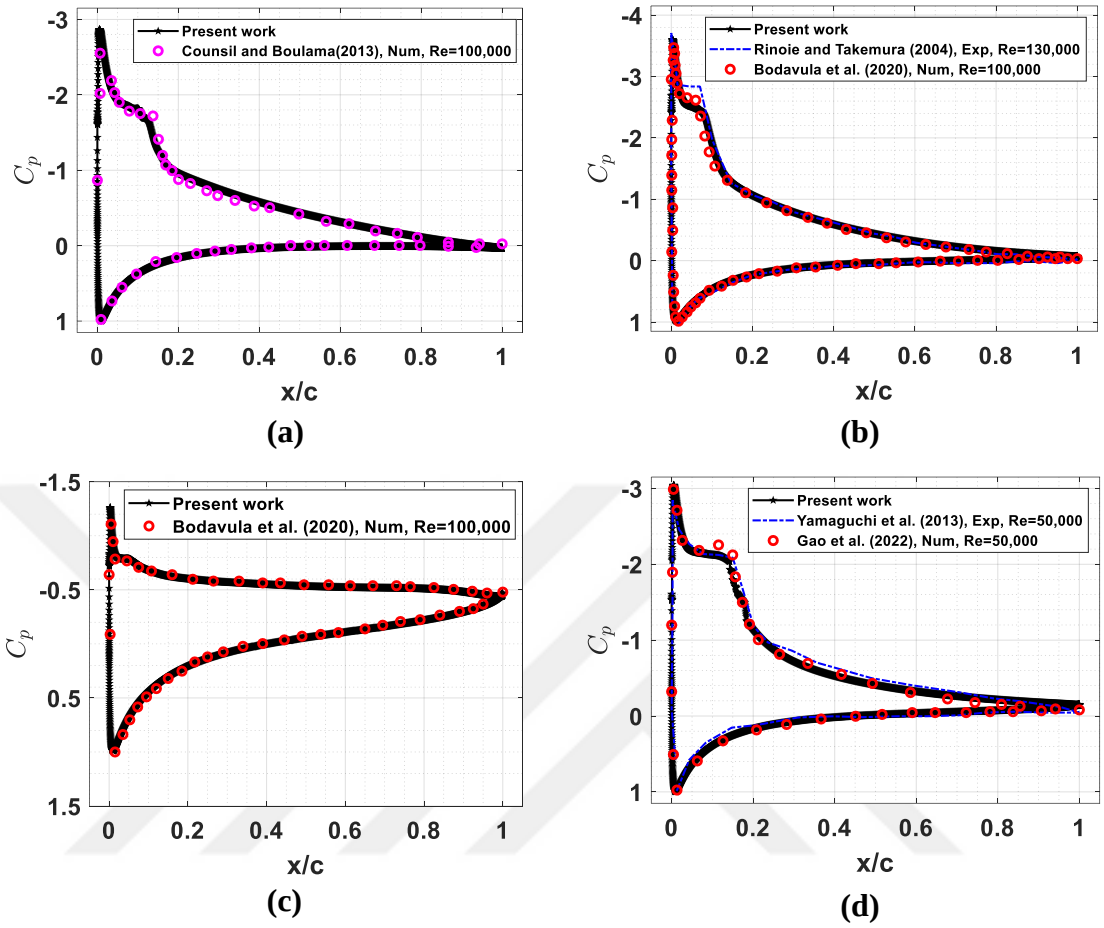

Figure 3.20. Mean pressure distributions around NACA 0012 with literature comparison for Re=100,000 and Re=50,000: a) α=8°, b) α=10°, c) α=16°, d) α=10°

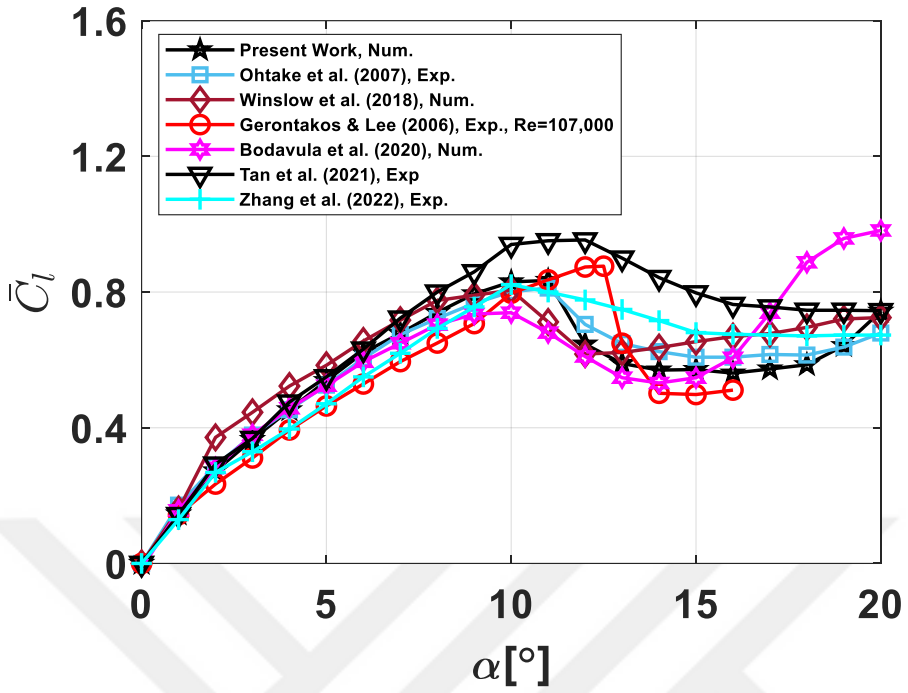

Figure 3.21. Mean lift coefficient vs. α comparison with literature for Re=100,000 (detailed version)

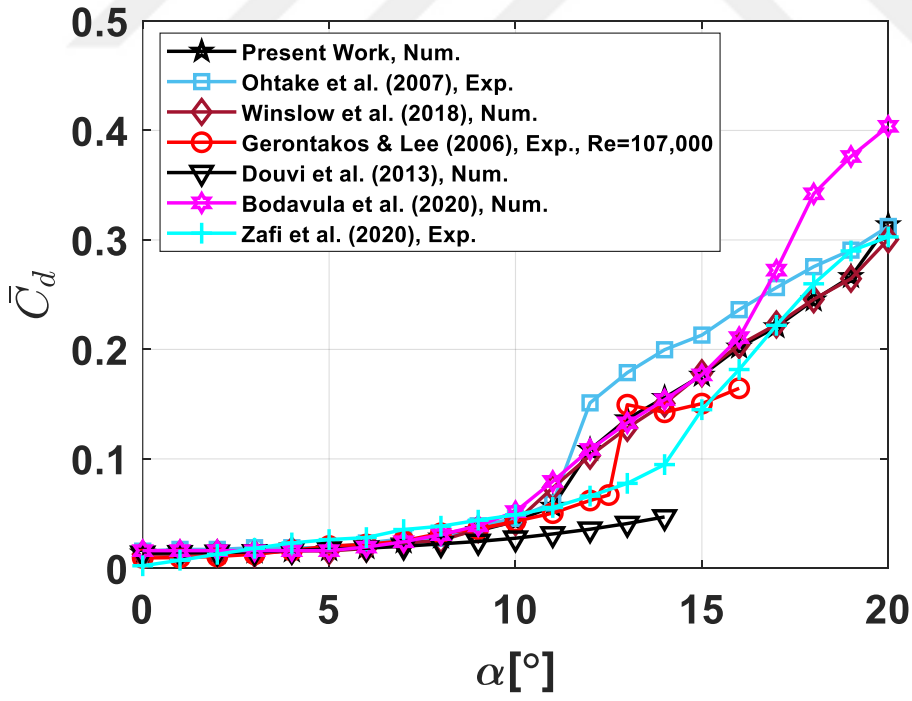

Figure 3.22. Mean drag coefficient vs. α comparison with literature for Re=100,000 (detailed version)

The error values in $\bar{C}_d$ of this work are better than previous numerical solutions, i.e. TURNS2D study, but the general trend is similar according to different incidence angles for Re=100,000. The bias relative to the experimental $\bar{C}_d$ is almost fixed from 10° to 20° angle of attack, and this may results from the differences between experimental–numerical approaches. Apart from that, the general trend and magnitude of mean aerodynamic coefficients are closer to experimental results than TURNS2D for Re=100,000.

The mean aerodynamic coefficients and surface pressure distributions at varied incidence angles are both the subject of the validation inquiry. The study's conclusions show that the information previously present in the literature is equivalent to the mean pressure distributions throughout the airfoil's surface at various incidence angles and Reynolds numbers. Additionally, the study intends to comprehend how well models and data from the literature already in existence can reflect flow characteristics, particularly around the stall angle and post-stall region. Most of the works in the literature focused on design parameters rather than capturing the flow's properties themselves. The simulation's outcomes are closer to those of well-known studies (Ohtake et al., 2007; Winslow et al., 2018). Overall, the validation study in this research project seems to be comprehensive and aimed to assess the accuracy of the simulation results thoroughly.

CHAPTER 4

RESULTS

NACA 0012 airfoil has been solved from Re=40,000 to Re=100,000 with an increment of 10,000 for investigating the unsteady aerodynamics around the airfoil by observing the mean aerodynamic coefficients, mean pressure distributions, mean streamlines, mean skin friction coefficients, and mean Strouhal numbers. In addition to that, instantaneous aerodynamic coefficients and wake patterns are also observed to complete the discussion. Additionally, 1° increment between 0° and 20° of incidence angles are used to calculate the findings. This enables us to see the NACA 0012 airfoil's aerodynamic properties for the pre-stall and post-stall regions in more depth. To sum up, the main goal of the investigation is to ascertain how Reynolds number and incidence angle impact the aerodynamic behavior of the NACA 0012 airfoil between Re=40,000 –100,000.

4.1 Aerodynamic Coefficients

Figure 4.1 shows the averaged aerodynamic coefficients for various incidence angles. The incidence angles are increased by 1°. As stated previously, aerodynamic coefficients are averaged between [8s 10s] which is equivalent to a non-dimensional time, $t^*=tU_\infty/c=[1172\ 1465]$. With the getting of aerodynamic results after t*=1172, the initial impulsive start effects have not been taken into account and only steady/quasi–periodic solutions are concerned.

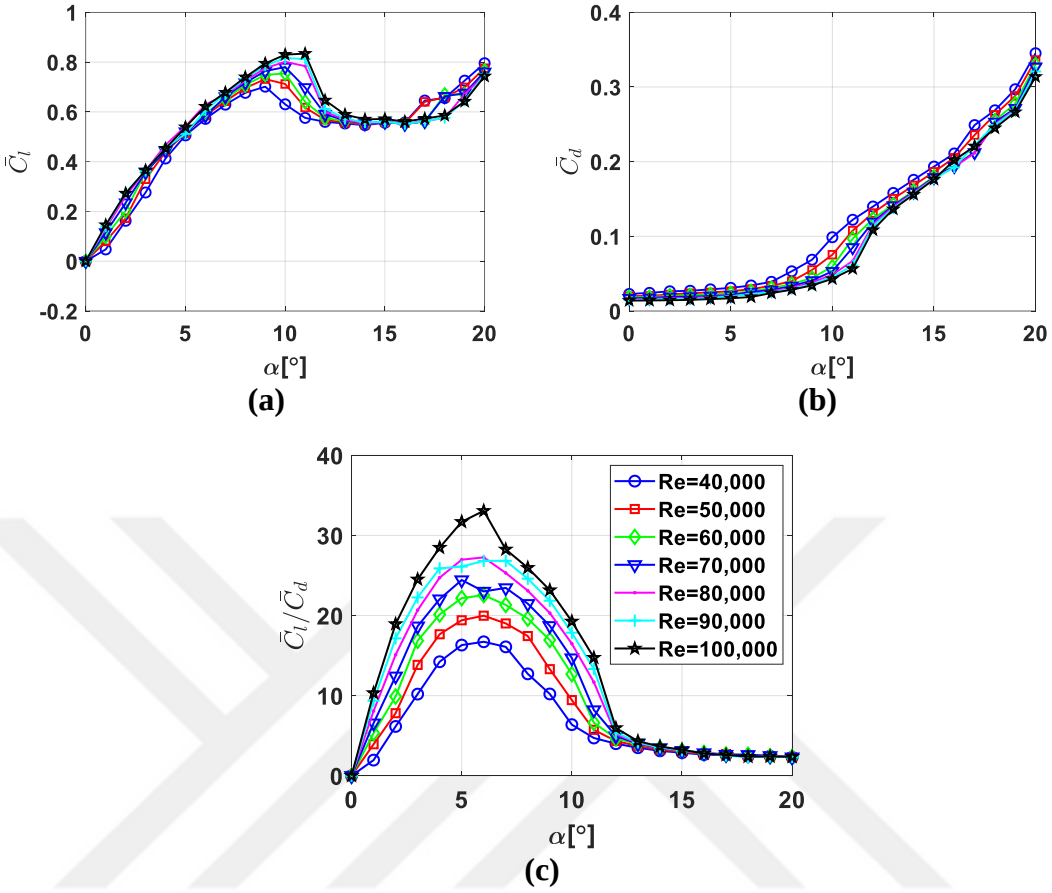

Figure 4.1. Mean aerodynamic coefficients vs. α comparison for different Reynolds numbers: a) mean lift coefficient, b) mean drag coefficient, c) mean lift to drag coefficient

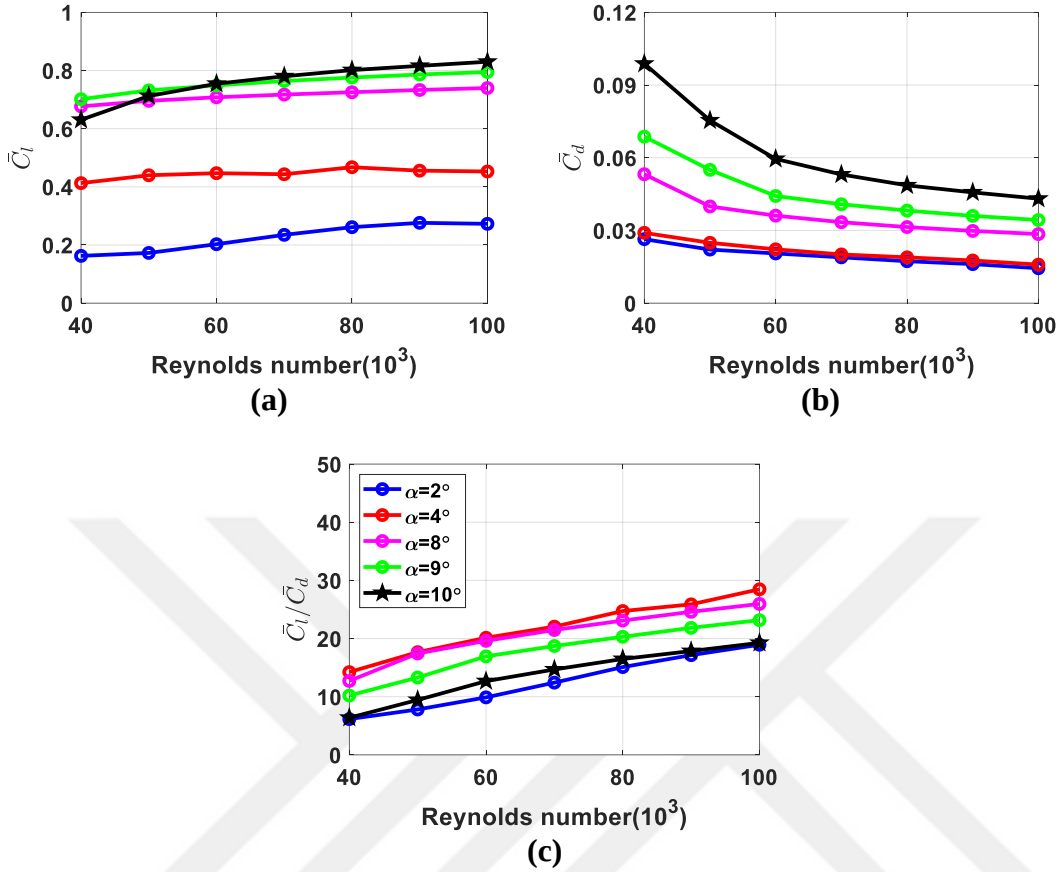

Figure 4.2. Mean aerodynamic coefficients vs. Reynolds number comparison for different angles of attack (quasi–linear region): a) mean lift coefficient, b) mean drag coefficient, c) mean lift to drag coefficient

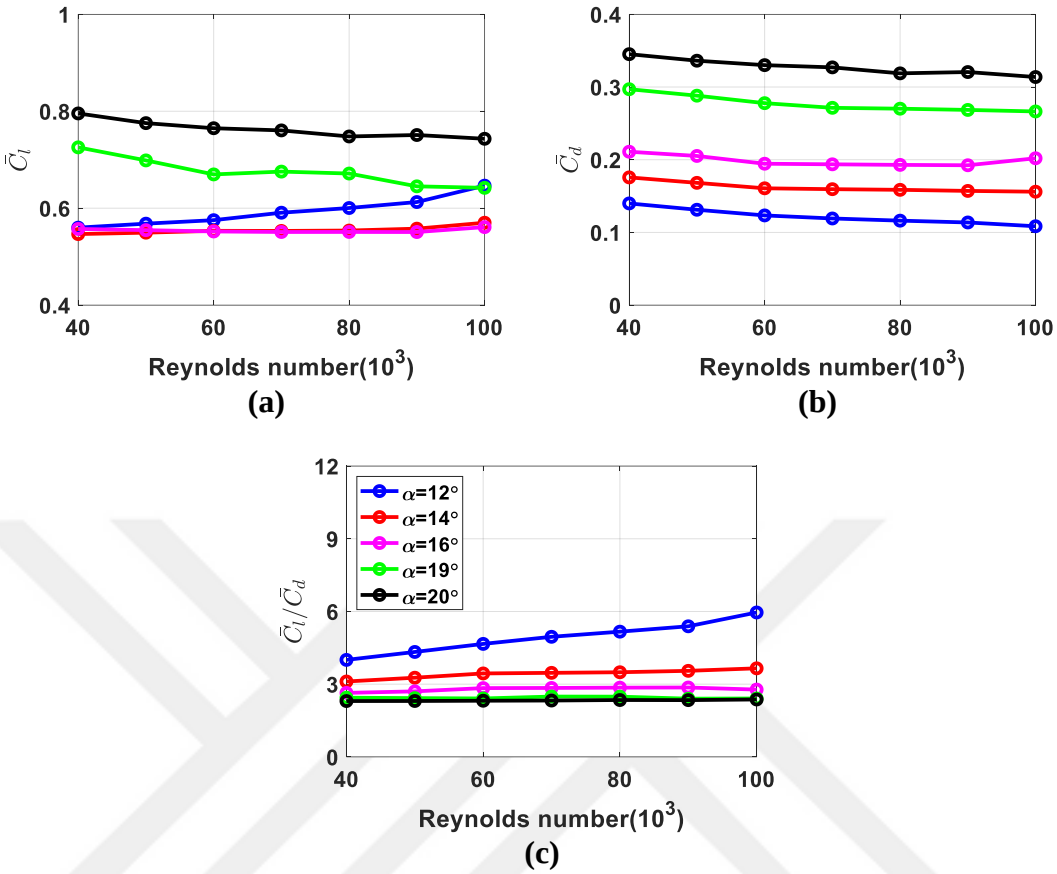

Figure 4.3. Mean aerodynamic coefficients vs. Reynolds number comparison for different angles of attack (post–stall region): a) mean lift coefficient, b) mean drag coefficient, c) mean lift to drag coefficient

4.1.1 Influence of angle of attack

The mean lift coefficient and incidence angle have a positive connection up to the stall angle (Figure 4.1). This relationship is not entirely linear, though. Especially for relatively lower Reynolds numbers, this non–linear behavior is increasing. The existence of bubbles on the upper airfoil surface in various places for different incidence angles may be the cause of this outcome (Ohtake et al., 2007).

The upper airfoil surface has a separation bubble that moves from the trailing edge to the leading edge of the airfoil for very low incidence angles. As a result, the point of flow transition is altered. Second, while the airfoil approaches the stall angle, a characteristic trailing edge separation bubble occurs until the top surface fully separates. These two different phenomena may explain the existence of different slopes when investigating the flow from 0° to stall angle of attack (i.e. non–linear/quasi–linear $\bar{C}_l$ vs α relation). Furthermore, as predicted, the drag coefficient's relationship with incidence angle is positively linear.

To better understand how the NACA 0012 airfoil performs aerodynamically, the $\bar{C}_l/\bar{C}_d$ vs. angle of attack is represented (Figure 4.1c). Around the 5°–6° angles of attack, $\bar{C}_l/\bar{C}_d$ has maximum values for each Reynolds number, but after these angles of attack, the mean drag coefficient starts to rise, so that $\bar{C}_l/\bar{C}_d$ starts to decrease. Finally, for higher incidence angles, the $\bar{C}_l/\bar{C}_d$ converges to a value that is essentially unaffected by the Reynolds number.

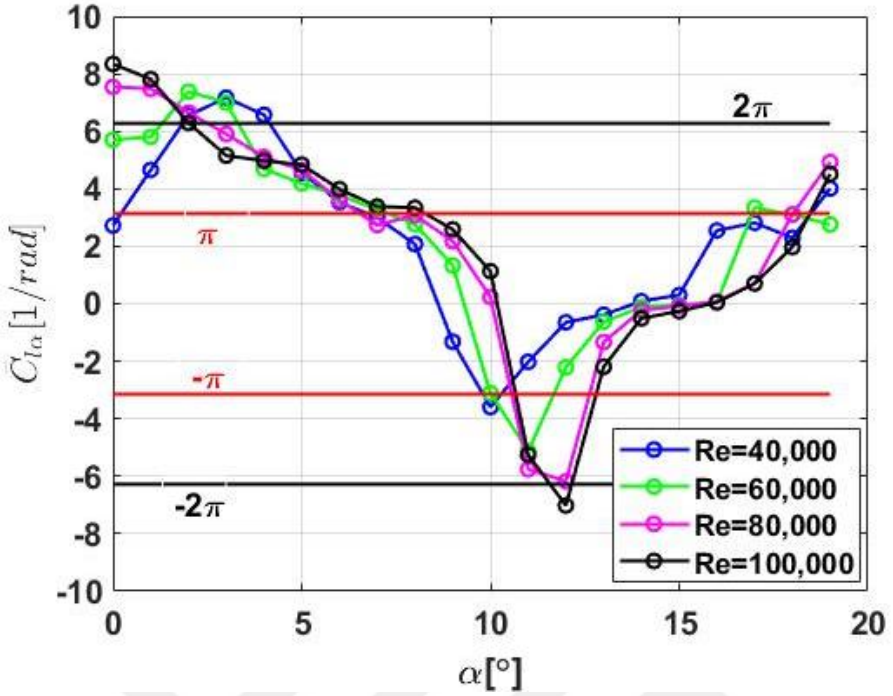

Figure 4.4. Lift slope at different incidence angles for different Reynolds numbers

The above figure represents how the slope of the mean lift coefficient with respect to the angle of attack changes relative to angle of attack for different Reynolds numbers. In general, up to the stall angle, the lift variation with respect to the incidence angle is decreasing. The main reason behind it may come from the existence of separation bubble becoming more dominant with increasing incidence angles. However, for very low Reynolds numbers (i.e. Re=40,000 and 60,000), the lift slope shows an increasing trend up to 4° and 3° incidence angles, respectively. Moreover, up to the 4° angle of attack, all flows have slopes close to the 2π, but the Reynolds number has an important effect especially at a very low incidence angle (i.e. 0°).

Since except for the 0° angle of attack, the slopes are calculated via the central difference method, the sign change is observed between the 1° incidence angle below than stall angle and the stall angle. For instance, Re=100,000 has a stall angle of 11°, and the black line represents that rapid decrease occur between 10°–11° angles of attack. Similarly, the green line shows this trend between 9°–10° angles of attack for 10° stall angle, and the blue line indicates between 8°–9° angles

of attack for 9° stall angle. However, the magenda line for Re=80,000 gives almost zero lift slope for at the stall angle, because the stall behavior is very smooth relative to the other Reynolds number flows.

4.1.2 Influence of Reynolds number

The airfoil's aerodynamic features are significantly influenced by Reynolds number, particularly at low Reynolds numbers. Figure 4.1 tells that for quasi–linear regions the drag coefficient falls as Reynolds number rises. This is valid, because for lower Reynolds numbers at an incidence angle, higher drag indicates early onset of flow separation. Also, with rising Reynolds numbers, the lift coefficient increases and stall angle delays. Moreover, the maximum mean lift coefficient, $\overline{C_l}_{max}$, rises with higher Reynolds numbers. Specifically, the stall angles are 11°, 10°, 10°, and 9° for Re=100,000; 80,000; 60,000, and 40,000, and corresponding $\overline{C_l}_{max}$ values are also 0.8341, 0.8159, 0.7543, and 0.7014, respectively.

At that point, it is important to review what is going on as its physics. Physically, inertial to viscous force ratio is defined as the Reynolds number. This reveals that the viscous forces prevail at low Reynolds number and the flow is more laminar. So, meanwhile the velocity flows are nearly linear for laminar flows (linear means that the velocity is zero at the top surface of airfoil and linearly increases to the value of the 0.99 x freestream flow velocity), because incoming flow and the boundary layer flow interact more in turbulent flows, the boundary layers are more parabolic. Thus, turbulent flows have a faster velocity profile in their boundary layers, so they have more energy (greater velocity at the same distance from the airfoil's surface). This increased energy has the effect of making turbulent boundary layers more resilient to negative pressure gradients, which causes delays in boundary layer separation and stall.

According to Figure 4.2, the Reynolds number barely affects the lift coefficient, but Figure 4.2(a) still shows that positive relationships between $\bar{C}_l$ and Reynolds

number in quasi–linear region. However, the more dominant point is about drag coefficient. The relationship between Reynolds number and $\bar{C}_d$ is inverse. It is indicating the early onset of flow separation for relatively lower Reynolds numbers that is not preferred.

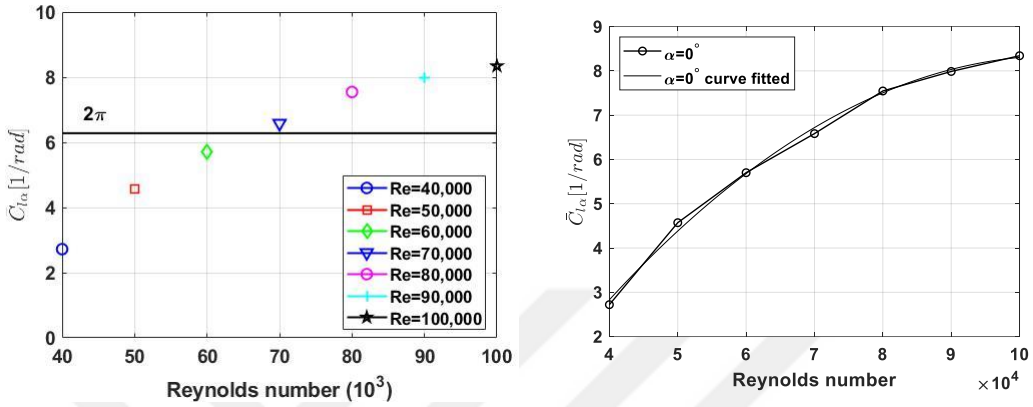

(a) **(b)**

Figure 4.5. Lift slope at α=0° for different Reynolds numbers: a) original form, b) comparison with curve fitted version

As stated previously, the Reynolds number has an important effect on lift slope with respect to the incidence angle. From the thin airfoil theory, the 2π line can be seen in Figure 4.5. For very low Reynolds number flows, the slope is under this threshold value, but with greater Reynolds number, the slope is passing over it. That's why, a curve may be fitted and formulated as a dependent variable of the Reynolds number for a fixed incidence angle (i.e. α=0°) as follows:

$$At\ \alpha=0^\circ \quad : \quad \bar{C}_{l_\alpha} = -1.28x10^{-9}Re^2 + 0.0002704\,Re - 5.938 \tag{16}$$

where 40,000 < Re < 100,000

4.2 Pressure Distributions

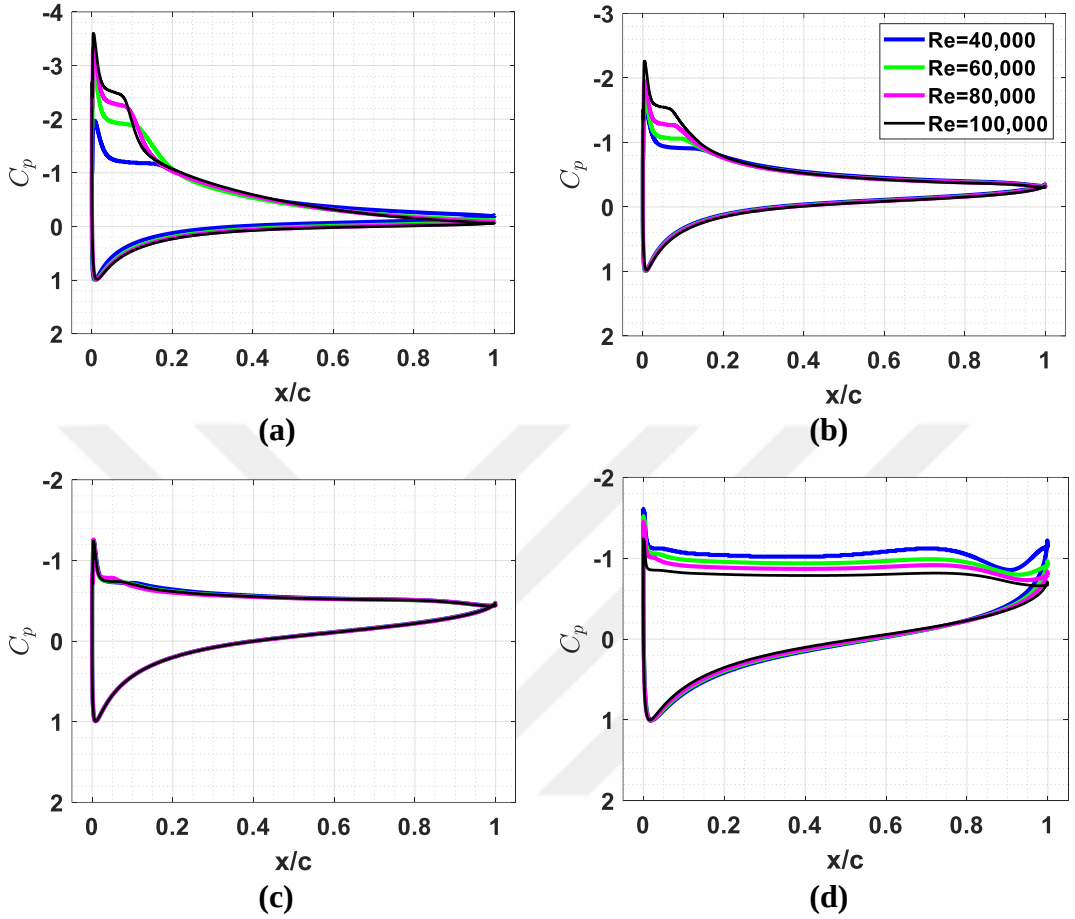

Figure 4.6. Mean pressure distributions around NACA 0012 with different Reynolds numbers: a) α=10°, b) α=12°, c) α=16°, d) α=20°

4.2.1 Influence of angle of attack

In Figure 4.6, pressure distributions around the NACA 0012 airfoil are obtained and displayed for various Reynolds numbers for near-stall and post-stall incidence angles. Because the airfoil exhibits post-stall characteristics and lift diminishes, lower and upper surfaces are less different when the incidence angle increases. Moreover, the upper surface pressure distribution becomes flatter with rising incidence angles between 10°–20° angles of attack, which means that separation covers all surfaces and kills the pressure gradient.

4.2.2 Influence of Reynolds number

According to the discussion of the mean aerodynamic coefficient, after the matching stall angles, the discrepancies between the aerodynamic coefficients for different Reynolds number flows are reducing. The pressure distributions support this outcome by showing how the Reynolds effect has been diminished up to 16° angle of attack. One of the main related discussions behind it may be oscillatory behavior for instantaneous C_l values for the angles of attack above 16°. Additionally, this leads to a transformation of the vortex mode from one of continuous vortex shedding to one of alternating vortex shedding (Kurtulus, 2015; 2016). Since these specific angles of attack also depend on Reynolds number, the result part will be continued and supported by skin friction coefficients, streamlines, Strouhal numbers, instantaneous behavior of aerodynamic coefficients, and wake patterns analyses.

4.3 Skin Friction Coefficients

The boundary layer on the airfoil thickens significantly in low Reynolds number flows as a result of viscous factors, therefore flow separation is possible even at small incidence angles. Therefore, the work of flow separation is very important in this kind of analysis where the Reynolds number is low.

The flow separation points experience no attachment between the flow and the airfoil surface. In other words, skin friction values become zero at these locations, making it possible to pinpoint the locations of flow separation by examining the skin friction coefficient values.

Flow separation points may vary due to different incidence angles and Reynolds numbers. Figure 4.7–Figure 4.14 provide summary of the various Reynolds values at angles of attack of 10°, 12°, 16°, and 20°. Red dots and letters are used on airfoil profiles to indicate the separation positions where the skin friction coefficient is 0.

S1: first separation point

R1: first reattachment point

S2: second separation point

R2: second reattachment point

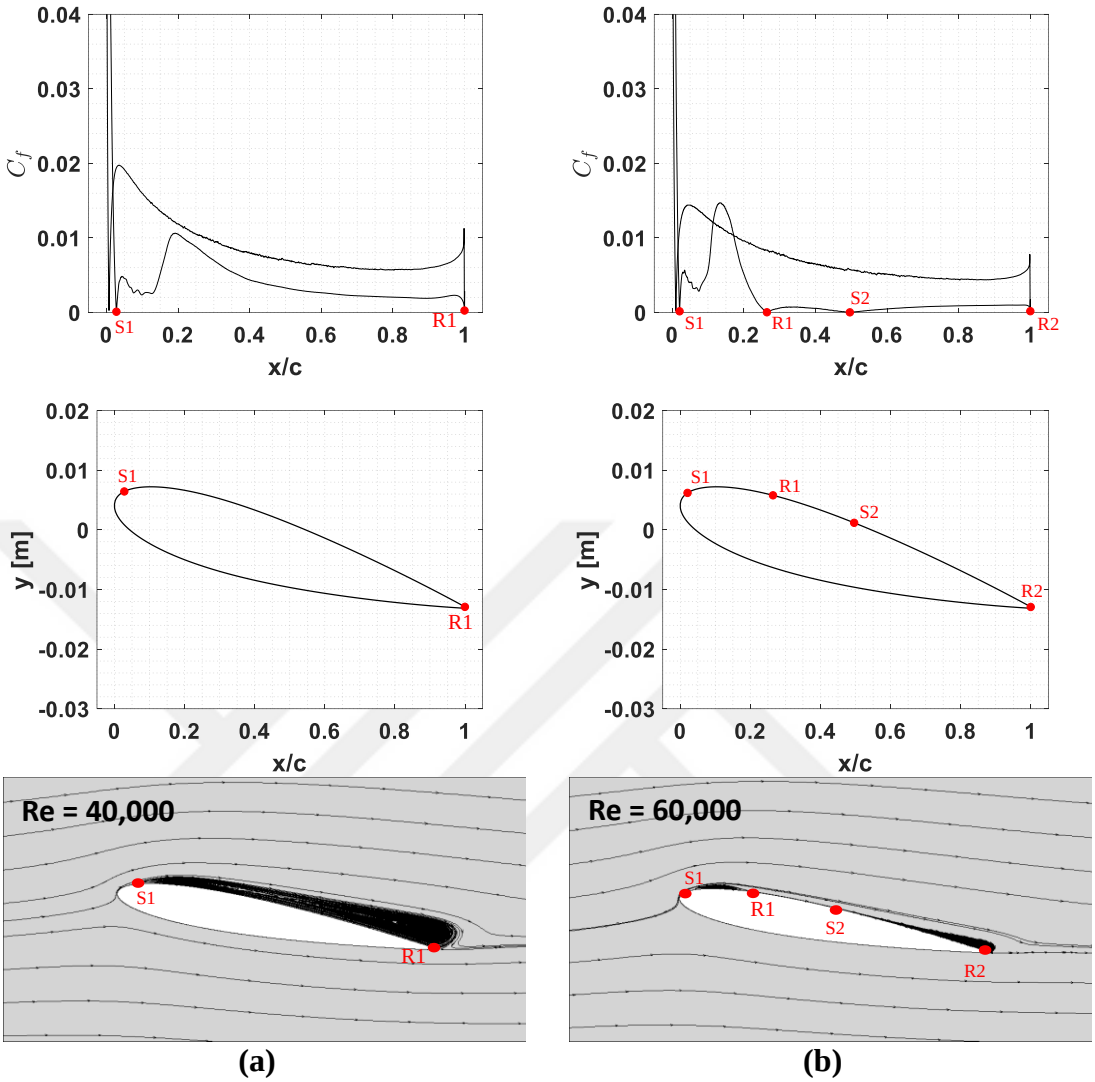

Figure 4.7. Mean skin friction coefficient and separation point on NACA 0012 at $\alpha=10^{\circ}$ for Reynolds numbers 40,000 and 60,000: a) Re=40,000 (left column), b) Re=60,000 (right column)

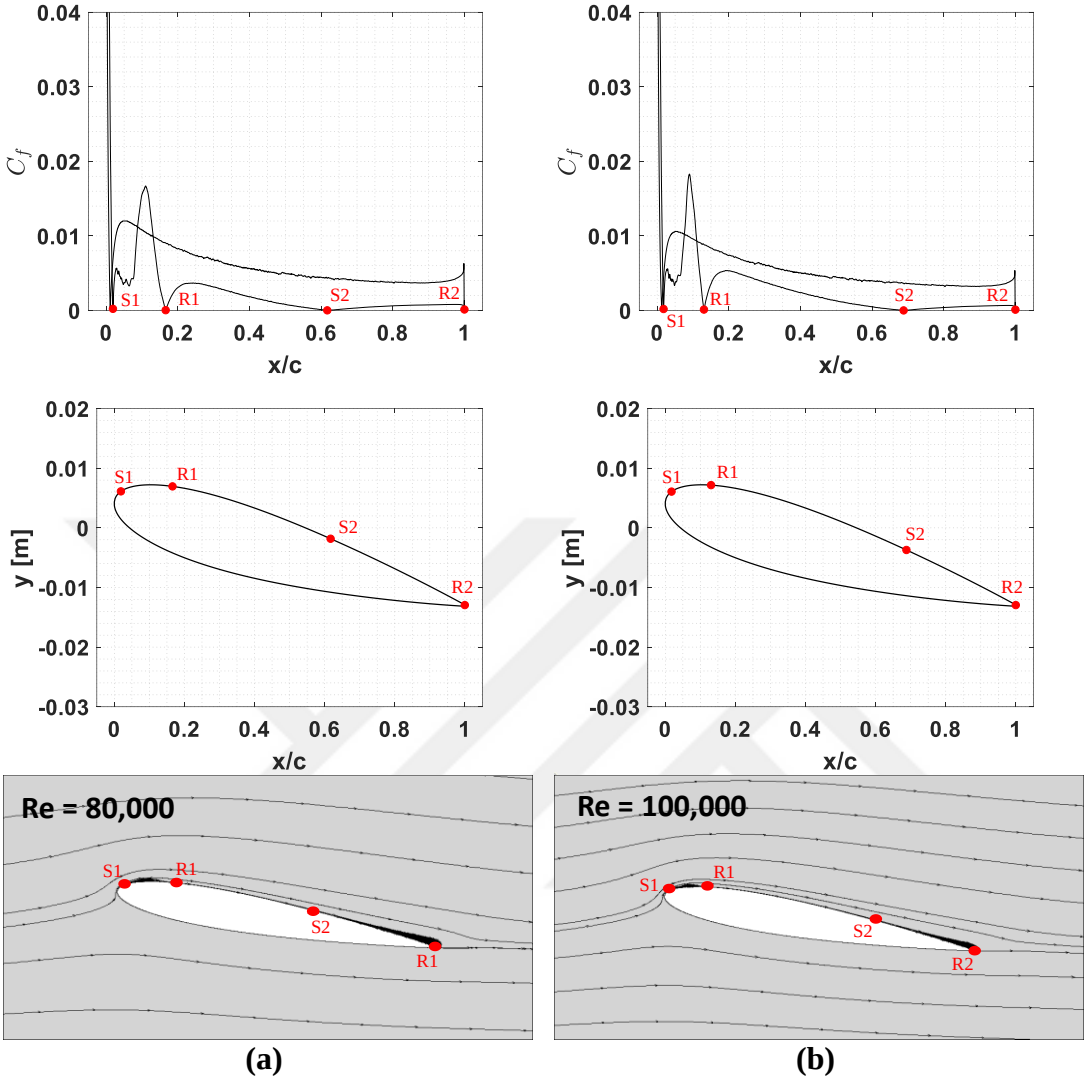

Figure 4.8. Mean skin friction coefficient and separation point on NACA 0012 at $\alpha=10^{\circ}$ for Reynolds numbers 80,000 and 100,000: a) Re=80,000 (left column), b) Re=100,000 (right column)

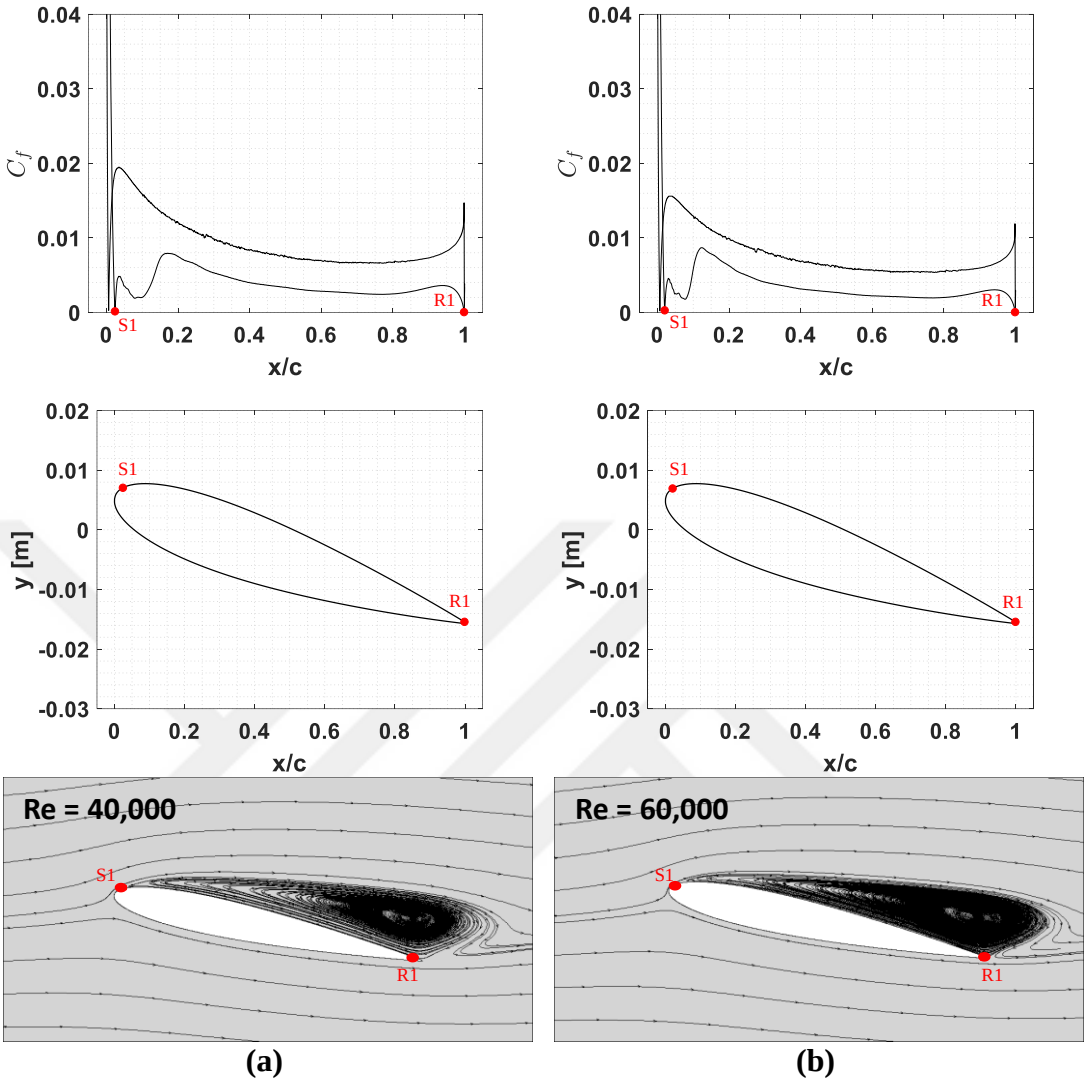

Figure 4.9. Mean skin friction coefficient and separation point on NACA 0012 at $\alpha=12^{\circ}$ for Reynolds numbers 40,000 and 60,000: a) Re=40,000 (left column), b) Re=60,000 (right column)

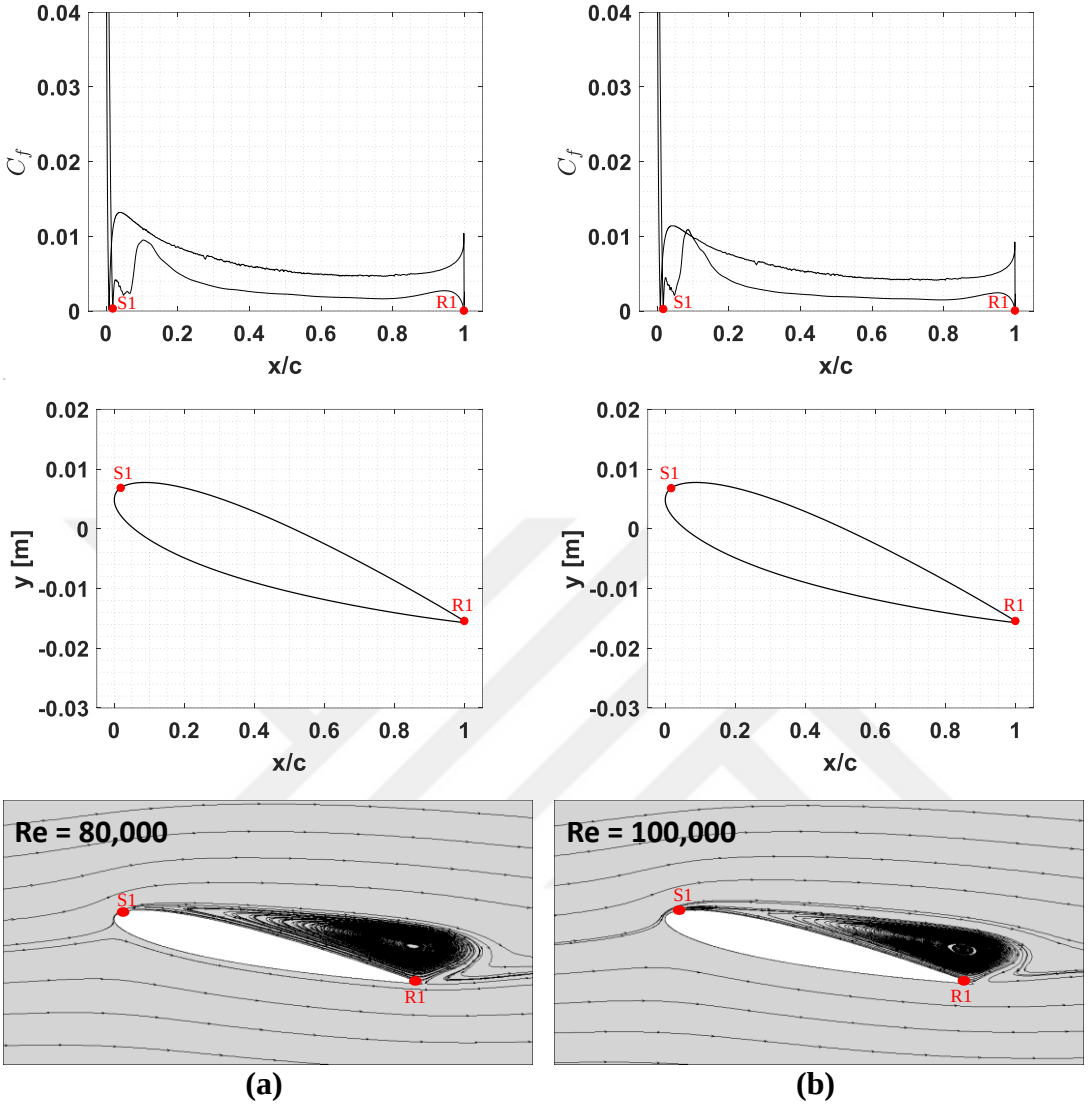

Figure 4.10. Mean skin friction coefficient and separation point on NACA 0012 at $\alpha=12^{\circ}$ for Reynolds numbers 80,000 and 100,000: a) Re=80,000 (left column), b) Re=100,000 (right column)

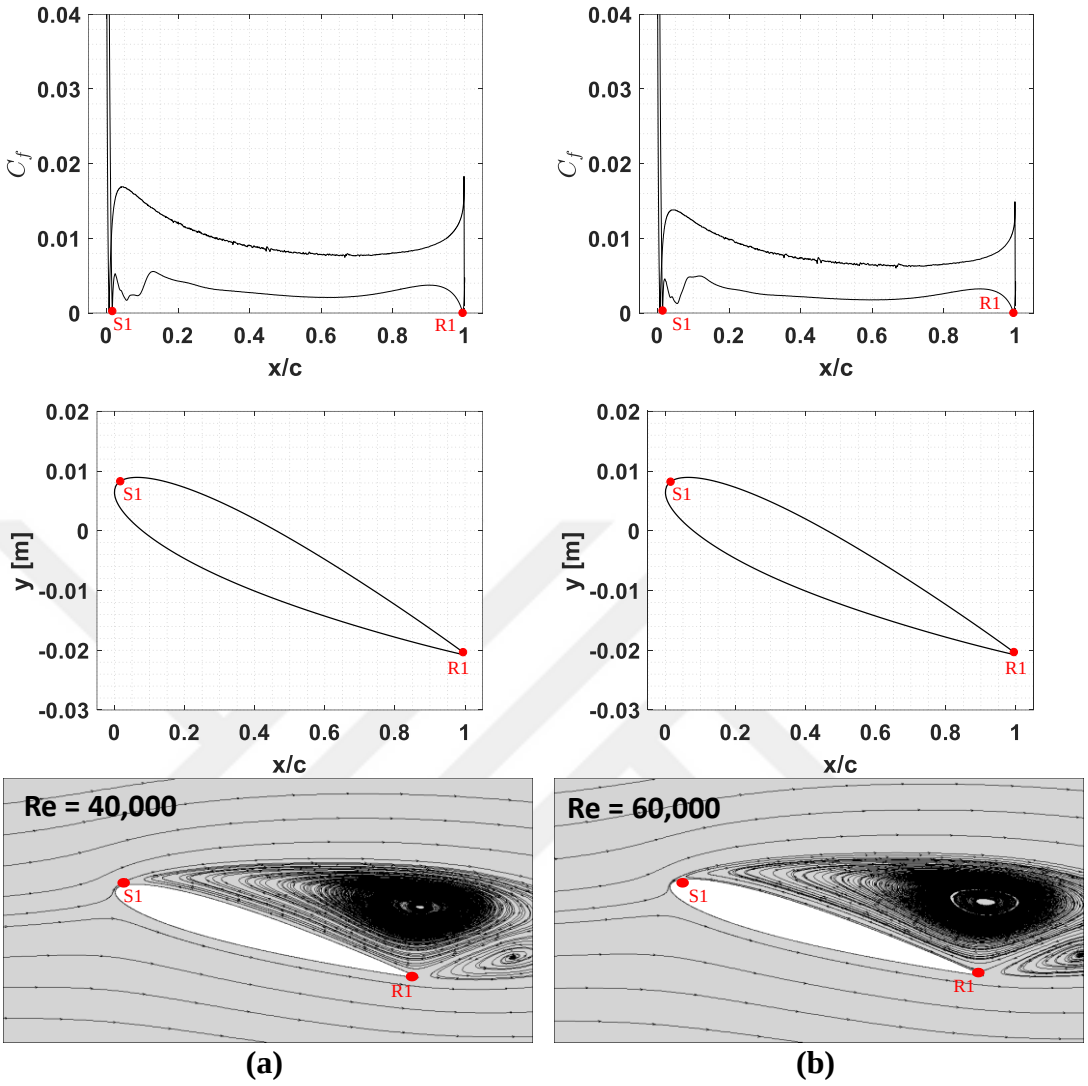

Figure 4.11. Mean skin friction coefficient and separation point on NACA 0012 at $\alpha=16^{\circ}$ for Reynolds numbers 40,000 and 60,000: a) Re=40,000 (left column), b) Re=60,000 (right column)

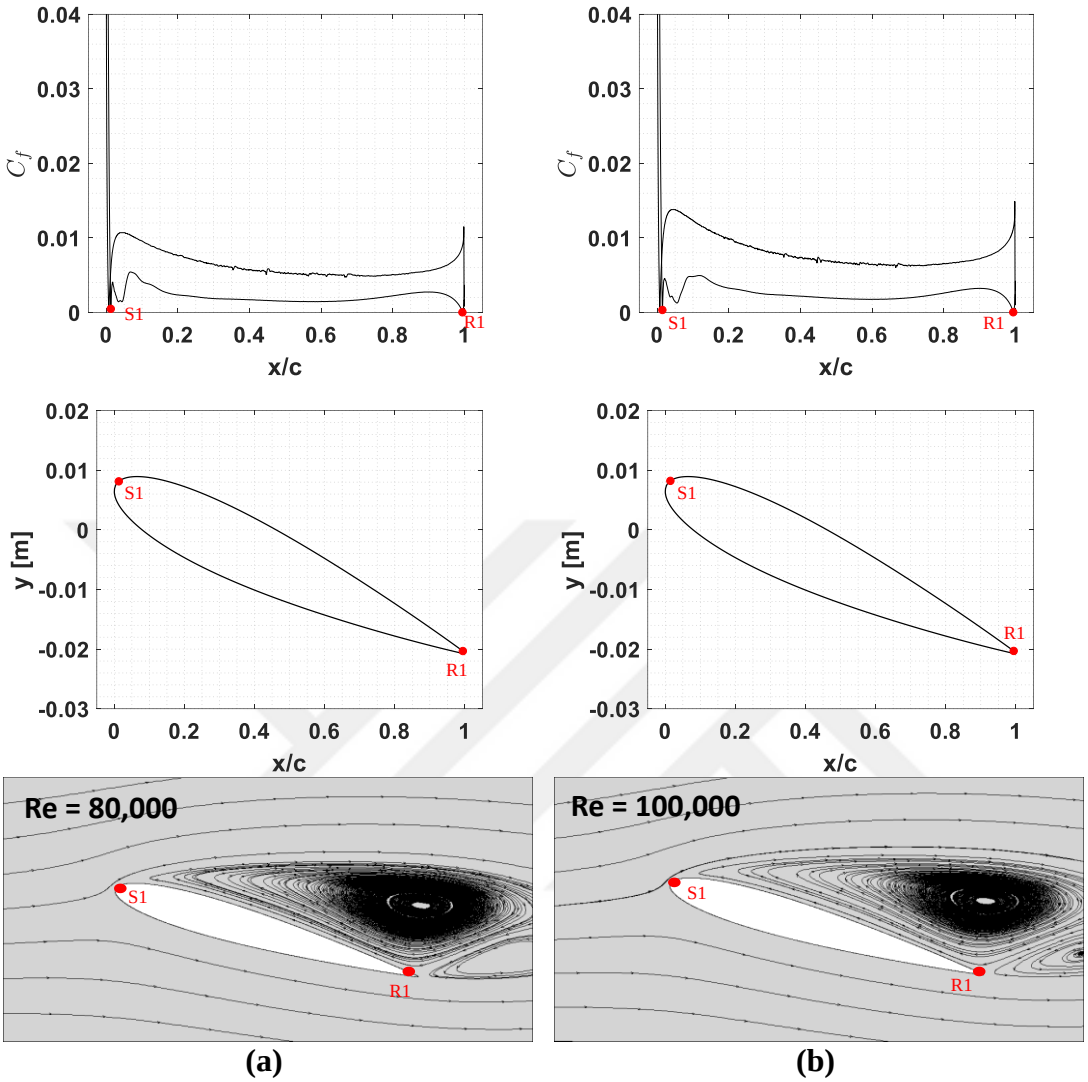

Figure 4.12. Mean skin friction coefficient and separation point on NACA 0012 at $\alpha=16^{\circ}$ for Reynolds numbers 80,000 and 100,000: a) Re=80,000 (left column), b) Re=100,000 (right column)

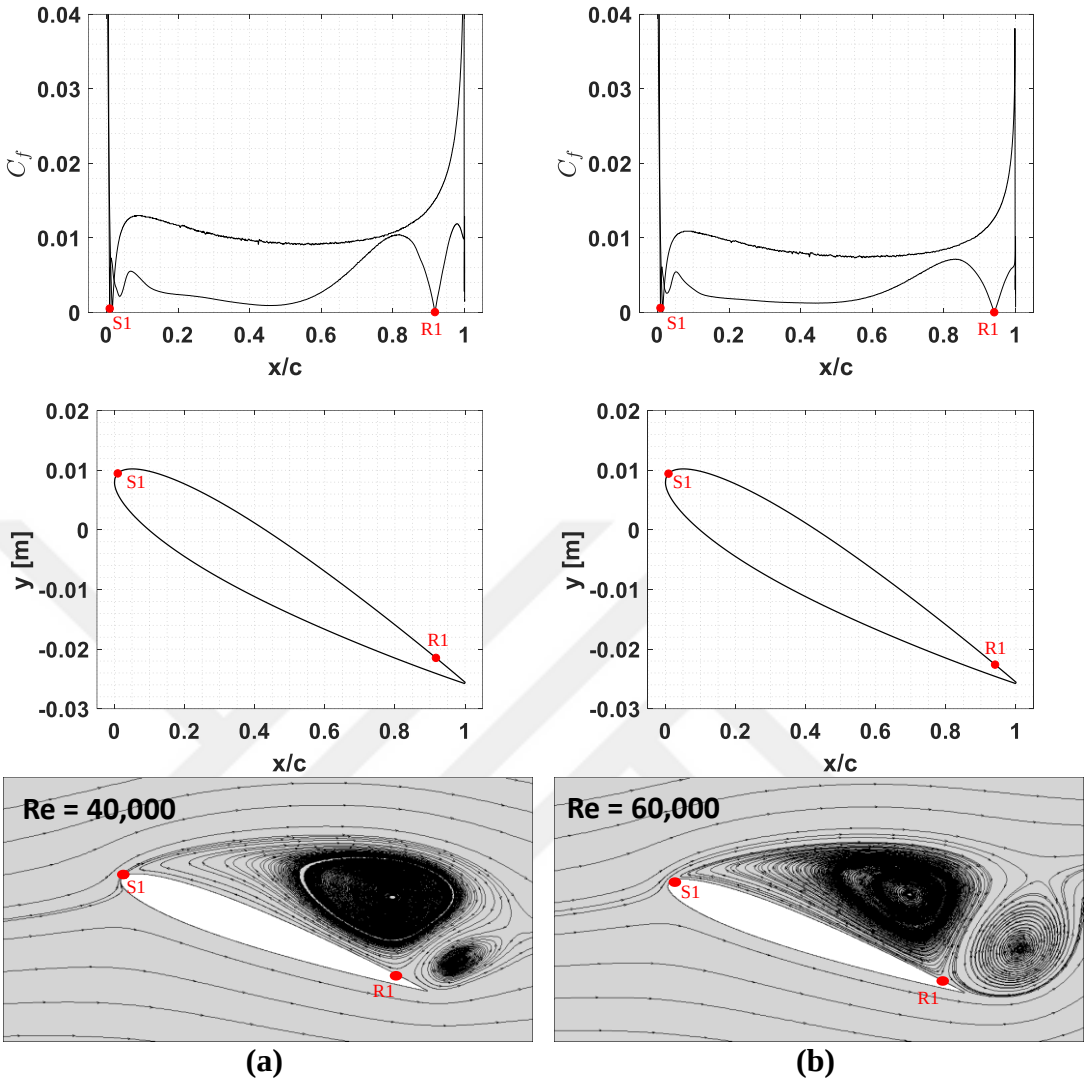

Figure 4.13. Mean skin friction coefficient and separation point on NACA 0012 at $\alpha=20^{\circ}$ for Reynolds numbers 40,000 and 60,000: a) Re=40,000 (left column), b) Re=60,000 (right column)

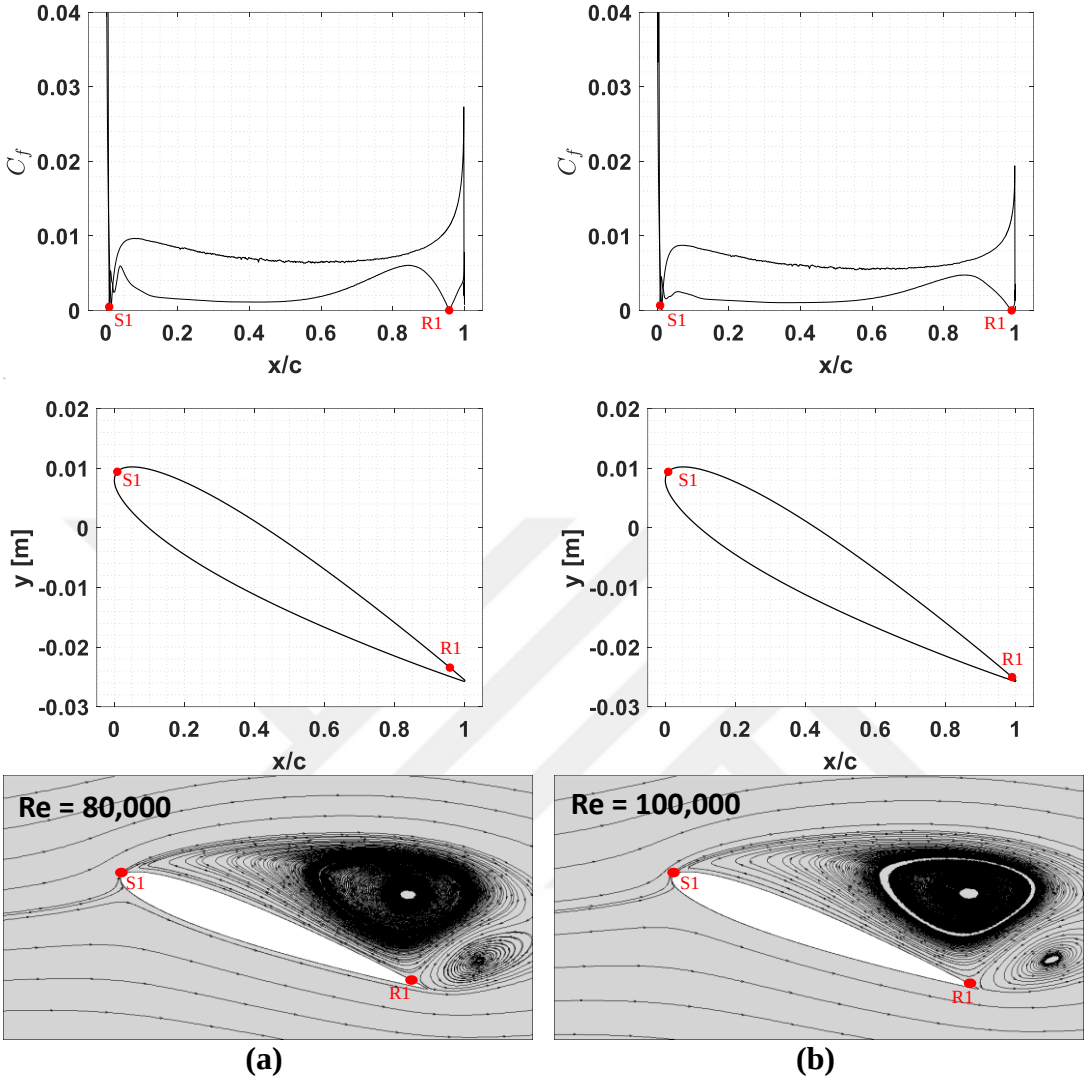

Figure 4.14. Mean skin friction coefficient and separation point on NACA 0012 at $\alpha=20^{\circ}$ for Reynolds numbers 80,000 and 100,000: a) Re=80,000 (left column), b) Re=100,000 (right column)

4.3.1 Influence of angle of attack

The angle of attack and the flow's unsteadiness are strongly associated, and as incidence angle rises, the airfoil's top surface becomes more turbulent. For instance, Re=40,000 flow stalls at 9° angle of attack, that's why it has already fully de-attached the upper surface at 10° incidence angle (Figure 4.7(a)). However, with an increasing the incidence angle, the magnitude of unsteadiness is also getting higher. So, the thickness of the recirculation of mean streamlines is getting higher. To more properly comprehend the impact of the incidence angle, specifically Re=60,000 flow may also be investigated. At 10° angle of attack, there exist two separation and reattachment points on the airfoil's top surface for Re=60,000 flow, but the flow experiences fully turbulent characteristics with increasing only 1° more angle of attack. The S1, R1, S2, and R2 points immediately went away, and only leading/trailing edge separation points are seen at 11° angle of attack.

4.3.2 Influence of Reynolds number

Re=40,000 flow has fully de-attached streamline topology at 10° angle of attack, but the other flows have two different separation regions on their upper surfaces. It results from that lower Reynolds number flows tend to separate than relatively higher ones. Additionally, as the Reynolds number rises, R1 and S2 points move to the leading and trailing edges of the airfoil, respectively. For instance, the S2 point sits between 0.4–0.6 x/c for Re=60,000 at 10° angle of attack, around 0.6 x/c for Re=80,000, and finally 0.6-0.8 x/c for Re=100,000.

4.4 Streamlines

Streamlines are provided for a range of incidence angles to help one understand how low Reynolds number flows are prone to experience the separation bubbles even at extremely low incidence angles. The “arrow” in the figures shows the recirculation zones that are attached to the top surface of the airfoil. The “ * ” sign represents the stall angle for the corresponding Reynolds number. The first angle that is represented after the stall angle showed with several “arrow” lines. This indicates that deattached flow occurs over the airfoil's top surface at the lowest angle.

4.4.1 Influence of angle of attack

The mean velocity streamline figures show that much of the information about the flow itself. It is evident that for each Reynolds number, a separation bubble exists in the trailing edge of the airfoil even at 0° incidence angle. By extending the incidence angle, this zone reaches the leading edge of the airfoil. This phenomena may be one of the key causes for the absence of a completely linear lift-to-incidence angle trend for low Reynolds number flow. Moreover, there are two unique recirculation zones that are present right before the stall angle: one is the separation bubble that extends to the leading edge of the airfoil, and the other is the traditional trailing edge separation bubble.

Further analysis revealed that, only 1° above the stall angle, the flow is totally deattached. This outcome is to be expected because the system is subjected to additional instability due to the higher incidence angle. Lastly, it may be said that as the magnitude of the unsteadiness rises, a higher incidence angle helps the recirculation zones grow.

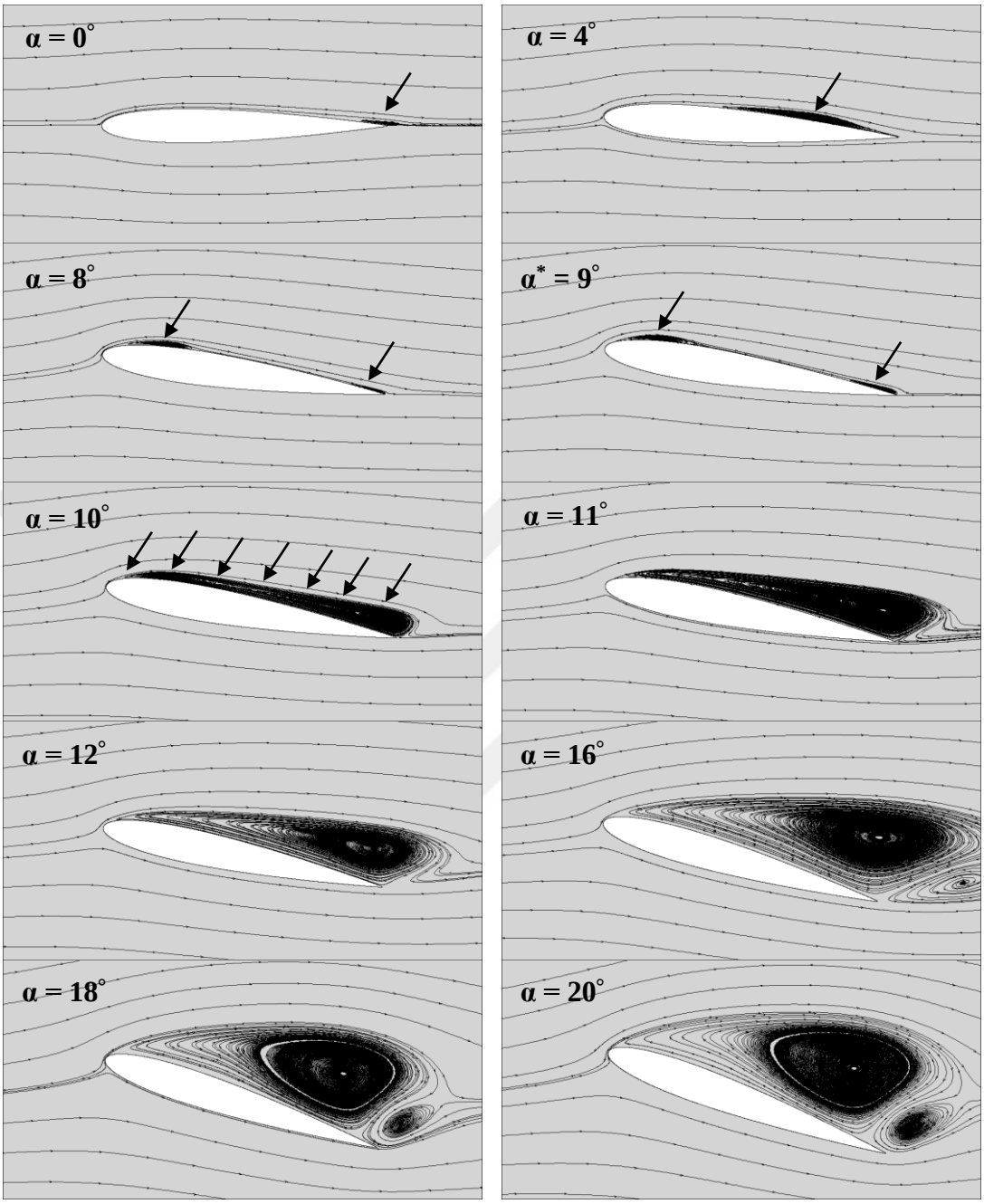

Figure 4.15. Mean velocity streamlines at different angles of attack for Re=40,000

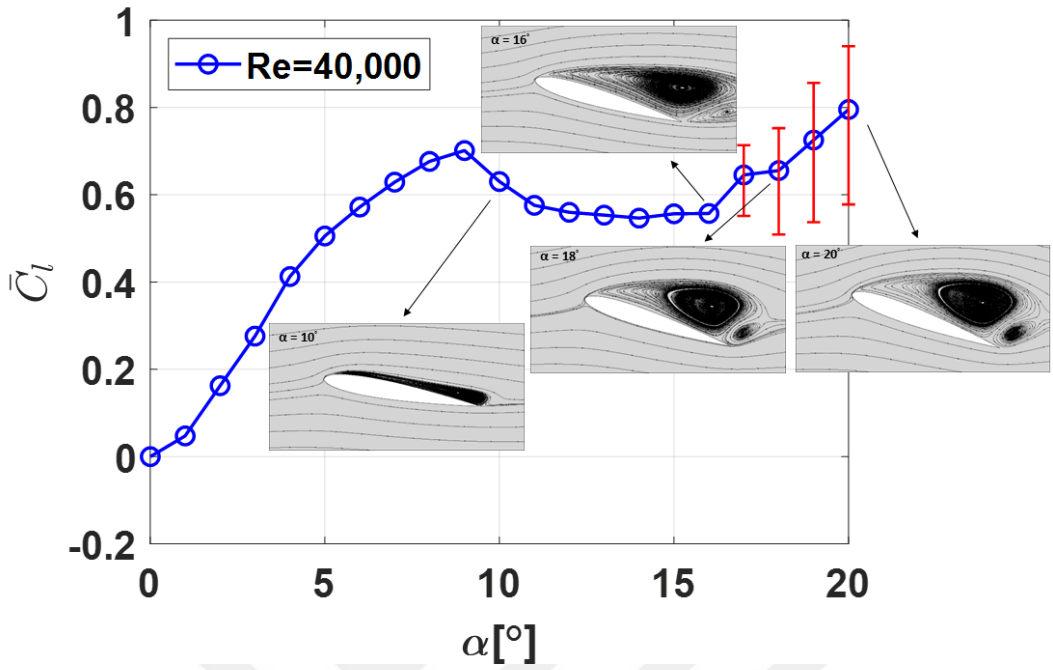

Figure 4.16. Mean lift coefficient vs. angle of attack for Re=40,000

The mean lift coefficient vs. angle of attack is represented with four different incidence angles streamlines. The red error bar indicates how the instantaneous lift coefficient oscillates around the mean value. The maximum and minimum values are the upper and lower boundary of the error bar. As unsteady behavior dominates with rising the incidence angle, the error bounds are also expanding. The first oscillation angle for Re=40,000 is 17° angle of attack. Before this value, the streamlines show that there is no second counter-rotating vortex on the top surface of the airfoil (α=16°). With increasing the angle of attack, the second counter-rotating vortex propagates toward to leading edge, and this may result in higher amplitude oscillations as seen in red error bars. Lastly, since the stall angle is 9°, the α=10° streamlines show that the upper surface is totally deattached and the lift decreases.

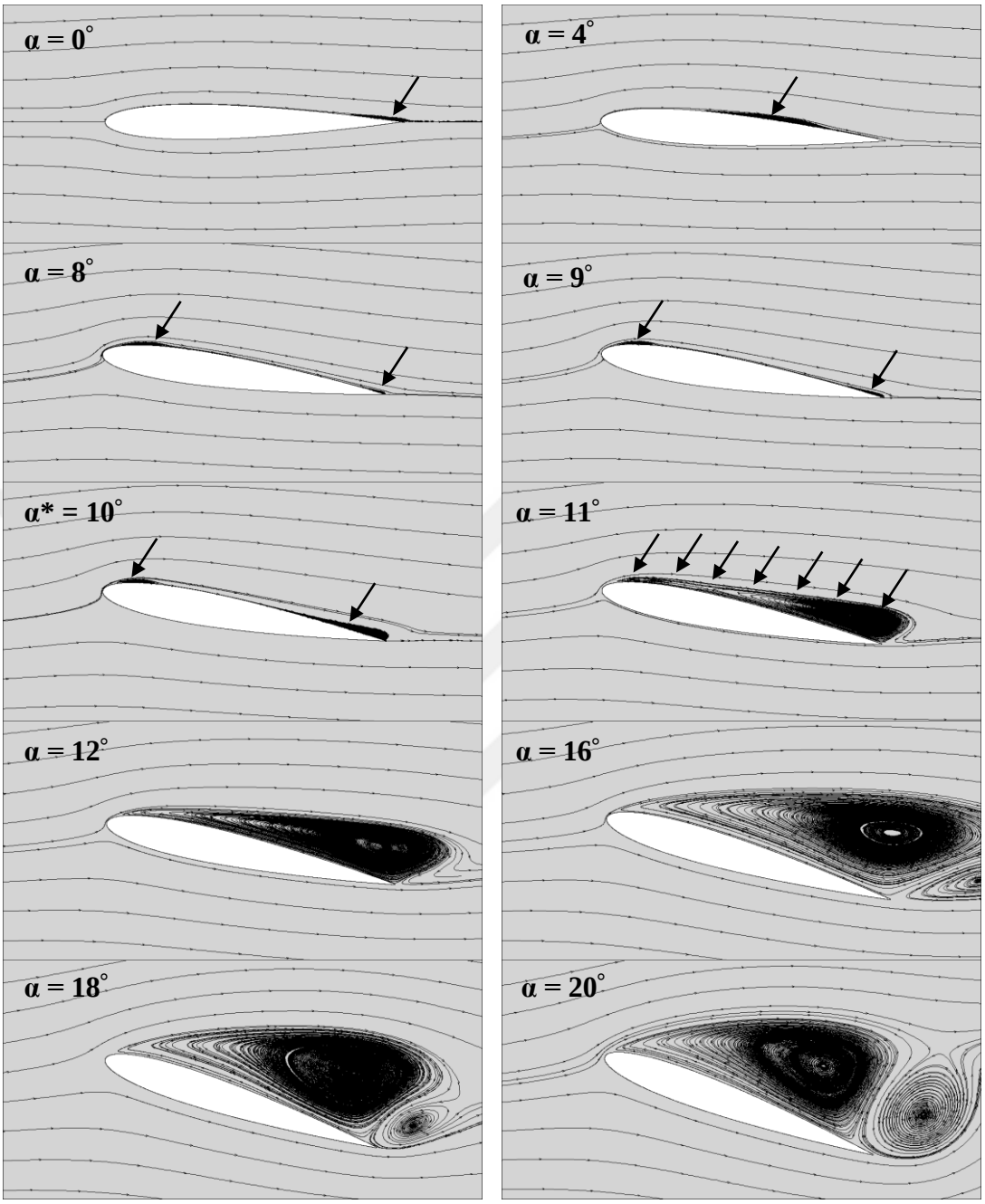

Figure 4.17. Mean velocity streamlines at different angles of attack for Re=60,000

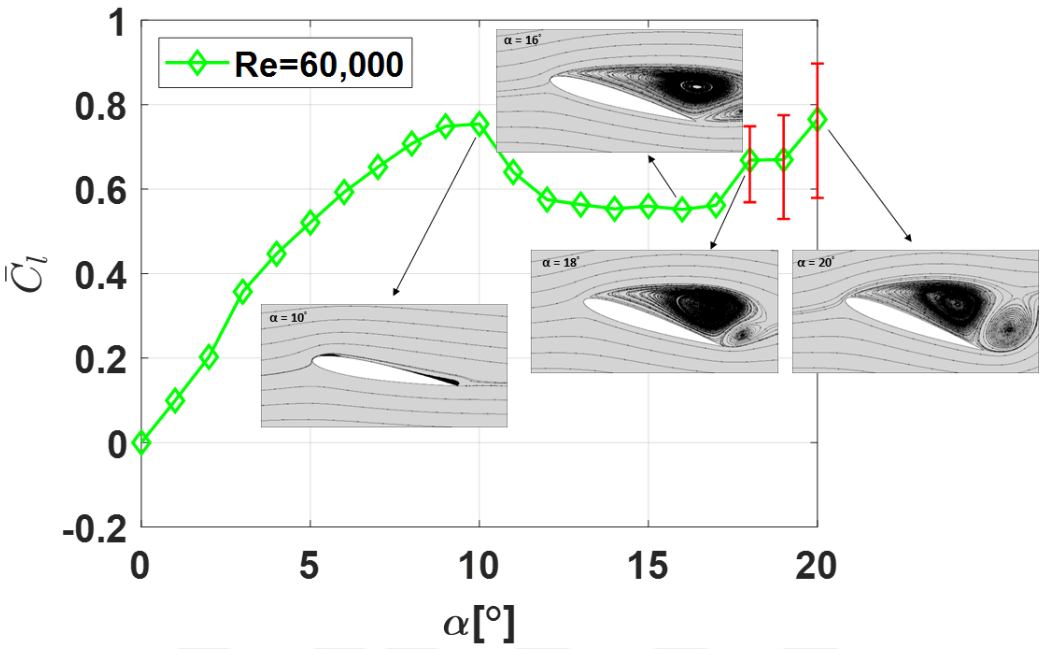

Figure 4.18. Mean lift coefficient vs. angle of attack for Re=60,000

Similar comments as in Re=40,000 flow are also applicable for Re=60,000 in terms of the relation between oscillatory lift behavior (red error bars) and the existence of a second counter-rotating vortex on the top surface of the airfoil. However, the threshold angle of attack value is changed. The oscillatory motion in the aerodynamic coefficient exists at 18° angle of attack which is 1° more than the previous case. Lastly, since the stall angle is 10°, the streamlines do not show fully deattached flow. The separation bubble and conventional trailing edge separation bubble look very big in dimension, but there still exists attached flow on the middle chord of the top surface of the airfoil.

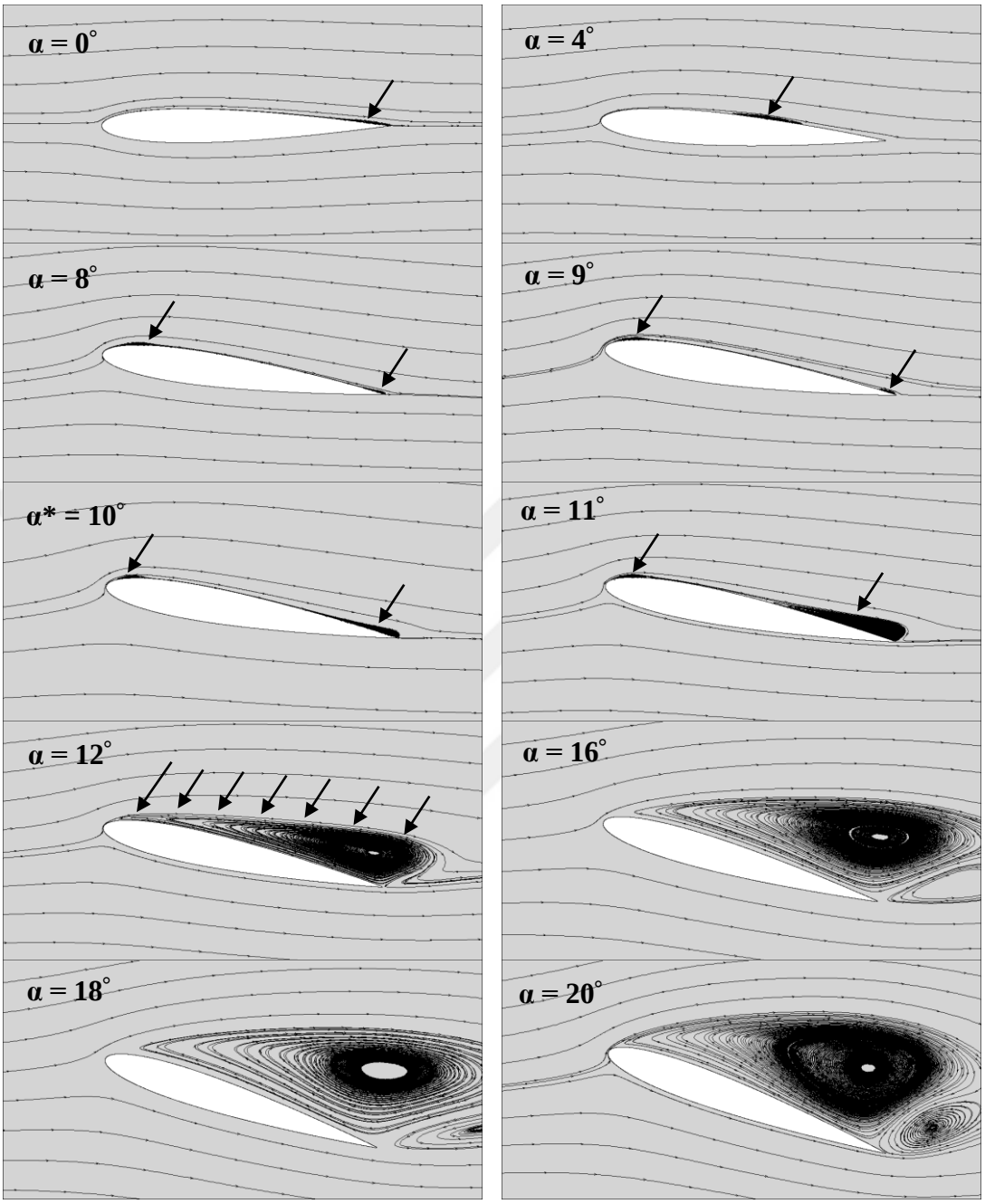

Figure 4.19. Mean velocity streamlines at different angles of attack for Re=80,000

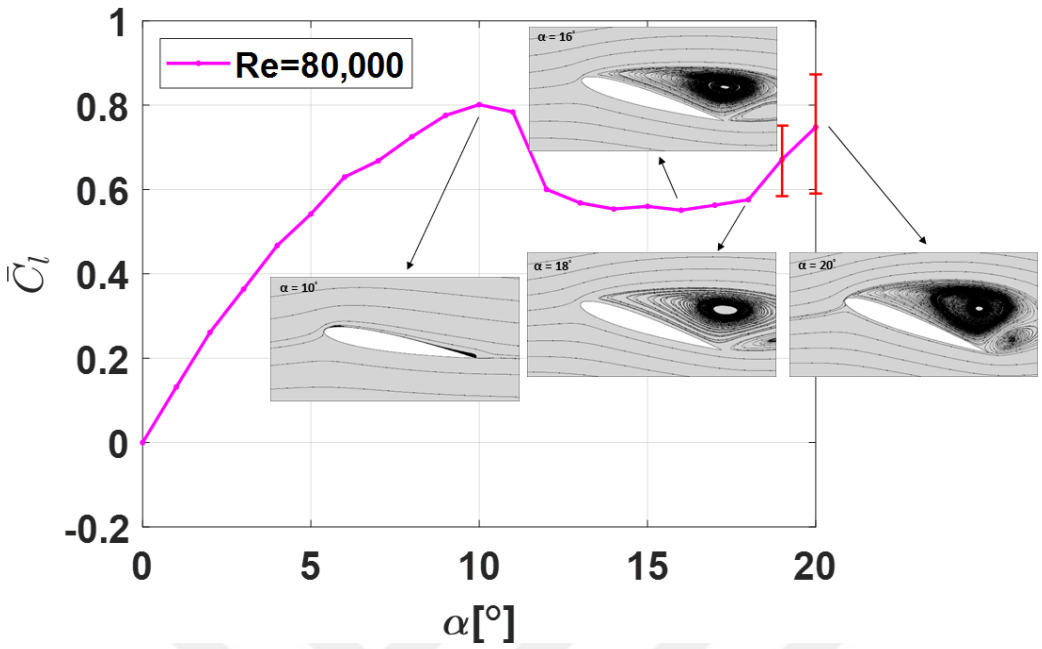

Figure 4.20. Mean lift coefficient vs. angle of attack for Re=80,000

By increasing the Reynolds number to 80,000, the mentioned results seem more obvious. Firstly, the angle where oscillatory motion starts is now 18° which is 1° higher than Re=60,000. And, the amplitude of oscillation decreases at the same incidence angles (i.e. 19° and 20°) for higher Reynolds numbers. The 18° does not produce any oscillatory motion, so the second counter-rotating vortex is again not on the top surface of the airfoil. Moreover, the stall angle is again 10° for Re=80,000, but the separation bubble and conventional trailing edge separation bubble decreases in size.

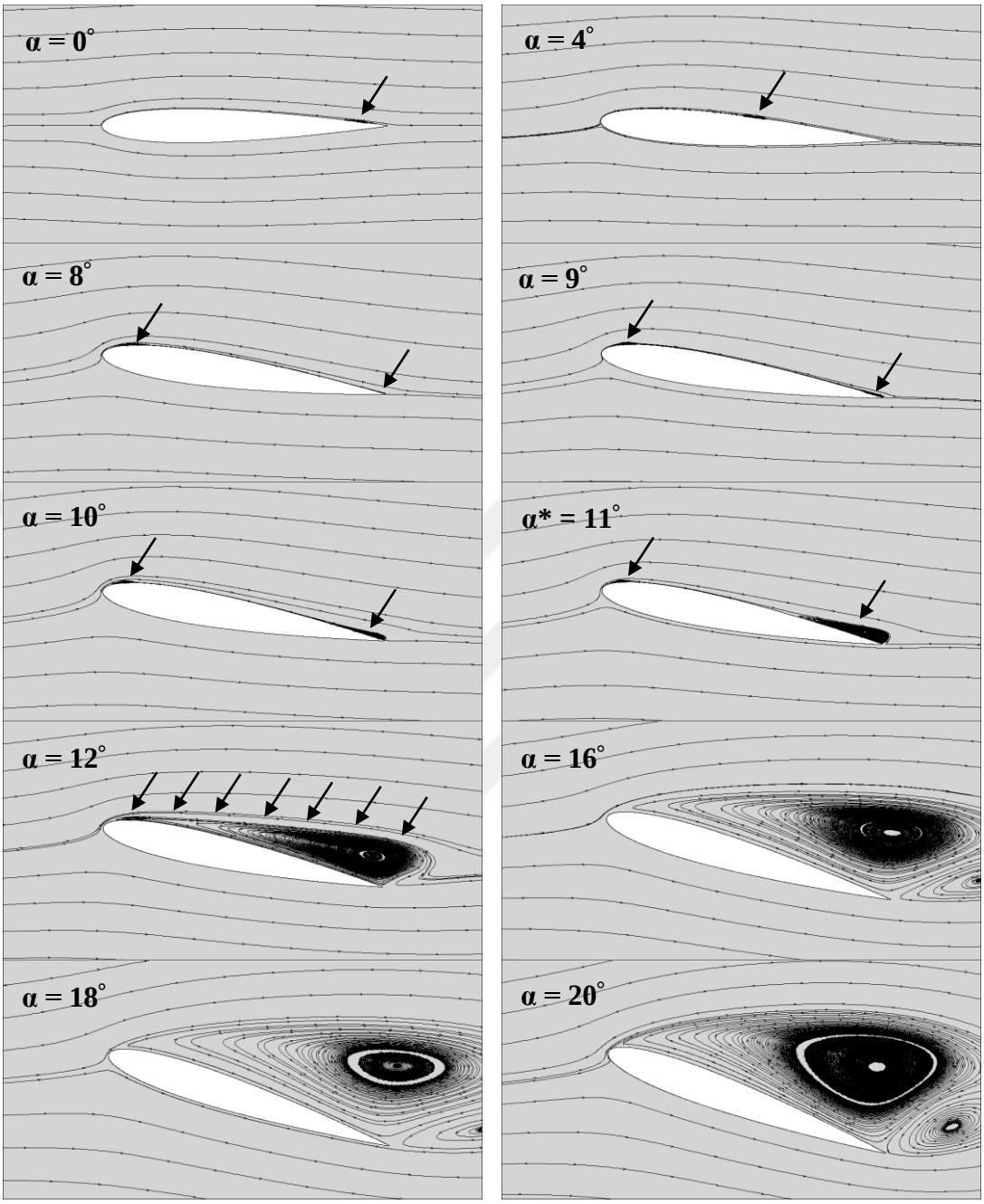

Figure 4.21. Mean velocity streamlines at different angles of attack for Re=100,000

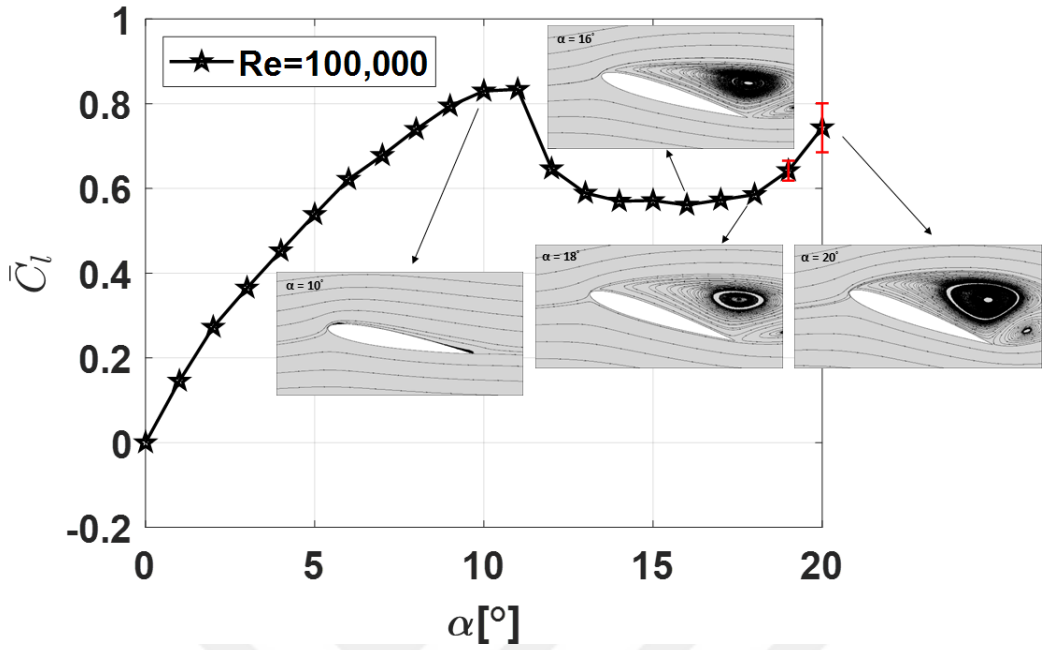

Figure 4.22. Mean lift coefficient vs. angle of attack for Re=100,000

The same comments in Re=80,000 are directly applicable for Re=100,000. By rising the Reynolds number the angle where the oscillatory motion starts does not change, however, the magnitude of quasi-periodic motion is decreasing. For instance, the 19° incidence angle is seen as having almost non-oscillatory motion by looking at the red error bounds which were not applicable for Re=80,000. Moreover, as observed for Re=80,000, the bubbles' sizes are still decreasing for Re=100,000 at 10° incidence angle. This results in getting a higher lift coefficient for higher Reynolds numbers thanks to the clear pressure distribution over the airfoil surface. Lastly, the stall angle is rising to 11° for Re=100,000.

4.4.2 Influence of Reynolds number

Figure 4.23–Figure 4.30 indicates the streamlines at a fixed incidence angle for each Reynolds number. Because viscous forces rather than substantially greater Reynolds number flows are more prevalent in this situation, the separation bubble is largest for the lowest Reynolds number (e.g. Figure 4.24). This is also valid for the pre-stall region where two distinct recirculation zones are observed (Figure 4.25 and Figure 4.26). Additionally, the Reynolds number effect is more visible at 10° and 11° angles of attack. The stall angle is 9° for Re=40,000, that's why the streamlines show unattached flow at 10°, meanwhile, rest of the Reynolds numbers still have attached zones, and the size of attached regions over the airfoil surface increases with increasing Reynolds number (Figure 4.27). At the 11° incidence angle, the Re=60,000 and Re=80,000 flows exhibit the same result, and they start to have unattached flows. However, the streamlines showed a slight difference between them, and Re=80,000 flow shows more stable characteristics than Re=60,000. Figure 4.1(a) shows that Re=80,000 has more gentle post-stall characteristics than Re=60,000 at between 10°–11° angles of attack so this small difference is consistent with mean aerodynamic coefficient behavior.

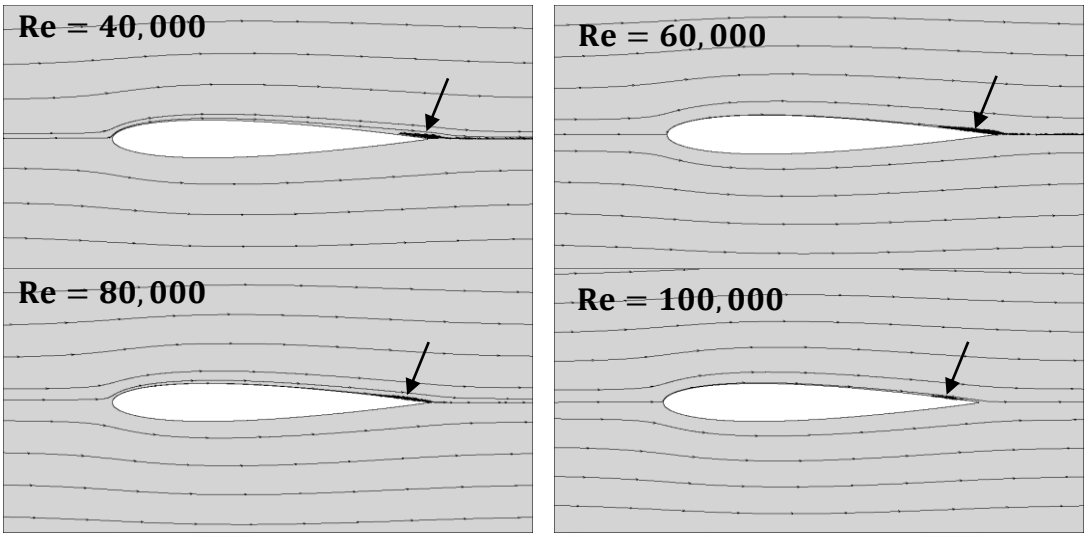

Figure 4.23. Mean velocity streamlines at α=0° for different Reynolds numbers

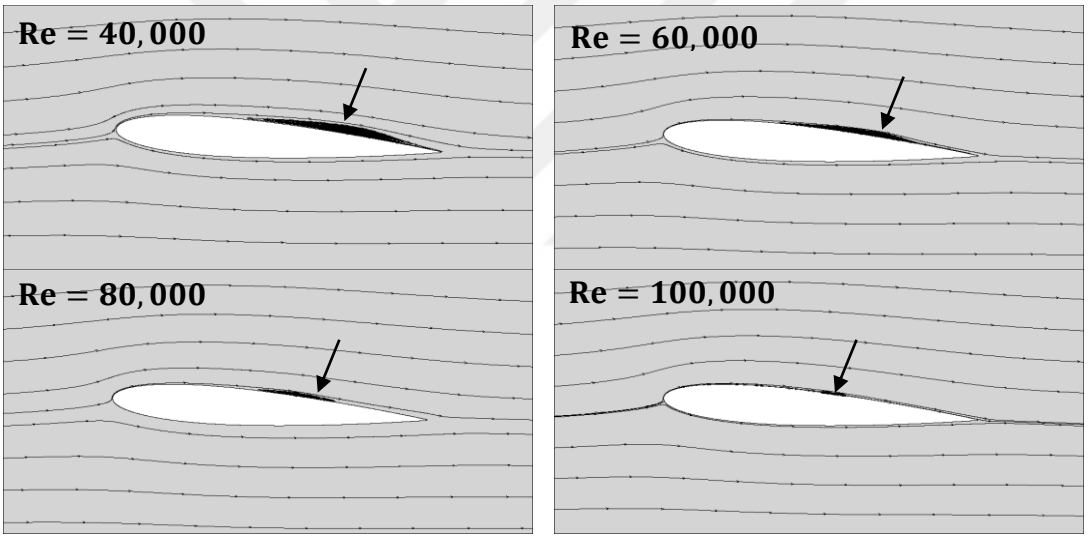

Figure 4.24. Mean velocity streamlines at α=4° for different Reynolds numbers

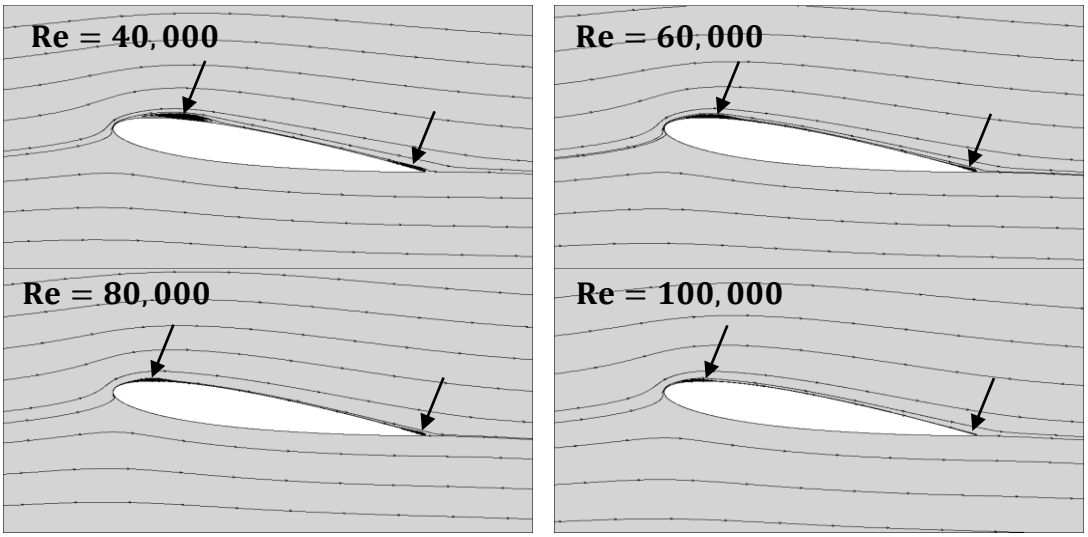

Figure 4.25. Mean velocity streamlines at α= 8° for different Reynolds numbers

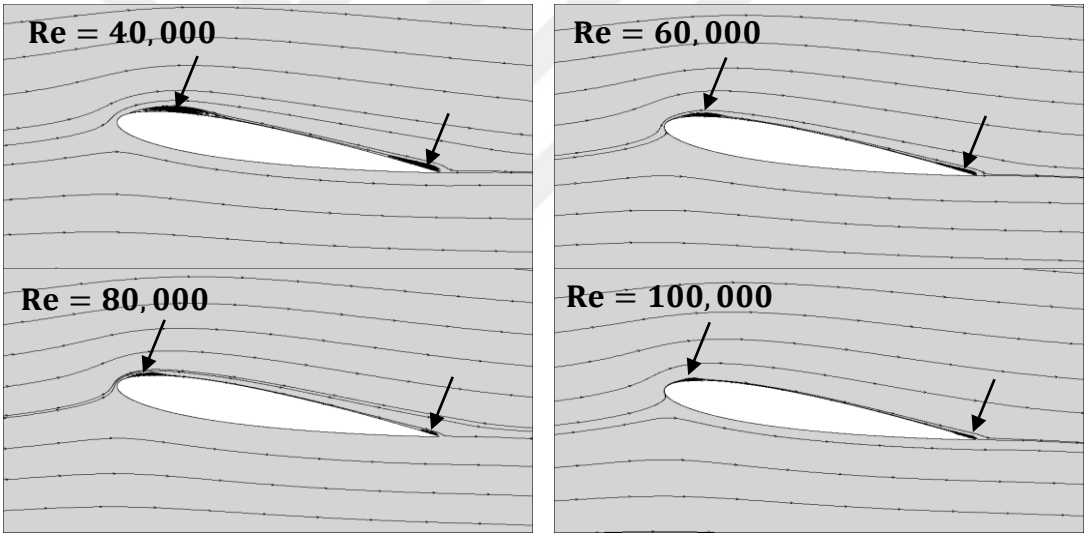

Figure 4.26. Mean velocity streamlines at α=9° for different Reynolds numbers

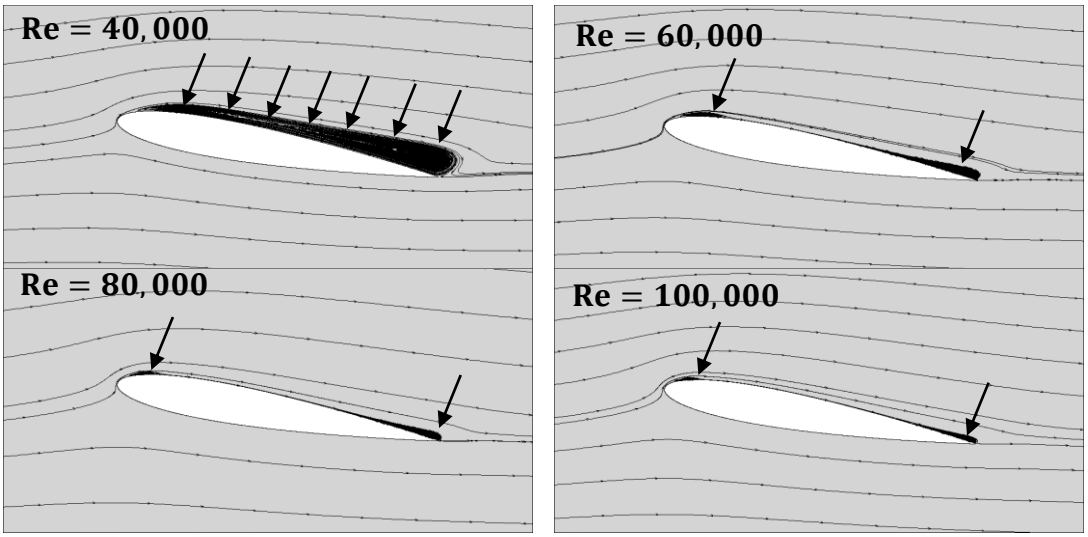

Figure 4.27. Mean velocity streamlines at α=10° for different Reynolds numbers

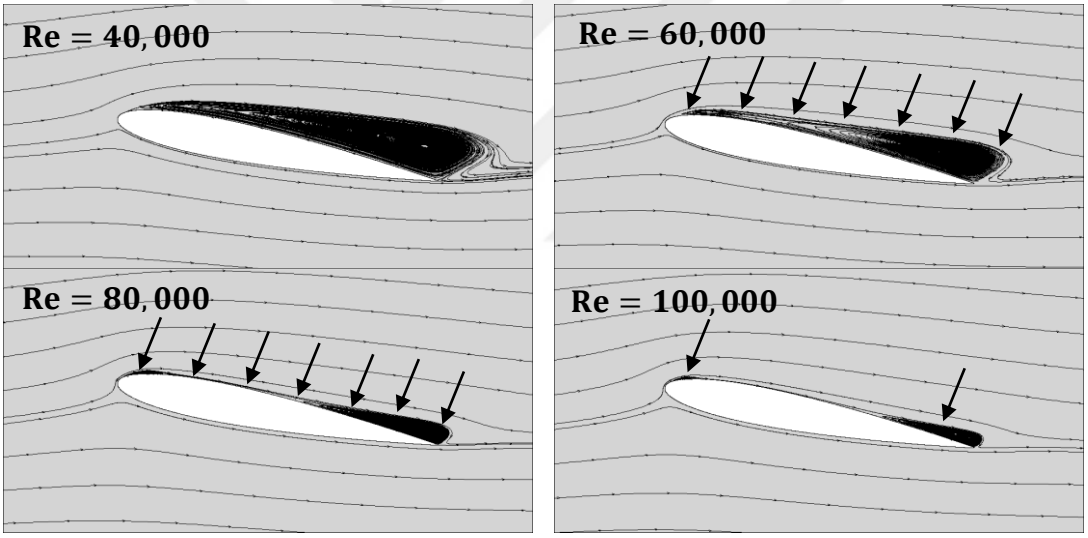

Figure 4.28. Mean velocity streamlines at α=11° for different Reynolds numbers

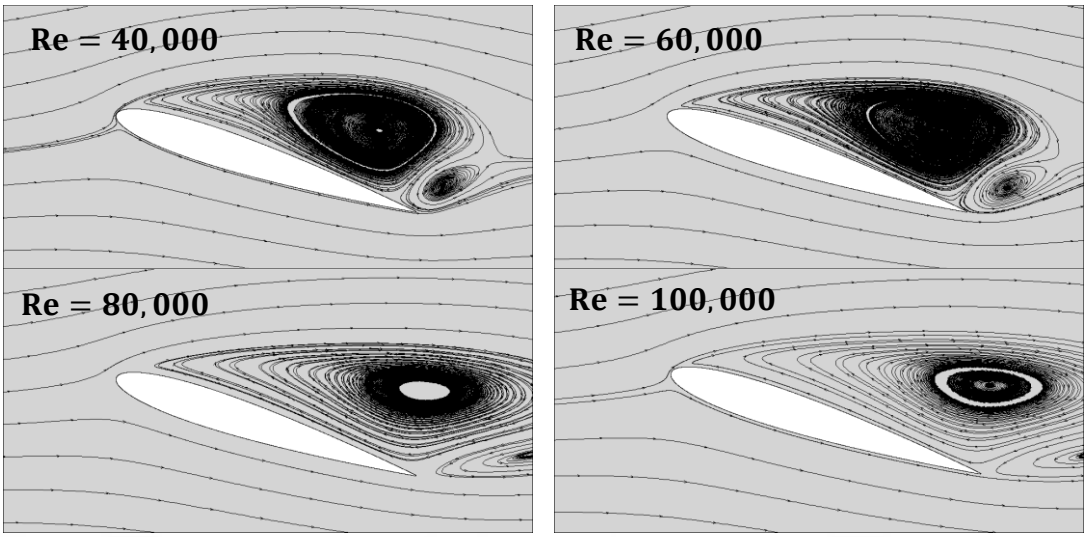

Figure 4.29. Mean velocity streamlines at α=18° for different Reynolds numbers

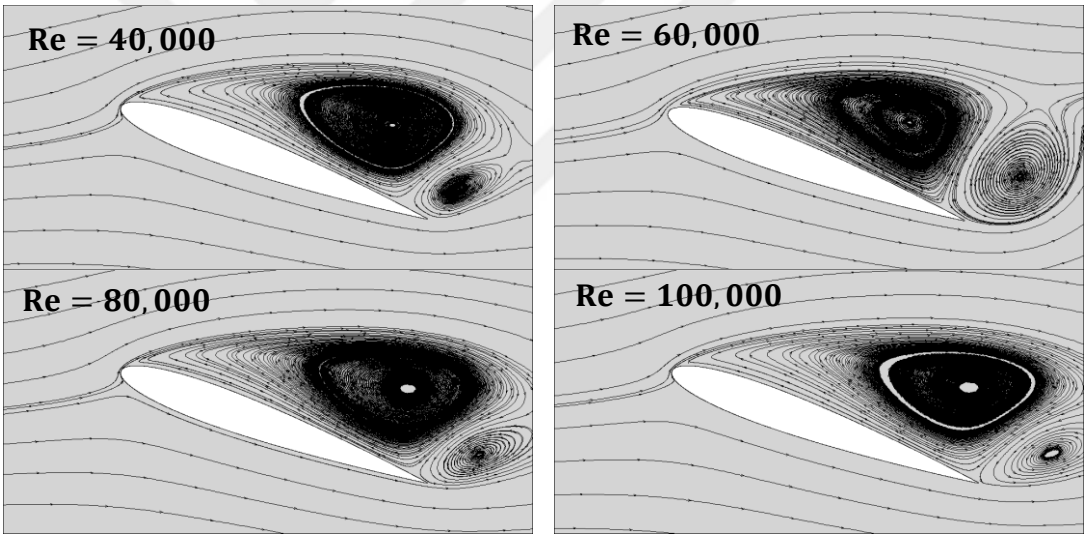

Figure 4.30. Mean velocity streamlines at α=20° for different Reynolds numbers

4.5 Strouhal Number Analysis

Strouhal number (St) is a non-dimensional variable, similar to Reynolds number, that aids in determining whether or not the flow is creating a vortex. Taylor et al. (2003) worked on the 42 species of birds, insects, and bats in cruise flight in terms of the flapping frequencies and amplitudes, then came to the conclusion that their group's Strouhal numbers were typically between 0.2 and 0.4. The Reynolds number of their flight regime can be seen lower bounds of this particular work, and the results of relatively lower Reynolds number solutions of this study should be similar to Taylor et al. (2003)'s results, and because of the higher Reynolds number solutions, it is possible to comprehend the Reynolds number effect in this section.

Strouhal number (St):

$$St = fA/U \tag{17}$$

f = vortex shedding frequency in Hertz

A = characteristic length

U = flight speed

Characteristic length definition may be varied for different problems. For the airfoil case, it is taken as the length of chord.

There is a correlation between the shedding vortex frequency, the Reynolds number, and the Strouhal number: (Chang et al., 2022)

$$Re \propto \frac{St}{f} \tag{18}$$

Non-dimensional parameters in aerodynamics facilitate the scientists' work to compare or categorize materials/problems. For example, Taylor et al. (2003) showed that the flight performances of different animals can be compared by investigating their Strouhal numbers. Moreover, thanks to Strouhal number has no dimension; the size, type, weight, etc. of the animals are not even important when compare them with their Strouhal numbers.

Physically, the Strouhal number is a measurement of the proportion of inertial forces resulting from local acceleration or unsteady flow to those resulting from changes in flow velocity between different points. For low Strouhal numbers (St << 0.2), the fluid quickly sweeps past the body, and the flow is dominated by convective acceleration. At high Strouhal numbers (St >> 0.3), the fluid cannot keep up with the oscillations of the body, and the flow is dominated by local acceleration. At intermediate Strouhal numbers (0.2 < St < 0.3), the shedding of vortices downstream of a bluff body occurs, creating a repeating pattern of eddies that can be seen as a series of alternating vortices.

Mathematically, any continuously monitored time series curve can be described as an endless superposition of sine waves with various frequencies. Alternatively, the NACA 0012 airfoil with numerous incidence angles and Reynolds numbers is investigated by using Fast Fourier Transform (FFT) algorithm based on the lift coefficients for this particular work. The frequency properties of vortex shedding are evident in the frequency domain, making it easier to understand the fluctuation law of the vortex (Chang et al., 2022). Moreover, Strouhal number analyses are also constructed between non–dimensional time, $t^*=tU_\infty/c$=[1172 1465] to avoid the initial errors of the computations. To see better, the maximum frequencies of the lift coefficient amplitude spectrums are labeled in the figures.

Reynolds number is taken between 40,000–100,000 with 20,000 increments. The angles of attack are taken above the 16° angle of attack because Strouhal number analysis is related to vorticity, and none of the solutions give any oscillatory motion in aerodynamic coefficients, or Mode 2 wake pattern below than 17° angle of attack. The following chapters will go into greater detail about these topics.

4.5.1 Influence of angle of attack

For very low incidence angles, the Strouhal number analysis is not necessary, because the flow is not generating a vortex. That's why it is crucial to understand which angle of attack regime is valid for discussion. The first positive Strouhal number exists at 17° incidence angle for Re=40,000, and the peak value of Strouhal number is decreasing with increasing the incidence angle. This behavior is similar for the all Reynolds number flows and literature data (Chang et al., 2022).

To comprehend how the maximum Strouhal number is affected by incidence angle as a percentage, it is better to use Re=40,000 because there exist four Strouhal numbers for it. For Re=40,000, the maximum Strouhal numbers are 0.226, 0.217, 0.208, and 0.199 at 17°, 18°, 19°, and 20° angles of attack, respectively. So, the corresponding decrement percentages are 3.98%, 4.15%, and 4.33%. It implies that when the incidence angle increases, the Strouhal number decrement trend also rises. Moreover, the amplitude of the lift coefficient increases with a higher incidence angle, because unsteadiness is increasing with the incidence angle.

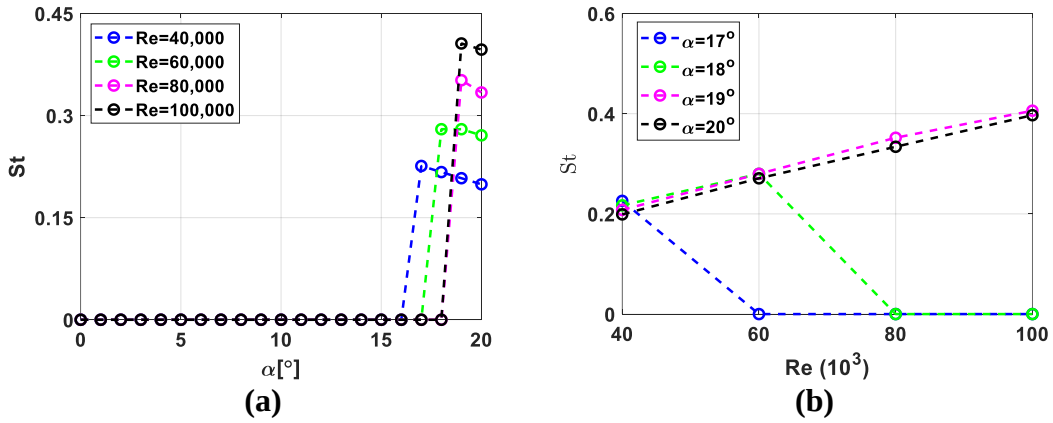

Figure 4.31. a) Strouhal number vs. α comparison for different Reynolds numbers, b) Strouhal number vs. Re comparison for different angles of attack

4.5.2 Influence of Reynolds number

Figure 4.31(b) showed that the Reynolds number and the Strouhal number have a roughly linear connection at α=19° and α=20°. The following formulas are derived by linear curve fitting such that:

$$At\ \alpha=19^{\circ}: St = 3.33x10^{-6}Re + 0.0784 \quad ; \quad 40{,}000 < Re < 100{,}000 \qquad (19)$$

$$At\ \alpha=20^{\circ}: St = 3.285x10^{-6}Re + 0.0703 \quad ; \quad 40{,}000 < Re < 100{,}000 \qquad (20)$$

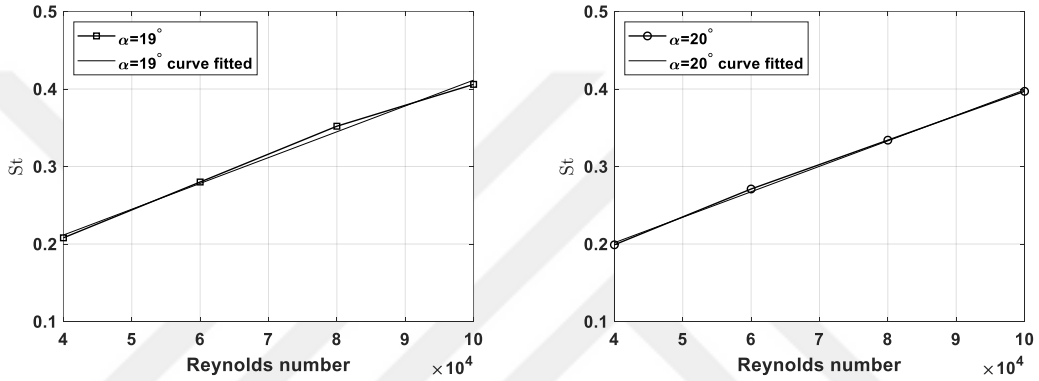

(a) **(b)**

Figure 4.32. Strouhal number vs. Reynolds number relation with curve fitted comparison: a) α=19°, b) α=20°

Increasing of Reynolds number results in a higher Strouhal number. This pattern resembles the data from the available literature of Yarusevych et al. (2009) and Jiang and Cheng (2017). Moreover, the higher Reynolds number flow experiences a non-zero Strouhal number at a relatively higher incidence angle. For instance, Re=40,000 flow sees that the first non-zero Strouhal number at 17° incidence angle, but Re=60,000, Re=80,000, and Re=100,000 flow see that 18°, 19°, and 19° angles of attack, respectively. It is still crucial to understand how Strouhal number numerically evolves and how the instantaneous lift coefficient responds to it, even though the incidence angle and Reynolds number effect may currently be investigated. Figure 4.33–Figure 4.37 are plotted to see how the Reynolds number changes the Strouhal number between 16°–20° angles of attack.

Table 4.1. Strouhal Numbers (St)

	α=17°	**α=18°**	**α=19°**	**α=20°**
Re=40,000	0.226	0.217	0.208	0.199
Re=60,000	–	0.280	0.280	0.271
Re=80,000	–	–	0.352	0.334
Re=100,000	–	–	0.406	0.397

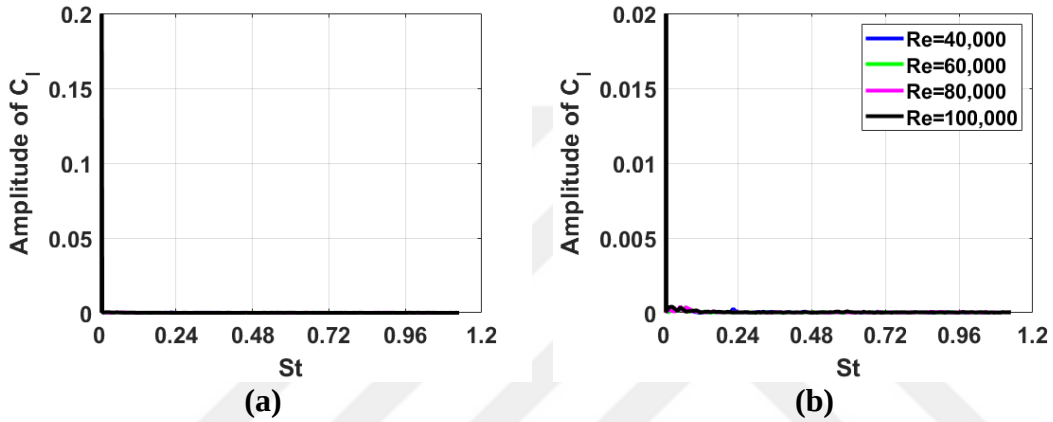

Figure 4.33. a) Amplitude spectrum of C_l versus Strouhal number at α=16° for different Reynolds numbers, b) Amplitude spectrum of C_l versus Strouhal number at α=16° for different Reynolds numbers (closer look)

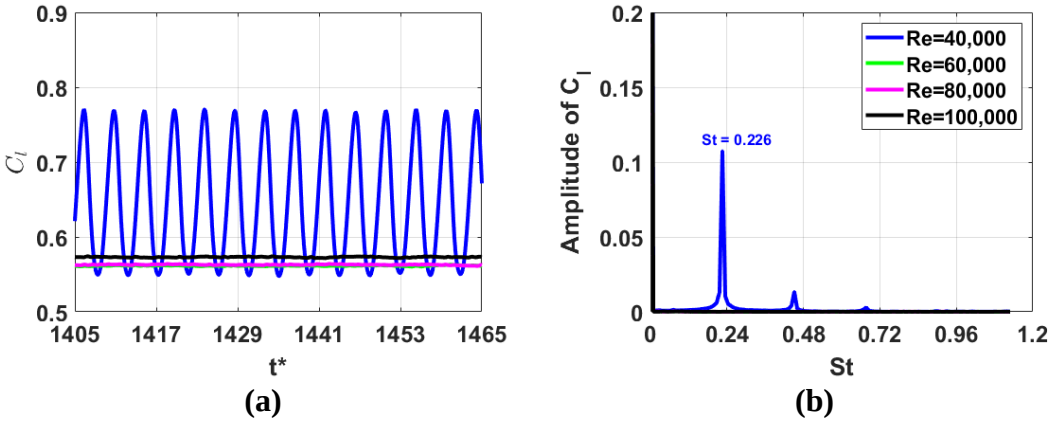

Figure 4.34. a) Instantaneous lift coefficient C_l, b) Amplitude spectrum of C_l versus Strouhal number at α=17° for different Reynolds numbers

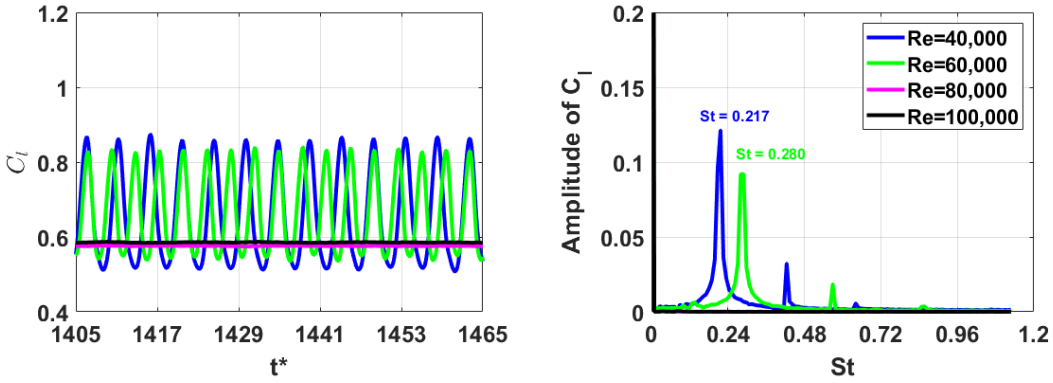

Figure 4.35. a) Instantaneous lift coefficient C_l, b) Amplitude spectrum of C_l versus Strouhal number at α=18° for different Reynolds numbers

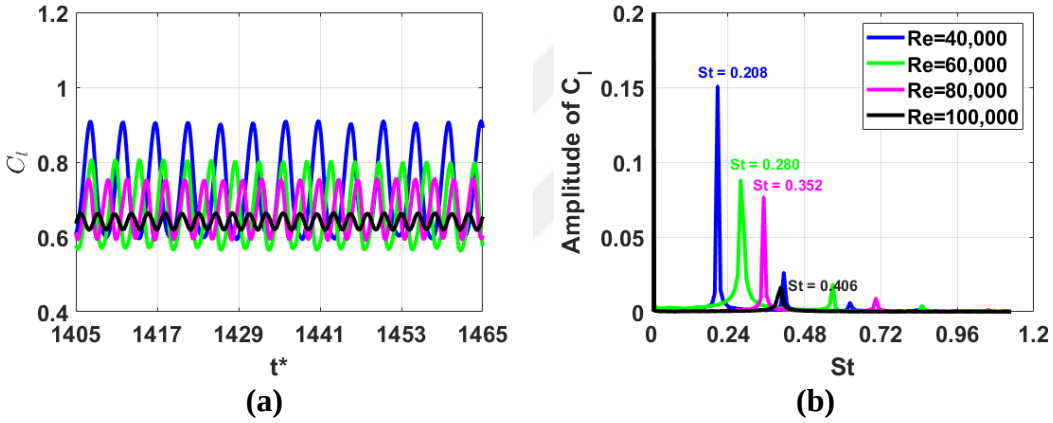

Figure 4.36. a) Instantaneous lift coefficient C_l, b) Amplitude spectrum of C_l versus Strouhal number at α=19° for different Reynolds numbers

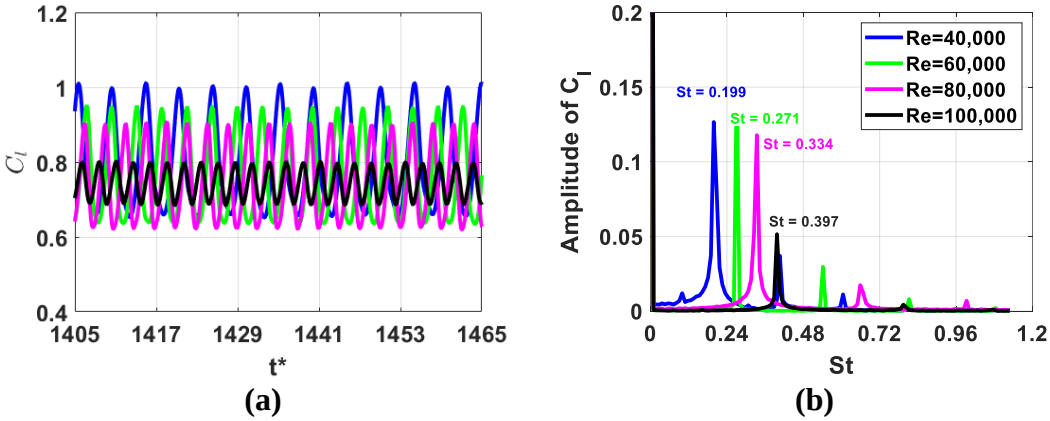

Figure 4.37. a) Instantaneous lift coefficient C_l, b) Amplitude spectrum of C_l versus Strouhal number at α=20° for different Reynolds numbers

Figure 4.33 represents that no oscillatory motion exists at the 16° incidence angle, but at the 17° incidence angle it starts immediately, and St=0.226 (Figure 4.34). In addition to that, the Strouhal number decreases to 0.217 at an 18° incidence angle for Re=40,000 and Re=60,000 flow experiences the Strouhal number as 0.280. If further angles of attack are investigated, all Reynolds number flows start to experience oscillatory motion, in other words, instability of the flow is high enough for shedding even for Re=100,000 (Figure 4.36 and Figure 4.37).

At 19° angle of attack, maximum Strouhal numbers are 0.208, 0.280, 0.352, and 0.406 for Re=40,000, 60,000, 80,000, and 100,000 respectively. In other words, the increment percentages are 34.62%, 25.71%, and 15.34%, it is brought on by the Reynolds number effect, which is more pronounced for flows with lower Reynolds numbers. Similarly, at 20° angle of attack, the increment percentages are 36.18%, 23.25%, and 18.86%.

4.6 Vortex Shedding Patterns of the Airfoil

The objective of this chapter is to present a study on the unstable vortex shedding patterns of the NACA 0012 airfoil at high and diverse incidence angles for various Reynolds values. As seen in previous chapters, the post-process for the Reynolds effect is done with Re=40,000, 60,000, 80,000, and 100,000. From the previous analysis, it concluded that the oscillations start at 17° incidence angle just for Re=40,000.

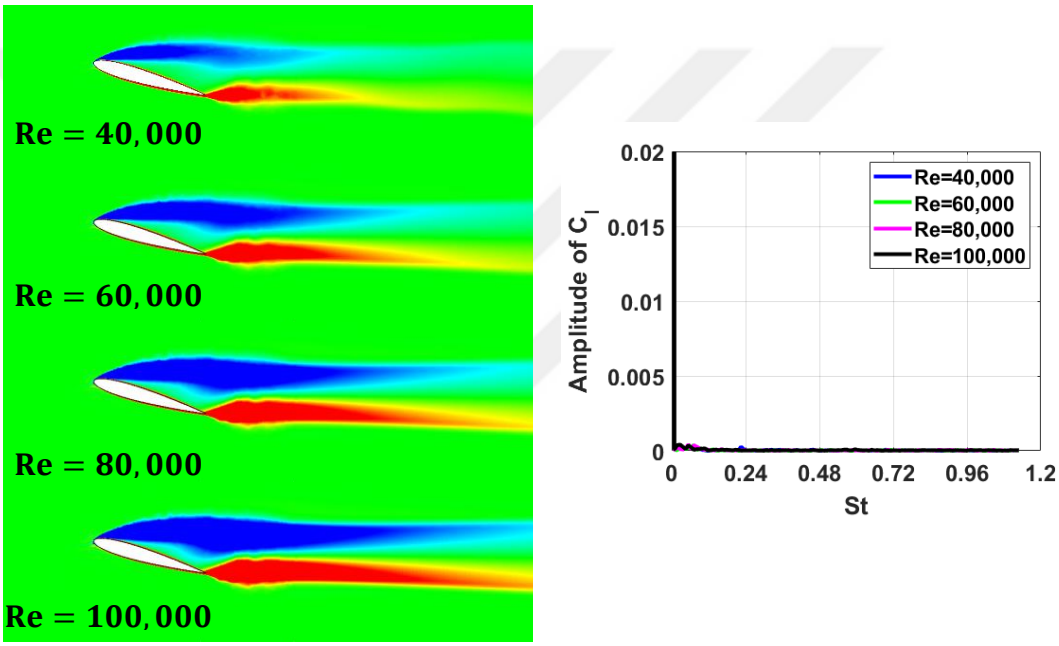

(a) **(b)**

Figure 4.38. a) Instantaneous wake patterns, b) Amplitude spectrum of C_l versus Strouhal number at α=16° for different Reynolds numbers

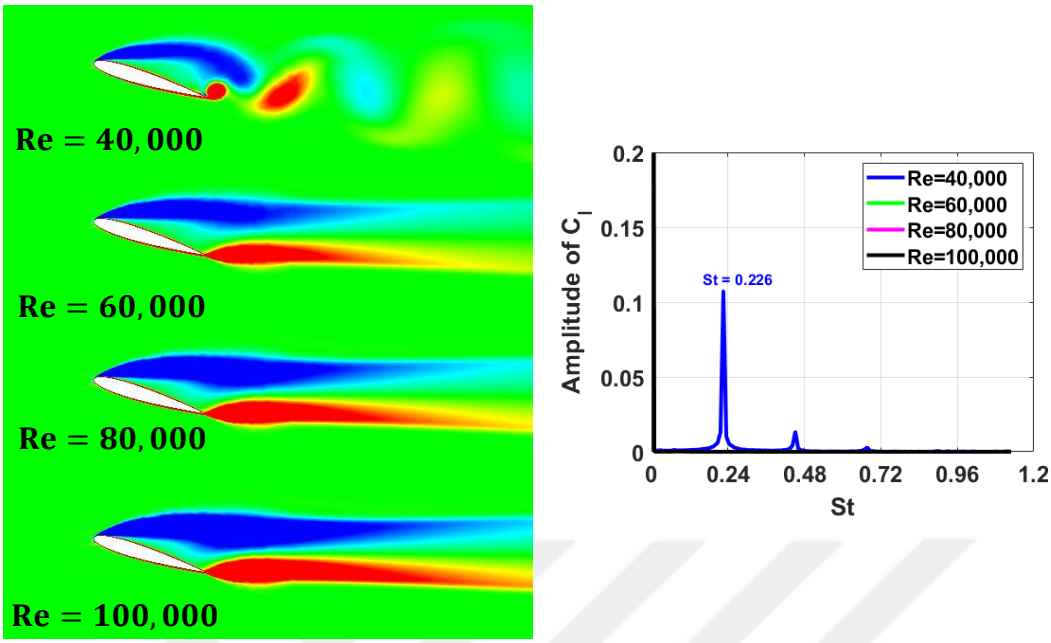

(a) **(b)**

Figure 4.39. a) Instantaneous wake patterns, b) Amplitude spectrum of C_l versus Strouhal number at $\alpha=17^{\circ}$ for different Reynolds numbers

Therefore, to observe the gradual change 16° angle of attack is also shown. Moreover, the Strouhal number distribution is also added to the corresponding figures, so it will be more clear to visualize the relationship between the Strouhal number and wakefield structure.

4.6.1 Influence of angle of attack

All Reynolds number flows have no oscillatory motion until the 17° incidence angle. For all Reynolds number flows, continuous vortex shedding is illustrated together with the 16° at this angle (Figure 4.38(a)). However, with a 1° increase in the incidence angle, the alternating vortex shedding patterns are shown just for Re=40,000. The rest of the flows face separation but do not produce enough drag for generating oscillations at the wakefield. Moreover, by looking Strouhal number distribution, it is apparent that there is a spike of Strouhal number at the 17° incidence angle for Re=40,000 which is not valid at the 16° angle of attack for all flows (Figure 4.38(b) and Figure 4.39(b)). This trend also continues for 18°, 19°, and 20° angles of attack. At 18°, the alternating vortex shedding patterns are also seen for Re=60,000 with a peak value of Strouhal number as 0.280. Finally, after 19° angle of attack, all flows exhibit vortex shedding. Throughout the angle of attack increment, vortex shedding density has increased for shaded ones. For instance, Re=40,000 flow has a relatively denser CCW (red) vortex at 18° angle of attack than 17° (see Figure 4.39 and Figure 4.40).

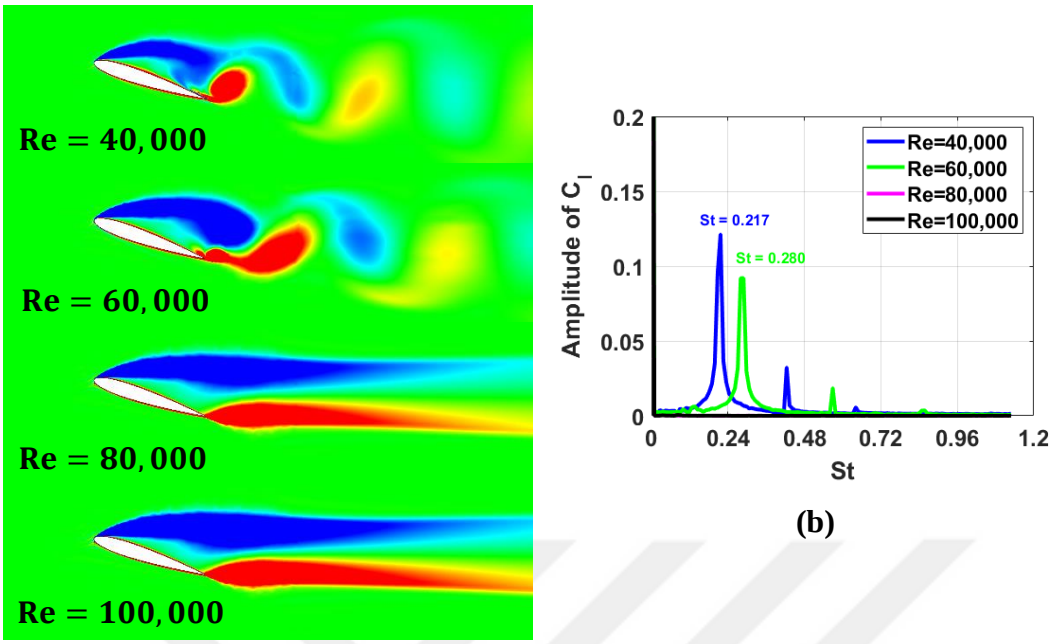

Figure 4.40. a) Instantaneous wake patterns, b) Amplitude spectrum of C_l versus Strouhal number at $\alpha=18^{\circ}$ for different Reynolds numbers

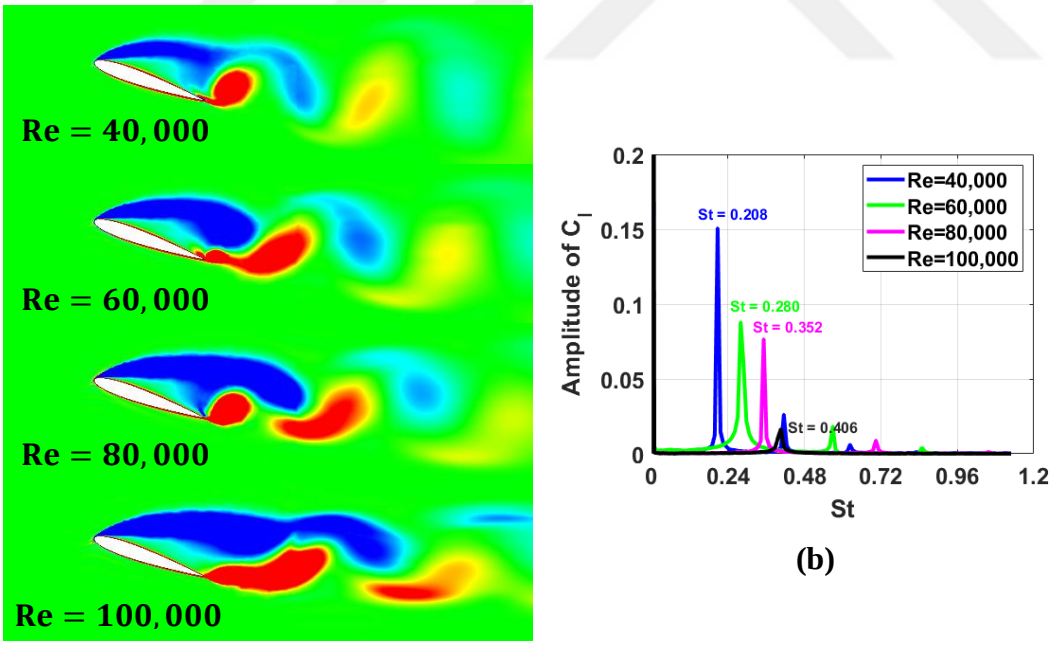

Figure 4.41. a) Instantaneous wake patterns, b) Amplitude spectrum of C_l versus Strouhal number at $\alpha=19^{\circ}$ for different Reynolds numbers

4.6.2 Influence of Reynolds number

A higher Reynolds number means that inertial forces are dominant to viscous forces, in other words, the higher Reynolds number flows have more resistance to separation and drag formation. That's why, the mean drag coefficient is also lower for relatively high Re flows (Figure 4.1.(b)). The figures in this section also support this result. For instance, at 17° and 18° angles of attack, there is no oscillatory motion for Re=80,000 and 100,000 (Figure 4.39(a) and Figure 4.40(a)).

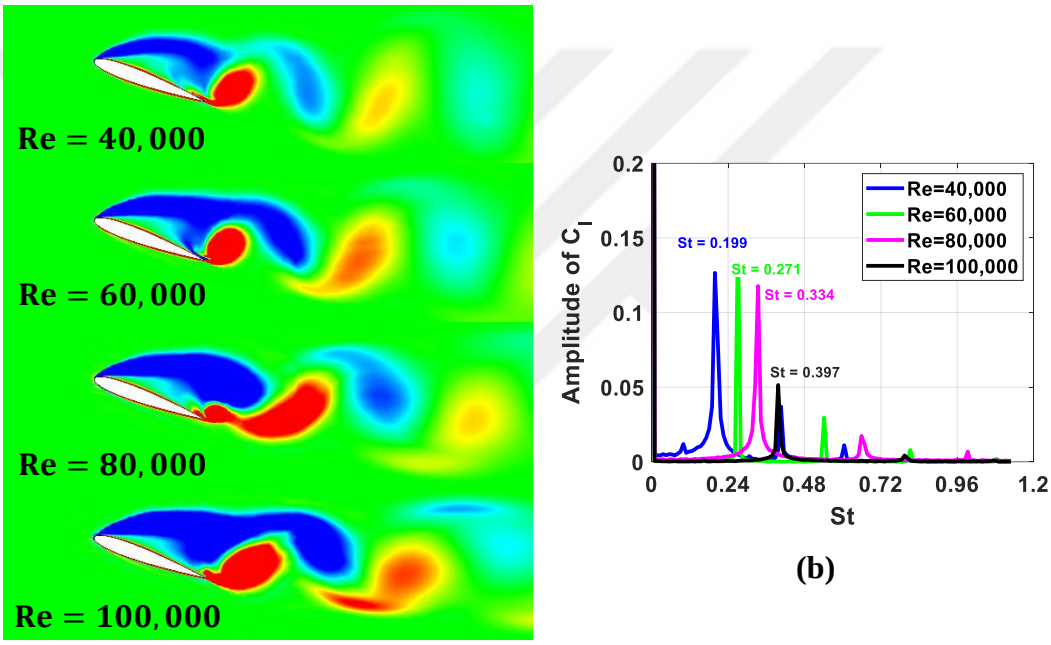

Figure 4.42. a) Instantaneous wake patterns, b) Amplitude spectrum of C_l versus Strouhal number at α=20° for different Reynolds numbers

Meanwhile, the flows of Re=40,000 and 60,000 already started to shed. Moreover, at just backward airfoil's trailing edge, the lower Reynolds number flows have more visible vorticity patterns, but the formation of vortices for relatively high ones is not too much mature.

CHAPTER 5

CONCLUSION

This study examines how Reynolds number and incidence angle affect the two-dimensional NACA 0012 airfoil's unsteady aerodynamic properties between Re=40,000–100,000. This work will offer insightful knowledge into the NACA 0012 airfoil's aerodynamic behavior at low Reynolds numbers and can be used to optimize the design of airfoils for specific uses, like small unmanned aerial vehicles or micro air vehicles.

Firstly, the numerical simulations of different Reynolds number flows are conducted via ANSYS FLUENT commercial tool in the two-dimensional domain for incidence angles from 0° to 20° with an increment of 1° per simulation. Low Reynolds numbers can produce extremely turbulent flow around an airfoil, which can cause a separation bubble to form on the surface of the airfoil. It can make it difficult to accurately capture the flow behavior in numerical simulations. Therefore, it is conducted detailed mesh and time refinement studies to optimize the simulation setup and ensure that it accurately simulates the flow behavior. Moreover, some simulation parameters such that turbulence intensity and turbulence model are also investigated closely. Although all turbulence models predict experimental results in a better way than previous numerical studies, the Transition-SST turbulence model which has 4 equations is selected rather than Spalart-Allmaras (1 equation), SST k–ω (2 equations), and k–kl–ω turbulence models (3 equations).

Transition-SST has the highest computational time than other turbulence models, however not only the mean aerodynamic coefficients but also mean pressure distributions show more correct results by using it. For instance, the Spalart-Allmaras turbulence model predicts stall angles as 12° and 8° which are 1° higher

and 1° lower than the previous experimental results for Re=100,000 and Re=40,000. But the Transition-SST turbulence model predicts stall angles directly what experimental results tell. Moreover, not only the "quasi" linear region of C_l versus α graph but also the post-stall region have consistent with the previous experimental results than other numerical studies. This work thus provides more trustworthy results than earlier efforts, despite the fact that the validation process in both this study and previous studies was greatly complicated by the flow behavior at low Reynolds numbers.

Generally, the results of the simulation study were then used to analyze various aerodynamic parameters which are lift coefficients, drag coefficients, pressure distributions, mean velocity streamlines, skin friction coefficients, Strouhal number, and wakefield vortex patterns. The effect of the Reynolds number on each of these parameters was carefully considered, and the results were demonstrated in figures to provide a clear understanding of the significance of the Reynolds number on unsteady aerodynamic behavior.

It is clear that for a given Reynolds number, the mean drag coefficients rise gradually with increasing incidence angle up to stall angle, then they accelerate incrementally from stall angle to 20° angle of attack. Meanwhile, the mean lift coefficients show decreasing trend after the stall angle. However, the decrease in mean lift coefficient after the stall angle does not dramatically. In other words, the post-stall characteristics are gentle for each Reynolds number between Re=40,000 and Re=100,000.

It may be said that a higher Reynolds number results in a higher mean lift coefficient and lower mean drag coefficient for a fixed angle of attack which is less than the stall angle. Because of this, the $\bar{C}_l/\bar{C}_d$ increases as the Reynolds numbers rise. In other words, the aerodynamic performance of the NACA 0012 airfoil is getting better for higher Reynolds numbers. Meanwhile, the angle which has the maximum $\bar{C}_l/\bar{C}_d$ is almost independent of the Reynolds number. The maximum $\bar{C}_l/\bar{C}_d$ value is seen around the 6° incidence angle. This point may be seen in the

maximum aerodynamic performance of the NACA 0012 airfoil for almost each Reynolds number. And, the effect of the Reynolds number is more dominant on the mean drag coefficient than the mean lift coefficient (Figure 4.2). Lastly, higher Reynolds number flows enable us to experience a stall a little bit late than lower Reynolds number flows. Numerically, the stall angles are observed as increasing from 9° to 11° incidence angle for Reynolds number 40,000 to 100,000, respectively.

Moreover, the mean lift slope with respect to the incidence angle is investigated in detail. For lower Reynolds numbers, the lift slope starts from lower values and increases up to 4° for Re=40,000 and 3° for Re=60,000. Then, the lowest two Reynolds number flows' mean lift slope is also decreasing like higher Reynolds numbers up to the stall angles. This is an expected result, because the existence of the separation bubbles are increasing with incidence angles, and the mean lift values are getting higher with lower increments. Also, the theoretical lift slope is represented with all Reynolds numbers at a fixed angle of attack (i.e. 0°). The relation is obvious that the Reynolds number has a positive effect on the lift change with respect to the incidence angle (Figure 4.5).

The mean skin friction coefficient is another crucial parameter that provides details regarding the location of separation points where C_f equals zero. In general, even for 0° incidence angle, all flow conditions in this effort experience separation bubbles on the upper airfoil surface. With the increasing incidence angle, the bubble moves forward and splits into two different bubble forms before reaching the stall angle. For a fixed incidence angle, the Reynolds number plays a damping role in terms of the size of the bubble. For instance, at 10° incidence angle, while the Re=40,000 flow already sees unattached flow, the higher Reynolds number flows still have attached flow on the mid part of the top surface of the airfoil. Since the higher Reynolds number indicates low viscous forces, this is an expected result. In addition to that, the reattachment point location differences due to various Reynolds numbers are observed at 20° angle of attack. The reattachment locations

are quite close to the trailing edge due to the high incidence angle, and there has been no detection of a second separation-reattachment bubble zone on the airfoil's top surface. However, the location of the reattachment point (R1) still goes a little more toward to leading edge with decreasing Reynolds number (Figure 4.13 and Figure 4.14).

The mean lift coefficient variation with respect to the angle of attack is also represented for each Reynolds number. The oscillatory properties of the instantaneous lift coefficient can be seen by red error bounds for each Reynolds number flow (Figure 4.16, Figure 4.18, Figure 4.20, and Figure 4.22). The main discussion in these figures is about understanding how streamlines and oscillatory motion of aerodynamic coefficients are related. It is revealed that for the incidence angles where the instantaneous lift coefficient starts quasi-periodic motion, the second counter-rotating vortex is attached to the airfoil's upper surface. By increasing the incidence angle, the amplitude magnitude of oscillatory behavior is also increasing, and the second vortex contact location propagates to the leading edge. In other words, for the non-oscillatory motion, the streamlines show directly deattached flow on the upper surface of the airfoil with one and a big clockwise rotating vortex.

Furthermore, the Strouhal number (St) and its relation between the different Reynolds numbers and different incidence angles are discussed. When there exists no oscillatory motion in instantaneous aerodynamic coefficients the Strouhal number equals zero. In other words, the Strouhal number explains whether the flow has vorticity or not. For instance, the first incidence angle (i.e. critical angle of attack) where the oscillatory movement starts is 17° for Re=40,000, and 18°, 19°, 19° for Re=60,000, Re=80,000, and Re=100,000 respectively. This can be commented such that the lower viscous flow needs to get more unsteady conditions to shed vortices and it reaches that by rising the incidence angle. Moreover, the existence of Strouhal number observations stated that the Strouhal number has an

almost linear relation with the Reynolds number for a fixed incidence angle but inverse relation with the incidence angle (Figure 4.31).

Lastly, the Strouhal number behavior is explained by showing the instantaneous lift coefficient and instantaneous wake patterns. To show the correlation between wake patterns, instantaneous lift coefficient, and St number is important to understand all pictures for the post-stall region of the NACA 0012 airfoil. For instance, the experimental results have a small lift increment between 18° and 19° incidence angles for Re=100,000, 16° and 17° angles of attack for Re=40,000 (Figure 3.14 and Figure 3.15). These increments may result from the starting of Mode 2 wake structures at these corresponding incidence angles. So, it may be concluded that the mean lift coefficient shows a more noticeable change than the mean drag coefficient at those critical incidence angles.

Future research can analyze the NACA 0012 airfoil for low Reynolds number flows in terms of the mean aerodynamic coefficient comparison and post-stall characteristics of the airfoil discussions by directly repeating this study with three–dimensional (3D) analyses. On top of that, the new geometrical implementations can be done to the NACA 0012 airfoil's commercial profile to understand whether the aerodynamic results which are discussed in this study are being changed or not.

REFERENCES

Abbott, I. H., & von Doenhoff, A. E. (1959). Theory of Wing Sections: Including a Summary of Airfoil Data. *Dover Publications*, Mineola.

Aftab, S. M. A., Mohd, Rafie, A. S., Razak, N. A., & Ahmad K. A. (2016). Turbulence Model Selection for Low Reynolds Number Flows. *PloS One*, *11*(4). https://doi.org/10.1371/journal.pone.0153755

Aftosmis, M., Gaitonde, D., & Tavares, T. S. (1995). Behavior of linear reconstruction techniques on unstructured grides. *AIAA Journal*, *33*(11), 2038–2049. https://doi.org/10.2514/3.12945

Agrawal, K., Patel, M., Shah, V., & Sura, J. (2020). Determination of Aerodynamic Characteristics of NACA 0012 using ANSYS for high Subsonic Flow. *SSRN Journal*. http://doi.org/10.139/ssrn.3696563

Ahuja, S., & Rowley, C.W. (2010). Feedback control of unstable steady states of flow past a flat plate using reduced–order estimators. *Journal of Fluid Mechanics*, *645*, 447–478. https://doi.org/10.1017/s0022112009992655

Alam, Md. M., Zhou, Y., Yang, H. X., Guo, H., & Mi, J. (2010). The ultra–low Reynolds number airfoil wake. *Experiments in Fluids*, *48*(1), 81–103. https://doi.org/10.1007/s00348–009–0713–7

Altenbuchner, C., & Hubbard, J. E. (2018). Modern Flexible Multi–Body Dynamics Modeling Methodology for Flapping Wing Vehicles, *Academic Press*. https://doi.org/10.1016/B978–0–12–814136–6.00002–0

Ananda, G. K., & Selig, S. M. (2018). Design of Bird–Like Airfoils. *AIAA SciTech Forum*, Kissimmee, Florida. https://doi.org/10.2514/6.2018–0310

Ansari, S. A., Phillips, N., Stabler, G., Wilkins, P. C., & Knowles, K. (2009). Experimental investigation of some aspects of insect–like flapping flight aerodynamics for application to micro air vehicles. *Experiments in Fluids, 46*(5), 777–798. https://doi.org/10.1007/s00348–009–0661–2

Anyoji, M., Nonomura, T., Aono, H., Oyama, A., Fujii, K., Nagai, H., & Asai, K.(2014). Computational and experimental analysis of a high–performance airfoil under low–Reynolds–number ow condition. *Journal of Aircraft, 51*(6), 1864–1872.

Ashraf, M. A., Young, J., & Lai, J., C., S. (2012). Oscillation frequency and amplitude effects on plunging Airfoil propulsion and flow periodicity. *AIAA Journal, 50*(11), 2308–2324.

Bakker, P. G. (1991). Bifurcations in Flow Patterns–Some Applications of the Qulitative Theory of Differential Equations in Fluid Dynamics. *Kluwer Academic.*

Batchelor, G. K. (2002). *An introduction to fluid dynamics*. Cambridge University Press.

Birch, J. M. (2003). The influence of wing–wake interactions on the productions of aerodynamic forces in flapping flight. *Journal of Experimental Biology, 206*(13), 2257–2272. https://doi.org/10.1242/jeb.00381

Bodavula, A., Yadav, R., & Guven, U. (2020). Numerical investigation of the unsteady aerodynamics of NACA 0012 with suction surface protrusion. *Aircraft Engineering and Aerospace Technology, 92*(2), 186–200. https://doi.org/10.1108/AEAT–01–2019–0022

Bohorquez, F., Pines, D., & Samuel, P. D. (2010). Small rotor design optimization using blade element momentum theory and hover tests. *Journal of Aircraft, 47*(1), 268–283. https://doi.org/10.2514/1.45301

Bull, S., Chiereghin, N., Gursul, I., & Cleaver DJ. (2021). Unsteady aerodynamics of a plunging airfoil in transient motion. *Journal of Fluids and Structure, 103*.

Calis, Ö., Kurtulus, D. F., & Arıkan, K. B. (2021). Modeling the flapping motion via Quasi–Steady Approach and Controlling the longitudinal Dynamics of a flapping wing MAV, *AIAC 2021–110, 11th Ankara International Aerospace Conference*, 8–10 September 2021, Ankara, Turkey.

Carmichael, B. (1981). Low Reynolds number airfoil survey. *National Aeronautics and Space Administration (Langley Research Center), NASA CR–165803*.

Chang, J., Zhang, Q., He L., & Zhou, Y. (2022). Shedding vortex characteristics analysis of NACA 0012 airfoil at low Reynolds numbers. *Energy Reports*, *8*, 156-174. https://doi.org/10.1016/j.cgyr.2022.01.149

Choudhry, A., Arjomandi, M., & Kelso, R. (2015). A study of long separation bubble on thick airfoils and its consequent effects. *International Journal of Heat and Fluid Flow*, *52*, 84–96. https://doi.org/j.ijheatfluidflow.2014.12.001

Counsil, J. N. N., & Boulama, K. G. (2012). Validating the URANS Shear Stress Transport γ–Re_θ Model for Low–Reynolds–Number External Aerodynamics. *International Journal for Numerical Methods in Fluids*, *69*(8), 1411–1432. https://doi.org/10.1002/fld.2651

Counsil, J. N. N., & Boulama, K. G. (2013). Low–Reynolds–number aerodynamic performances of the NACA 0012 and Selig–Donovan 7003 Airfoils. *Journal of Aircraft, 50*(1), 204–216.

Day, M. A. (1990). The no–slip condition of fluid dynamics. *Erkenntnis, 33*(3), 285–296. https://doi.org/10.1007/BF00717588

Dickinson, M. H., Lehmann, F. O., & Sane, S. P. (1999). Wing Rotation and the Aerodynamic Basis of Insect Flight. *Science*, *284*(5422), 1954–1960. https://doi.org/10.1126/science.284.5422.1954

Douvi, E. C., Margaris, D. P., Lazaropoulos, S. D., & Svanas, S. (2013). Low Reynolds Number Investigation of the Flow over a NACA 0012 Airfoil at Different Rainfall Rates. *Int. Rev. Mech. Eng.*, *7*, 625-632.

Eleni, D. C., Athanasios, T. I., & Dionissios, M. P. (2012). Evaluation of the turbulence models for the simulation of the flow over a National Advisory Committee for Aeronautics (NACA) 0012 airfoil. *Journal of Mechanical Engineering Research, 4*(3). https://doi.org/10.5897/11.074

Ellington, C. P., van den Berg, C., Willmott, A. P., & Thomas, A. L. R. (1996). Leading–edge vortices in insect flight. *Nature, 384*(6610), 626–630. https://doi.org/10.1038/384626a0

Ferziger, J. H., Peric, M., & Street, R. L. (2020). *Computational Methods for Fluid Dynamics*. Springer.

Fluent ANSYS. (2015). *Theory Guide Release 16.1*, Ansys Inc.

Fluent ANSYS. (2016). *User's Guide Release 16.1*, Ansys Inc.

Fowler, A. C., & Howell, P., D. (2003). Intermittency in the Transition to Turbulence. *SIAM Journal on Applied Mathematics, 63*(4), 1184–1207. https://doi.org/10.1137/S0036139900368893

Gao, W., Samtaney, R., & Parsani, M. (2022). Direct numerical simulation of transitional flow past an airfoil with partially covered wavy roughness elements. *Physics of Fluids, 34*(10): 105135. https://doi.org/10.1063/5.0123437

Genc, M. S., Lock, G. D., & Kaynak, Ü. (2008). An Experimental and Computational Study of Low Re Number Transitional Flows over an Aerofoil with Leading Edge Slat, *AIAA Paper*, 2008–8877.

Gerasimov, A. (2006). Modeling Turbulent Flows with FLUENT. *ANSYS, Inc*., Europe.

Gerontakos, P., & Lee, T. (2006). Oscillating Wing Loadings with Trailing–Edge Strips. *Journal of Aircraft, 43*(2), 428–436. http://dx.doi.org/10.2514/1.15616

Gilling, L, S., Rensen, N., & Davidson, L. (2009) Detached eddy simulations of an airfoil in turbulent inflow. *Proceedings of 47th AIAA Aerospace Sciences Meeting Including the New Horizons Forum and Aerospace Exposition*, Orlando, Florida.

Gopinath, A. K., & Jameson, A. (2006). Application of the Time Spectral Method to Periodic Unsteady Vortex Shedding. *44th AIAA Aerospace Sciences Meeting and Exhibit*. https://doi.org/10.2514/6.2006–449

Grauer, J., Ulrich, E., Hubbard, J., Pines, D., & Humbert, J. S. (2011). Testing and System Identification of an Ornithopter in Longitudinal Flight. *Journal of Aircraft, 48*(2), 660–667. https://doi.org/10.2514/1.c031208

Gunaydinoglu, E., & Kurtulus, D. F. (2020). Pressure–velocity coupling algorithm–based pressure reconstruction from PIV for laminar flows. *Experiments in Fluids, 61*(5), 1–20.

Harmon, R. L., & Hubbard Jr, J. E. (2015). Aerodynamic Modeling of a Flapping Membrane Wing Using Motion Tracking Experiments.

Hau, E., & von Reynouard, H. (2006). *Wind Turbines*. Springer. https://doi.org/10.1007/3–540–29284–5

Hoffmann, J. A. (1991). Effects of free stream turbulence on the performance–characteristics of an airfoil. *AIAA Journal, 29*(9), 1353–1354.

Hu, H., & Yang, Z. (2008). An experimental study of the laminar flow separation on a low–Reynolds–number airfoil. *Journal of Fluids Engineering, 130*(5). https://doi.org/10.1115/1.2907416

Huang, R. F., & Lin, C. L. (1995). Vortex shedding and shear–layer instability of wing at Low–Reynolds numbers. *AIAA Journal, 33*(8), 1398–1403.

Huang, R. F., Wu, J. Y., Jeng, J. H., & Chen, R. C. (2001). Surface flow and vortex shedding of an impulsively started wing. *Journal of Fluid Mechanics, 441*, 265–292. https://doi.org/10.1017/s002211200100489x

Jiang, H., & Cheng, L. (2017). Strouhal-Reynolds number relationship for flow past a circular cylinder. *Journal of Fluid Mechanics, 832*, 170–188. https://doi.org/10.1017/jfm.2017.685

Jones, K. D., Dohring, C. M., & Platzer, M. F. (1996). Wake structures behind plunging airfoils – A comparison of numerical and experimental results. *AIAA Journal*. https://doi.org/10.2514/6.1996–78

Jung, Y.W., & Park, S.O. (2005). Vortex–shedding characteristics in the wake of an oscillating airfoil at low Reynolds number. *Journal of Fluids and Structures*,*20*(3),451–464.https://doi.org/10.1016/j.jfluidstructs.2004.11.002

Kang, C., & Shyy, W. (2013). Scaling law and enhancement of lift generation of an insect–size hovering flexible wing. *Journal of the Royal Society Interface, 10*(85). https://doi.org/10.1098/rsif.2013.0361

Kang, C. K., Fahimi, F., Griffin, R., Landrum, D. B., Mesmer, B., Zhang, G., L, T., & Aono, H. (2018). Marsbee–Swarm of flapping wing flyers for enhanced MARS exploration. *NASA Phase I – Final Report*.

Khalid, M., Uddin, E., Naseem, M. A., Mubashar, A., & Shah, S. (2017). Investigation of the flow around uncambered airfoils at 1000 Reynolds number using computational fluid dynamics for micro air vehicles.

Khchine, Y. E., & Sriti, M. (2017). Boundary layer and grid refinement effects on aerodynamic performances of horizontal axis wind turbine (HAWT). *International Journal of Mechanical Engineering, 2*, ISSN:2367–8968.

Krishnan, A., & Roy, S. (2022). Aerodynamic Profile Modification of a NACA 0012 Aerofoil for Enhanced Lift–Drag Characteristics at Low Reynolds Number. *U. Porto Journal of Engineering, 8*(2), 156–158. https://doi.org/10.24840/2183–6493_008.002_0012

Kurtulus, D. F., Farcy, A., & Alemdaroglu, N. (2004). Numerical Calculation and Analytical Modelization of Flapping Motion, *Proceeding of 1st European Micro Air Vehicle Conference and Flight Competition*, Braunschweig, Germany, 13–14 July 2004

Kurtulus, D. F., Farcy, A., & Alemdaroglu, N. (2005). Unsteady Aerodynamics of Flapping Airfoil in Hovering Flight at Low Reynolds Numbers, *AIAA–2005–1356, 43rd AIAA Aerospace Sciences Meeting and Exhibit*, Reno, Nevada, USA, 10 – 13 Jan 2005.

Kurtulus, D. F., David, L., Farcy, A., & Alemdaroglu, N. (2006a). A Parametrical Study with Laser Sheet Visualization for an Unsteady Flapping Motion, *AIAA–2006–3917, 36th AIAA Fluid Dynamics Conference and Exhibit*, San Francisco, California USA, 5 – 8 June 2006.

Kurtulus, D. F., David, L., Farcy, A., & Alemdaroglu, N. (2006b). Laser Sheet Visualization for Flapping Motion in Hover, *AIAA–2006–0254, 44rd AIAA Aerospace Sciences Meeting and Exhibit*, Reno, Nevada, USA, 9 – 12 Jan 2006.

Kurtulus, D. F., David, L., Farcy, A., & Alemdaroglu, N. (2008). Aerodynamic characteristics of flapping motion in hover. *Experiments in Fluids, 44*, 23–36. https://doi.org/10.1007/s00348–007–0369–0

Kurtulus, D. F. (2015). On the unsteady behavior of the flow around NACA 0012 airfoil with steady external conditions at Re=1000. *International Journal of Micro Air Vehicles, 7*(3), 301–326. https://doi.org/10.1260/1756–8293.7.3.301

Kurtulus, D. F. (2016). On the wake pattern of symmetric airfoils for different incidence angles at Re=1000. *International Journal of Micro Air Vehicles, 8*(2), 109–139. https://doi.org/10.1177/1756829316653700

Kurtulus, D. F. (2018). Aerodynamic loads of small amplitude pitching NACA 0012 airfoil at Reynolds number of 1000. *AIAA Journal*, *56*(8), 3328–3331

Kurtulus, D. F. (2019). Unsteady aerodynamics of a pitching naca 0012 airfoil at low Reynolds number. *International Journal of Micro Air Vehicles, 11*, 1–21.

Kurtulus, D. F. (2021). Vortex flow aerodynamics behind a symmetric airfoil at low angles of attack and Reynolds Numbers, *International Journal of Micro Air Vehicles*, *13*, 1–18. https://doi.org/10.1177/17568293211055653

Kurtulus, D. F. (2022). Critical Angle and Fundamental Frequency of Symmetric Airfoils at Low Reynolds Numbers, *Journal of Applied Fluid Mechanics*, *15*(3), May 2022, 723–735. https://doi.org/735.10.47176/JAFM.15.03.33099

Laitone, E. V. (1997). Wind Tunnel Tests ofWings at Reynolds Numbers Below 70000. *Experiments in Fluids*, *23*(5), 405–409. https://doi.org/10.1007/s003480050128

Lan, T., Li, G., & Zhang, M. (2020). Calculation Method of Aerodynamic Performance of Small Propeller with Serrated Trailing Edge. *Journal of Physics: Conference Series*, *1600*(1), 012012. https://doi.org/10.1088/1742–6596/1600/1/012012

Langtry, R. B., & Menter, F. R. (2009). Correlation–based transition modeling for unstructured parallelized computational fluid dynamics codes. *AIAA journal*, *47*(12), 2894–2906. https://doi.org/10.2514/1.42362

Lian, Y., Shyy, W., Viieru, D., & Zhang, B. (2003). Membrane wing aerodynamics for micro air vehicles. *Progress in Aerospace Sciences*, *39*(6–7), 425–465. https://doi.org/10.1016/s0376–0421(03)00076–9

Lilienthal, O. (2000). *Birdflight As the Basis of Aviation*. Markowski International.

Liseikin, V. D. (2009). *Grid Generation Methods*. Springer Science and Business Media.

Lu, S., Liu, J., & Hekkenberg, R. (2021). Grid Properties for RANS Simulations of Airfoil–Shaped Profiles: A Case Study of Rudder Hydrodynamics. *Journal of Marine Science and Engineering, 9*(10), 1062. https://doi.org/10.3390/jmse9101062

Lua, K. B., Lim, T. T. Yeo, K. S., & Oo, G. Y. (2007). Wake–structure formation of a heaving two–dimensional elliptic airfoil. *AIAA Journal*, *45*(7), 1571–1583. https://doi.org/10.2514/1.25310

Lyon, C. A., Broeren, A. P., Giguere, P., Gopalarathnam, A., & Selig, M. S. (1997). Summary of Low–Speed Airfoil Data, *University. of Illinois at Urbana–Champaign, 3*(5). https://doi.org/10.5656

McAurthur, J. (2008). Aerodynamics of Wing at Low Reynolds Numbers: Boundary Layer Separation and Reattachment, *Dissertation Abstracts International, 69*(11), 6953.

Mckeough, P. J., & Graham, J. M. R. (1980). Effect of mean loading on the fluctuating loads induced on aerofoils by a turbulent stream. *Aeronautical Quarterly, 31*, 56–69.

McMasters, J. H., & Henderson, M. L. (1980). Low–Speed Single–Element Airfoil Synthesis, *Technical Soaring, 6*(2), 1–21.

McMasters, J. H. (2004). The Biomechanics of Flight: Many Possible Solutions Looking for Problems. *International Journal of Engineering Education, 20*(3), 398–404.

McGranahan, B., & Selig, M. (2012). Surface Oil Flow Measurements on Several Airfoils at Low Reynolds Numbers. https://doi.org/10.2514/6.2003–4067

Medida, S., & Baeder, J. D. (2011). Application of the Correlation–Based γ̃–$Re_{\tilde{\Theta}t}$ Transition Model to the Spalart–Allmaras Turbulence Model. *20th AIAA Computational Fluid Dynamics Conference, 3979*. https://doi.org/10.2514/6.2011–1979

Medina, A., Rade, D. A., Sales, T.D.P., & Souza, F. (2014). Study of the Flow over an Oscillating NACA 0012 Airfoil. *VIII Congresso Nacional De Engenharia Mecanica Uberlandia.*

Mendez, B., Munoz, A., Pires, O., & Munduate, X. (2017). Characterization of the carborundum used in rough airfoil surface tests and modelling with CFD. *35th Wind Energy Symposium*, 1–14. https://doi.org/10.2514/6.2017–0916

Menter, F. R. (1994). Two–equation eddy–viscosity turbulence models for engineering applications. *AIAA journal, 32*(8), 1598–1605. https://doi.org/10.2514/3.12149

Menter, F. R., Langtry, R., Likki, S., Suzen, Y., Huang, P., & Volker, S. (2006). A correlation–based transition model using local variables—Part I: model formulation. *Journal of turbomachinery, 128*(3), 413–422. https://doi.org/10.1115/1.2184352

Mish, P. F., & Devenpor, W. J. (2001). Mean loading effects on the surface pressure fluctuations on an airfoil in turbulence. *Proceedings of 7th AIAA/CEAS Aeroacoustics Conference*, Maastricht, The Netherlands.

Mousavi, S. M., Aminian, J., Shafiei, N., & Dadvand, A. (2017). Numerical Simulatioın of Subsonic Turbulent Flow Over Naca0012 Airfoil: Evaluation of Turbulence Models. *Sigma Journal of Engineering and Natural Sciences, 35*(1), 133–155.

Mueller, T. J., & Batill, S. M. (1982). Experimental Studies of Separation on a Two–Dimensional Airfoil at Low Reynolds Numbers, *AIAA Journal, 20*(4), 457–463. https://doi.org/10.2514/3.51095

Mueller, T. J. (1999). Aerodynamic Measurements at Low Reynolds Numbers for Fixed Wing Micro–Air Vehicles. *RTO AVT/VKI Special Course on Development and Operation of UAVs for Military and Civil Applications*, Von–Karman. https://www.dticmil/docs/citations/ADP010760

Mueller, T. J., & DeLaurier, J. D. (2003). Aerodynamics of Small Vehicles, *Annual Review of Fluid Mechanics, 35*(1), 89–111. https://doi.org/10.1146/ 35.101101.161102

Naeem, N., Fouda M., Güney M., & Kurtulus D. K. (2023). Wake Patterns and mode switching at low Reynolds numbers, *Progress in Computational Fluid Dynamics, 23*(2), 87–100. https://doi.org/10.1504/PCFD.2023.129762

Narsipur, S., Pomeroy, B., & Selig, M. (2012). CFD analysis of multielement airfoils for wind turbines. *30th AIAA Applied Aerodynamics Conference*, New Orleans, Louisiana. https://doi.org/10.2514/6.2012–2781

NASA Langley. (2014). NASA Langley. https://images.nasa.gov

Ohmi, K., Coutanceau, M., Loc, T. P., & Dulieu, A. (1990). Vortex formation around an oscillating and translating airfoil at large incidences. *Journal of Fluid Mechanics, 211*, 37–60.

Ohmi, K., Coutanceau, M., Daube, O., & Loc, T. P. (1991). Further experiments on vortex formation around an oscillating and translating airfoil at large incidences. *Journal of Fluid Mechanics, 225*, 607–630.

Ohtake, T., Nakae, Y., & Motohashi, T. (2007). Nonlinearity of the Aerodynamic Characteristics of NACA 0012 Aerofoil at Low Reynolds Numbers. *Japanese Society for Aeronautical and Space Science Papers, 55*(644), 439–445. https://doi.org/ 10.2322/jjsass.55.439

Özdemir, Y., H., & Barlas, B. (2021). 2D and 3D Potential Flow Simulation around NACA 0012 Airfoil with Ground Effect. *CC BY 4.0 Licence*. https://doi.org/10.21203/rs.3.rs–151154/v1

Platzer, M. F., Jones, K. D., Young, J., & Lai, J. C. S. (2006). Flapping Wing Aerodynamics: Progress and Challenges. *AIAA Journal, 46*(9), 2136–2149. https://doi.org/10.2514/1.29263

Raney, D., & Waszak, M. (2003). Biologically Inspired Micro–Flight Resarch. *SAE Techinal Paper*, Montreal, Quebec, Canada.

Ren, N., & Ou, J. (2009). Dust Effect on the Performance of Wind Turbine Airfoils. *Journal of Electromagnetic Analysis and Applications, 1*(2), 209–220. https://doi.org/10.1016/j.desal.2007.04.030

Rinoie, K., & Takemura, N. (2004). Oscillating behaviour of laminar separation bubble formed on an aerofoil near stall. *The Aeronautical Journal, 108*(1081), 153–163.

Rossi, E., Colagrossi, A., Oger, G., & Le Touze, D. (2018). Multiple bifurcations of the flow over stalled airfoils when changing the Reynolds number. *Journal of Fluid Mechanics, 846*, 356–391.

Rumsey, C. L., & Spalart, P. R. (2009). Turbulence model behaviour in low Reynolds number regions of aerodynamic flowfields, *AIAA Journal, 47*(4), 982–993.

Salim, S. M., & Cheah, S. C. (2009). Wall y+ strategy for dealing with wall–bounded turbulent flows. *The International MultiConference on Engineerings and Computer Science,* Hong Kong.

Sane, S., & Dickinson, M. (2002). The aerodynamic effects of wing rotation and a revised quasi–steady model of flapping flight. *Journal of Experiemental Biology, 205,* 1087–1096.

Saniei, N. M. (2009). *Fundamentals of turbulent flows and turbulence modeling*. Danesh Negar Press, Tehran, Iran. (In Persian).

Saniei, N. M., & Mani, M. (2014) Numerical comparison between physics of transitional flow and full turbulent flow around classical airfoil of NACA0012 at subsonic and transonic regimes. *Journal of Fluid Mechanics and Aerodynamics, 2*, 63–87 (In Persian).

Selig, M. S., Donovan, J. F., & Fraser, D. B. (1989). Airfoils at LowSpeeds, *H.A. Stokely, 12*.

Selig, M., Guglielmo, J., Broern, A., & Giguere, P. (1996). Experiments on airfoils at low Reynolds numbers. https://doi.org/10.2514/6.1996–62

Selig, M. S., Lyon, C. A., Giguere, P., Ninham, C. P., & Guglielmo, J. J. (1996). Summary of Low–Speed Airfoil Data, *SoarTech Publ., 2*(5).

Schlichting, H. (1979). *Boundary Layer Theory*. 7th ed., McGraw–Hill, New York.

Schmitt, F. G. (2007). About boussinesq's turbulent viscosity hypothesis; Historical remarks and a direct evaluation of its validity. *Comptes Rendus Mecanique, 335*, 617–627. https://doi.org/10.1016/j.crme.2007.08.004

Schmitz, F. W. (1967). Aerodynamics of the Model Airfoil Part I: Airfoil Measurements, *Redstone Scientific Information Center RSIC–721*.

Shrestha, R., Benedict, M., Hrishikeshavan, V., & Chopra, I. (2016). Hover Performance of a Small–Scale Helicopter Rotor for Flying on Mars. *Journal of Aircraft*, *53*(4), 1160–1167. https://doi.org/10.2514/1.C033621

Shyy, W. (Wei). (2008). *Aerodynamics of low Reynolds number flyers*. Cambridge University Press.

Shyy, W., Aono, H., Kang, C., & Liu, H. (2013). *An Introduction to Flapping Wing Aerodynamics*. Cambridge University Press.

Spalart, P. R., & Allmaras, S. R. (1992). A one–equation turbulence model for aerodynamic flows. *AIAA, 092*(0439).

Srinivasan, G. R., & Baeder, J. D. (1992). TURNS: A Free–Wake Euler/Navier–Stokes Numerical Method for Helicopter Rotors. *AIAA Journal*, *31*(5), 959–962. https://doi.org/10.2514/3.49036

Tan, J., Wang, Z., & Gursul, I. (2021). Self–excited flag vibrations produce post–stall flow control. *Physical Review Fluids*, *6*(10):L102701

Taylor, K. G., Nudds, R. L., & Thomas, A. L. R. (2003). Flying and Swimming animals cruise at a Strouhal number tuned for high power efficiency. *Nature*, *425*(6959). https://doi.org/10.1038/nature02047

Thomas, M., & Boyer, M. (2011). *Aerovironment Develops World's First Fully Operational Life–Size Hummingbird–like Unmanned Aircraft for DARPA*. AeroVironment, Inc.

Tsuchiya, T., Numata, D., Suwa, T., & Asai, K. (2013). Influence of Turbulence Intensity on Aerodynamic Characteristics of an NACA0012 at Low Reynolds Numbers, *51st AIAA Aerospace Sciences Meeting AIAA Paper*, *65*. https://doi.org/10.2514/6.2013–65

Unsplash. (2021). Unsplash. https://unsplash.com/

Versteeg, H. K., & Malalasekera, W. (2007). *An introduction to computational fluid dynamics: The finite volume method*. 2nd ed., Pearson Education Limited, ISBN: 978–0–13–127498–3.

Walters, D.K., & Cokljat, D. (2008). A three–equation eddy–viscosity model for Reynolds–averaged Navier–Stokes simulations of transitional flow. *Journal of Fluid Engineering, 130*(12), 124101. https://doi.org/10.1115/1.2979230

Wang, S., Mi, J., & Wang, J. (2011). Effect of turbulence intensity on airfoil flow: Numerical simulations experimental measurements. *Applied Mathematics and Mechanics, 32*(8), 1029–1038. https://doi.org/10.1007/s10483–011–1478–8

Wang, S., Ingham, D. B., Ma, L., Pourkashanian, M. & Tao, Z. (2012). Turbulence modeling of deep dynamic stall at relatively low Reynolds number, *Journal of Fluids and Structures, 33*, 191–209.

Weis–Fogh, T. (1973). Quick estimates of flight fitness in hovering animals, including novel mechanism for lift production. *Journal of Experimental Biology*, 169–230.

Winslow, J., Otsuka, H., Govindarajan, B., & Chopra, I. (2018). Basic Understanding of Airfoil Characteristics at Low Reynolds Numbers (10^4–10^5). *Journal of Aircraft, 55*(3). https://doi.org/10.2514/1.C034415

Yamaguchi, Y., Ohtake, T., & Muramatsu, A. (2013). Pressure distribution on a NACA 0012 airfoil at low Reynolds number. *In The Proceedings of the International Conference on Jets, Wakes and Separated Flows (The Japan Society of Mechanical Engineers,* 1201.

Yang, W., Wang, L., & Song, B. (2018). Dove: A biomimetic flapping–wing micro air vehicle. *International Journal of Micro Air Vehicles, 10*(1), 70–84. https://doi.org/1 0.1177/1756829317734837

Yang, L. J., & Esakki, B. (2021). Flapping Wing Vehicles: Numerical and Experimental Approach.

Yarusevych, S., Sullivan, P. E., & Kawall, J. G. (2009). On vortex shedding from an airfoil in low–Reynolds–number flows. *Journal of Fluid Mechanics, 632*, 245–271.

Yousefi, K., Saleh, R., & Zahedi, P. (2014). Numerical study of blowing and suction slot geometry optimization on NACA 0012 airfoil. *Journal of Mechanical Science and Technology, 28*(4), 1–14. https://doi.org/10.1007/s12206–013–0913–y

Yu, W., Zhang, M. M., & Xu, J. Z. (2012). Effect of Smart Rotor Control Using a Deformable Trailing Edge Flap on Load Reduction under Normal and Extreme Turbulence. *Energies, 5*, 3608–3626. https://doi.org/10.3390/en5093608

Zafi, N. A., Hossain, A., & Mim, I. T. (2020). Experimental Study of NACA0012 Airfoil with Slanted Drills Through the Body. *Proceedings of International Exchange and Innovation Conference on Engineering and Sciences (IEICES), 6*, 258–263. https://doi.org/10.5109/41025

Zakaria, M. Y., İbrahim, M. M., Ragab, S., & Muhammed, R. (2018). A computational study of vortex shedding from NACA–0012 airfoil at high angles of attack. *International Journal of Aerodynamics, 6*(1). https://doi.org/10.1504/ijad.2018.089779

Zhang, Z., Wang, Z., & Gursul, I. (2022). Post–stall flow control with upstream flags. *Experiments in Fluids, 63*(179). https://doi.org/10.1007/s00348–022–03528–0